MICROCOPY RESOLUTION TEST CHART

NATIONAL BUREAU OF STANDARDS-1963-A
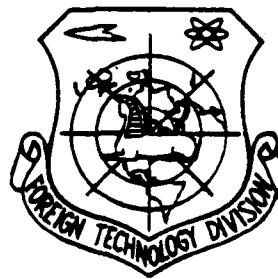
②

AD A139952

FOREIGN TECHNOLOGY DIVISION

AERONAUTICAL MATERIALS
(Selected Articles)

DTIC
S ELECTE D
APR 1 0 1984
B

Approved for public release;
distribution unlimited.

84 04 09 186

EDITED TRANSLATION

FTD-ID(RS)T-1868-83   13 March 1984

MICROFICHE NR: FTD-84-C-000270

AERONAUTICAL MATERIALS (Selected Articles)

English pages: 174

Source: Hangkong Cailiao, Nr. 2, Vol. 2, 1982, pp.
         1-7; 8-15; 16-22; 31-37; 38-44; 45-53; 54-59;
         60-74; 15 unnr pgs

Country of origin: USSR
Translated by: LEO KANNER ASSOCIATES
                F33657-81-D-0264
Requester: FTD/TQTA
Approved for public release; distribution unlimited.

GRAPHICS DISCLAIMER

All figures, graphics, tables, equations, etc. merged into this
translation were extracted from the best quality copy available.

TABLE OF CONTENTS

INFLUENCES OF DIRECTIONALLY SOLIDIFIED TECHNIQUES AND HAFNIUM CONTENT ON A NICKEL BASE HIGH TEMPERATURE ALLOY

Wang Luobao, Chen Rongzhang and Wang Yuping

Abstract

This paper uses two directionally solidified techniques, that is, the power decrease (P.D.) and high rate solidification (H.R.S.) methods, to study the influences of the different Hf contents on the structures and properties of a nickel base high temperature alloy. Test results show that when entering the alloy the Hf is mainly segregated in the interdentritic regions and γ/γ' eutectic phases; after the alloy is added, there are noticeable changes in the microstructure: the amount of γ/γ' eutectic phase noticeably increases, its morphology also undergoes noticeable changes; the conditions of grain boundaries and interdentritic regions are improved; several new types of Hf-rich microfacies also appeared. At 760°C, the endurance properties (especially the transverse properties) of the alloy noticeably rise with the increase of the Hf content. However, at 1040°C, the endurance life decreases with the increase of the Hf content. When we use the H.R.S. technique, the medium and high temperature performances of the alloy are both noticeably superior to the P.D. technique.

This paper discusses the mechanisms of the structure and property changes after the alloy adds Hf, determines that the relatively appropriate Hf content in this alloy is 1.0-2.0% (weight) and considers that we should give priority to the use of the H.R.S. directional technique.

I. Preface

1

Since the middle of the 1960's, metallurgical workers have carried out a great deal of work in adding Hf in nickel base cast high temperature alloys to improve the medium temperature strength and plastic mechanism. Important achievements were attained and a series of alloys with Hf and very good comprehensive properties appeared [1-7]. Afterwards, Duhl and others [8] brought the concept of adding Hf metamorphism into directionally solidified high temperature alloys which changes the structure of the alloy and thus greatly improved the transverse properties of the directional alloy and at the same time improved the castability. Nevertheless, to date, there have been very few reports on how Hf influences the high temperature (especially higher than $1\bar{0}00°C$) properties of alloys.

During our study of a high performance directionally solidified nickel base alloy, we discovered that after adding a small amount of Hf into the alloy, it had very good medium temperature properties. Yet, at 1040°C, the longitudinal endurance life of 13kg/mm^2 is 70-150 hours lower than alloys which do not add Hf. Therefore, when carrying out this test, we used two types of directionally solidified techniques to study the influences of the different Hf contents on the structures and properties of alloys so as to determine the proper amount of Hf. This paper briefly narrates and discusses the major results of this test.

II. Test Method

This test used an 80mm diameter circular bar made by vacuum smelt pouring the master alloy.

Its chemical composition is as follows (wt %):

C	Cr	Co	W	Al	Ti	Nb	B	Zr	Ni
0.12	8.97	9.98	12.69	4.98	2.04	1.06	0.014	0.080	Remainder

When we carried out vacuum remelting on the master alloy ingot, we separately added in 0.5, 1.0, 1.5, 2.0 and 2.5 (wt %) of Hf. The pouring temperature was about 1530°C and the shell type preheating temperature was about 1540°C. After pouring, the directional solidification based on the P.D. and H.R.S. methods obtained slab. The slab dimensions were 150x70x15mm or 240x70x15mm. We took vertical and horizontal samples from the upper cutting of the slab. Prior to machining by the sampler, we carried out the following range of heat treatment: 1205°C solid solution for 2 hours, air cooling and afterwards effective for 32 hours at 870°C.

We separately tested the technical methods and samples with different Hf contents at 760°C, 73.8kg/mm^2 and the vertical and horizontal endurance properties of 13kg/mm^2. We also tested the tensile properties at room temperature and 760°C.

We used the Neophat-2 optical microscope and JEM-200A electron microscope to observe the metallographic structure; separately carried out microregional composition analysis and fracture observations on a 733 model high level electronic probe instrument and JSM-35 scanning electron microscope; and used the area counting method to determine the volume fraction of the γ/γ' eutectic phase. The appearance of the alloy's microstructure used nitric acid: hydrofluoric acid: glycerine=1:2:3 reagent.

III. Test Results and Discussion

3.1 The Distribution of Hf in the Alloy Composition Phase

The electronic probe analyzed the concentration ratio of Hf in the γ/γ' eutectic phase, the interdendritic regions and interdentritic axis. It was 18:5:1 in the sample of the P.D. technique and 12:3:1 in the sample of the H.R.S. technique. This shows that Hf is a strong positive segregating element

3

mainly distributed in the interdentritic region and γ/γ' eutectic phase. Table 1 lists the concentrations of Hf in each composition phase of the alloy (the results of an analysis of an x-ray energy spectrum).

(1)添加Hf,% (2)组成相中Hf,% (3)组成相	(4)γ/γ'共晶		(7)晶间大 γ'	(8)晶轴小 γ'	MC(1)	MC(2)	(9)备注
	(5)中心	(6)边缘					
0.5		4.594	5.423	3.644	12.580	61.272	此外还形成
1.0	3.029	5.697	5.789	2.958	15.478	57.346	少量的富Hf 相,如Ni₅Hf,
1.5	3.602	4.948	6.386	2.534	20.516	56.389	(M, Hf)₂SC
2.0		5.77	6.613	3.801	19.014	45.515	(10)

(11) ● 试样取自P.D法板坯

Table 1 Hf concentrations in alloy composition phases*

Key: (1) Added Hf,%; (2) Hf in composition phase, %; (3) Composition phase; (4) Eutectic; (5) Center; (6) Boundary; (7) Interdendritic large; (8) Interdendritic small; (9) Remarks; (10) Aside from these, it also forms a small amount of Hf-rich phase such as Ni5Hf (M,Hf)2SC; (11)* The sample takes a slab by the P.D. method.

We can see from Table 1 that the Hf is primarily concentrated on the boundaries of the MC carbide, interdendritic coarse γ' phase and γ/γ' eutectic phase. Because the solubility of the Hf is very low ($<1\%$ at) in the γ base, it is repelled to the interdendritic region during the solidification process. The solubility of the Hf in the Ni_3Al is relatively large ($\sim 7\%$ at) [1] and therefore it can directly enter the interdendritic region's γ' phase. Although the Hf content in the MC carbide is relatively high, yet because the amount of MC in the alloy is relatively small, the added Hf is still mainly concentrated in the coarse γ' phase.

3.2 The Influence of Hf on the Alloy's Structure

4

Similar to other nickel base alloys with added Hf, after this alloy adds Hf, the microstructure has noticeable changes. The most outstanding among them is the increase in the amount of Υ/Υ' eutectic phase and the shape also changes from a small slab to a "large flower" shape. Following the increase of the Hf contents, this type of change becomes increasingly noticeable (Figs. 1 and 2, see Plate 1).
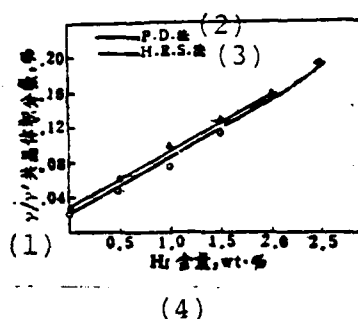
Fig. 1 The influence of the Hf content on the volume fraction of the Υ/Υ' eutectic phase.
Key: (1) Υ/Υ' eutectic volume fraction, %:
(2) Method; (3) Method; (4) Hf content, wt, %.

The major reason for the Υ/Υ' eutectic phase increases is the Hf changes the solidifying properties of the alloy which causes the temperature range between the liquid-solid phase line to widen. After Burton [2] added in 9% of Hf in an Mar-M200 alloy, the solidification range increased from 59.4°C to 70°C. The enlargement of the alloy's solidification range was the formation of the eutectic Υ' phase which provided advantageous dynamic conditions. In the H.R.S. technique, because the local solidification speed is relatively fast, the alloy's microsegregation decreases and the amount of Υ/Υ' eutectic phase is also less than with the P.D. method.

The adding of Hf causes another change in the alloy's micro-structure which was an improvement of the grain boundary and interdendritic region conditions (Fig. 1, see Plate 1). When Hf is not added, the vast majority of the grain boundary of the

5

alloy assumes fine line shapes, silver inlay of a small amount of MC and small slabs of Υ/Υ' eutectic phase (Fig. 3a); the interdendritic regions are skeleton shaped and long strip shaped MC carbides, coarse Υ' phase and a small amount of Υ/Υ' eutectic phase. After adding Hf, because the amount of Υ/Υ' eutectic region is large, the Υ' and grain shaped $M_{23}C_6$ on the grain boundary form occluded shaped grain boundary; during the heat treatment, because the carbide produces a reaction, the grain boundary $M_{23}C_6$ grains are surrounded by Υ' in varying degrees. This type of grain boundary condition matches the ideal grain boundary model proposed by Sims [9].

Aside from this Hf also causes noticeable changes in the alloy's microfacies The $MC_{(1)}$ carbide changes from the skeleton shape to independent block shapes and forms Hf-rich $MC_{(2)}$ carbide. At the same time, a small amount of low melting point metallic chemical compound phase Ni_5Hf and stable fine strip shaped sulfur carbide $(M, Hf)_2SC$ appear in the vicinity of the Υ/Υ' eutectic phase (see Fig. 4, see Plate 1).

3.3 The Influence of Hf on the Alloy's Mechanical Properties
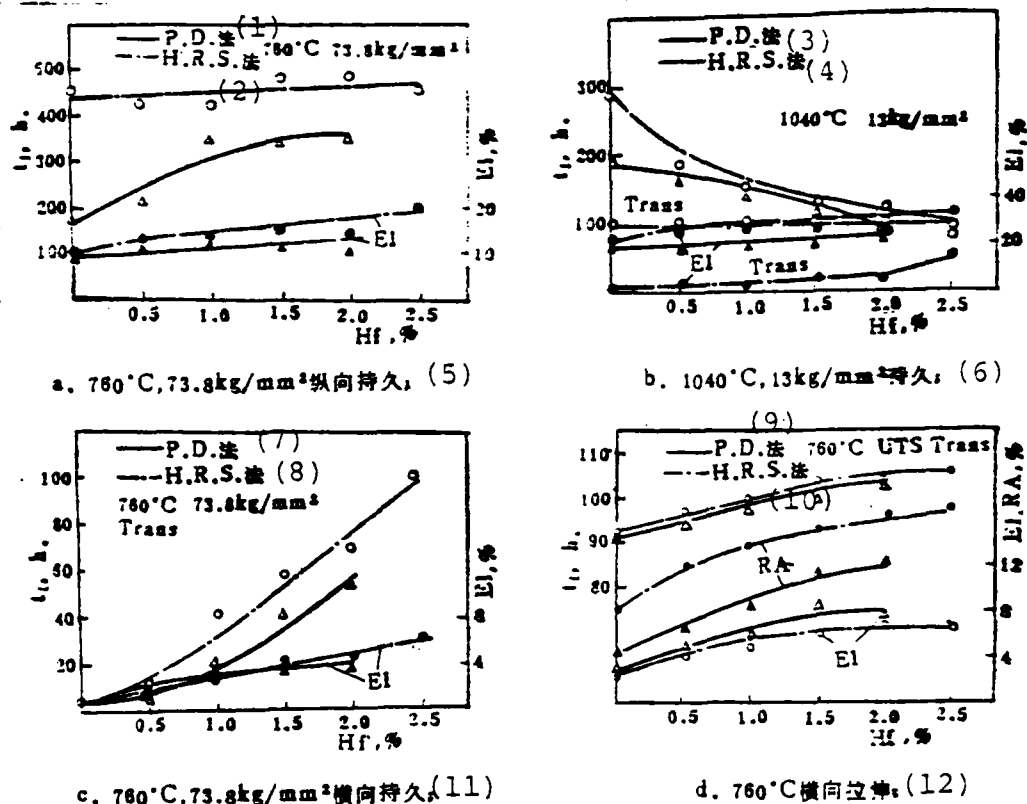
Fig. 5   The influence of Hf on the alloy's mechanical properties.
Key: (1)-(4) Method; (5) Longitudinal endurance;
(6) Endurance; (7)-(10) Method; (11) Transverse
endurance; (12) Transverse elongation.

(1) The Medium Temperature Endurance Properties. We can see
from Fig. 5a that the longitudinal and transverse endurance life
and plasticity of the alloy rise with the increase of the Hf
content. We believe that the major reason for the medium tem-
perature property rises is the above mentioned improvement of
the grain boundary condition. Because the operating position of
the transverse endurance tensile sample has a large amount of
grain boundary perpendicular to the main strain axis, the grain
boundary conditions has a determining effect on the medium
temperature properties of the alloy. The fracture observation
results also verify the above view, that is, no matter if it is
a longitudinal or transverse fracture sample, all of the samples
without Hf have typical fractures along the grain; but after

7

adding Hf $>$ 1.0 (wt %), then there is a noticeable change into mixed type fractures (Fig. 6, see Plate 2). This shows that adding Hf into the alloy noticeably raises the strength of the grain boundary and interdendritic regions. It is commonly considered that the grain shaped carbides in the occluded shaped grain boundary act to inhibit the grain boundary slip under medium temperature yet do not decrease plasticity. The coarse γ' phase surrounding the carbide can carry out plasticity adjustments. Reference [10] points out that the creep strength of the single phase γ' alloy is lower than that of the $\gamma + \gamma'$ two phase alloy but that the buckling strength is higher than the $\gamma + \gamma'$ two phase alloy. Therefore, the coarse γ' phase on the grain boundary can conveniently carry out plasticity adjustments and possess certain strength. γ' is not the same as ($\gamma + \gamma'$). It can carry out small, fine and uniform slipping and thus scatter and decrease the formation of grain boundary holes and cracks or cause crack passivation. Therefore, the existence of the coarse γ' phase in the grain boundary is advantageous to increasing the endurance life. Further, the adding of Hf causes the morphological changes of the MC carbide to also be able to delay the formation and expansion of the cracks.

Doherty and others [11] used the conclusion of "the Ni_3 (Al,Hf) alloy grain boundary has even greater anticracking capabilities than the Ni_3(Al,Ti) grain boundary" obtained from simple flexure tests of directionally solidified γ' phase alloy longitudinal samples. This explains that the coarse γ' phase transformed by the Hf alloy and distributed on the grain boundary is advantageous for raising the inherent strength of the grain boundary.

Another reason that the addition of Hf causes an increase in the grain boundary strength is that the formed stable $(M,Hf)_2SC$ is used to eliminate the harmful impurity S segregated

8

on the grain boundary thus raising the comprehensive strength of the grain boundary.

The results of this test on the medium temperature longitudinal properties have some dissimilarities with foreign reports [8,11]. They consider that after adding Hf the longitudinal properties of the alloy can be maintained unchanged. Our test results show that the rise of the $760°C-73.8kg/mm^2$ longitudinal endurance life of the P.D. technique is relatively large (Fig. 5a). The improvements mentioned above regarding the grain boundary and interdendritic region conditions after adding Hf, including the rises of the transverse section comprehensive strength of a large number of quadratic interdendritic axis regions and longitudinal grain boundaries, possibly contribute to the improvement of the medium temperature longitudinal properties. In view of the microcosmic deformation mechanism, when the Hf with relatively large atomic radii enter the Υ' phase, this can increase the mismatching of $\Upsilon - \Upsilon'$ and raise the alloy's eutectic strengthening effects. Further, Hf can raise the opposite phase domain energy of the dislocation cutting Υ' phase which is of aid to stopping dislocation cutting Υ' and raising the strengthening effects.

(2) High Temperature Endurance Properties. We can see from Fig. 5b that following the increase of the Hf content, the longitudinal high temperature endurance life gradually decreases. However, the transverse high temperature endurance life is basically maintained unchanged yet there is a slight rise in the plasticity.

The major reason that adding Hf causes the alloy's high temperature endurance life to decrease is the existence of Υ / Υ' eutectic phase (Fig. 1). The Υ / Υ' eutectic is a plastic phase [3] and is also a low melting point phase. The

9

high temperature strength is very low. When observing the high
temperature endurance fracture metallographic phase, we often
see that the Υ/Υ' eutectic phase has been elongated even to
the point of being pulled and broken off (Fig. 6). We can know
from the micro-analysis that the composition of the Υ/Υ'
eutectic phase is not uniform (Table 2). This creates self
instability. At the same time, the locally rich Hf at the
boundary of the Υ/Υ' eutectic phase easily forms a low
melting point chemical compound (Ni_5Hf) which is also naturally
not beneficial to the high temperature properties of the alloy.

(1)工 艺	部(2) 位	Ni	Cr	Al	Ti	Co	W	Nb	Hf
(3) P.D法	(5)共晶γ'边	64.406	2.949	10.339	3.039	6.020	6.688	0.858	5.697
	(6)共晶γ'中心	66.688	6.367	6.432	2.435	7.527	6.984	0.544	3.029
(4) H.R.S法	(7)共晶γ'边	50.645	4.259	16.925	2.385	6.362	13.747	1.380	4.825
	(8)共晶γ'中心	50.000	5.808	16.956	2.130	6.878	12.881	1.412	3.524

Table 2 Composition (weight %) of the eutectic Υ' phase of
an alloy containing 1.5 Hf.

Key: (1) Technique; (2) Position; (3) Method;
(4) Method; (5) Eutectic Υ' boundary; (6) Eutectic
Υ' center; (7) Eutectic Υ' boundary; (8) Eutectic
Υ' center.

Secondly, the adding of Hf causes the high temperature
stability of the $^-\Upsilon'$ phase to decrease. After we put samples
with different Hf contents through standard heat treatment,
when exposed at 1040°C for 100 hours, we discovered that cube
Υ' of the sample with Hf not only had three-dimensional
growth but also had relatively clear linear grouping (Fig. 7,
see Plate 1).

It is well known that the eutectic stress field of the Υ'
phase and base in a nickel base high temperature alloy is one
of the major strengthening factors when in an operating

10

temperature of less than 0.6T melting; but when in an operating temperature higher than 0.6T melting, the excessively high eutectic stress field becomes a factor for γ' phase high temperature instability. When the Hf enters the γ' phase, this causes the mismatching of the $\gamma - \gamma'$ to enlarge, the eutectic stress to rise, under high temperature the excessively high eutectic stress will cause the destruction of the eutectic relationship, dislocations appeared in the vicinity of the boundary surface which provided a short circuit diffusion passage and promoted the growth of the γ' phase. Under the effects of high temperature stress, the major deformation mechanism is diffusion and the clear grouping of the γ' phase increased the particle distance which is of benefit to the dislocation climbing.

In an alloy with Hf added, the existence of the Ni_5Hf phase with a low melting point (1200-1220°C) is a weak strength region. Under the effects of high temperature strain, it very possibly becomes the starting point of the crack or the passage of the diffusion. When observing the fracture, we often see the appearance of microholes and quadratic cracks in the area of the remaining Ni_5Hf (Fig. 9, see Plate 2). Therefore, the formation of the Ni_5Hf phase is also one reason for the decrease in the high temperature endurance properties.

(3) Tension Properties. The influence of Hf on the alloy's room temperature and 760°C tension properties are shown in Fig. 5d. It can be seen that at 760°C the transverse tension strengths of the P.D. method and H.R.S. method are equal, about 10 kilograms higher than samples without Hf. The plasticity also rises. After adding Hf, the longitudinal tension strength of the H.R.S. method basically remains unchanged yet the plasticity rises a little. Aside from this, the test data also shows that the influence of Hf on the alloy's room temperature tension properties is not large.

11

3.4 The Influence of the Directional Technique on the Alloy's Mechanical Properties

We can see from Fig. 5 that the 760°C transverse endurance properties of the P.D. method and H.R.S. method always rise with the increase of the Hf content and that the range raised by the H.R.S. method is much greater than that of the P.D. method. Although the 760°C longitudinal endurance life of H.R.S. method increases with the Hf content and basically remains unchanged, yet the life level is about 100 hours higher than P.D. method samples.

As regards the high temperature endurance properties, even though the endurance lives of samples of the two technical methods decrease with the increase of the Hf content, yet the high temperature (1040°C) endurance life level of the H.R.S. method is higher than that of the P.D. method.

We believe that the differences in mechanical properties obtained by the two directional techniques are due to the differences of their local solidification speeds. The H.R.S. method's local solidification speed is relatively fast and thus the interdendritic arm distance is relatively small, the number of $\gamma / \gamma '$ eutectic phases is relatively small and the dimensions are also relatively small. Moreover, the segregation of the Hf is reduced (see Table 2) and the divergency of the grain orientation is also relatively small. All of these are beneficial in further raising the alloy's medium temperature and high temperature endurance properties.

IV. Conclusion

1. The Hf added in alloys is mainly segregated in the interdendritic regions and directly enters the $\gamma / \gamma '$ eutectic and $\gamma '$ phases. The Hf changed the solidification properties of the alloy and intensified interdendritic segregation causing the alloy's structure to undergo a series of changes: the

12

number of γ/γ' eutectic phases increased and there were morphological changes; there were changes in the grain boundary and interdendritic conditions; it changed the morphology and distribution of the carbides; new microfacies such as $MC_{(2)}$, Ni_5Hf, $(M,Hf)_2SC$ etc. appeared.

2. The addition of Hf can raise the alloy's 760°C transverse endurance and tension properties. The reason for this is primarily the large number of γ/γ' eutectic and coarse γ' phases changed by the Hf alloy distributed along the grain boundary and interdendritic regions. The advantageous distribution of the granular $M_{23}C_6$ and the effects of the Hf on the purification of grain boundary are also important reasons.

3. The alloy's high temperature endurance life decreases with the increases of the Hf content which appears to be mainly that the Hf causes an excessive amount of γ/γ' eutectic phases and lowers the high temperature stability of the γ' phase.

4. There is a noticeable influence of the directional technique on the alloy 's mechanical properties. The medium and high temperature properties of the H.R.S. method are superior to those of the P.D. method.

5. Giving consideration to the alloy's medium and high temperature properties and low costs, we consider that the suitable Hf content of this alloy is 1.0-2.0% (weight) and we should give priority to using the H.R.S. directional technique.

13

[1] Масленхов, С.Б., "Металловедение и Термическая Обработка Металлов", 1980.4. P45.

[2] Burton, C.J., "Superalloys, Metallurgy and Manufacture", 1976, p147.

[3] Cai Julin and Zheng Yunrong, "A Study of the Interdendritic Strengthening Mechanism of Casting Nickel Base High Temperature Alloys", (Internal materials), The Beijing Institute of Aeronautical Materials, 1977.8.

[4] Hund, C.H., et al, USP 3677331.

[5] Kotval, P.S., et al, Met. Trans., 3(1972), 453.

[6] Hockin, J. and Zund, C.H., USP 3677746.

[7] "A Study of the Patterns of Phase Changes of High Temperature Alloys in Solidification Regions", Laboratory 403 of Northwestern Polytechnical University, 1979.10.

[8] Duhl, D.N. et al, J. Metals, July, 1971, P38.

[9] Sims, C.T., J. Metals, 18(1966), P 1119-1130.

[10] Kear, B.H. et al, "The Microstructure and Design of Alloy_, 1973,8,p134.

[11] Doherty, J.E. et al, J. Metals, Nov., 1971, p59.

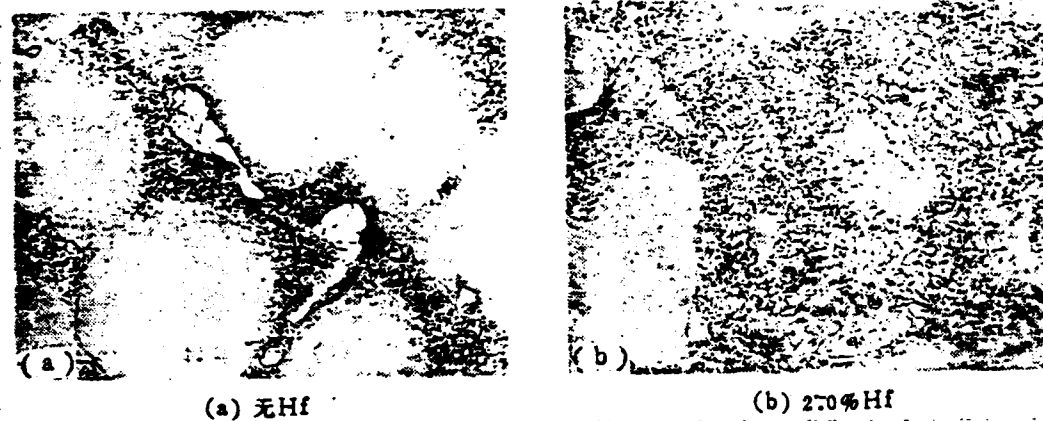(a) 无Hf   (b) 2.0%Hf

Fig. 2 Changes of r/r' eutectic phase morphology after adding Hf (P.D. method), x 500.

Key: (a) Without Hf.

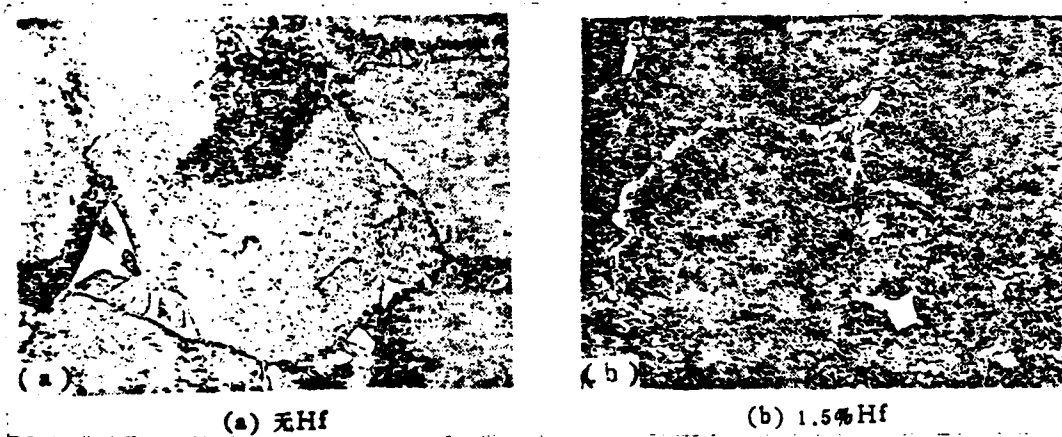(a) 无Hf   (b) 1.5%Hf

Fig. 3 Improvements of Hf on alloy grain boundary state (H.R.S. method), x 400.
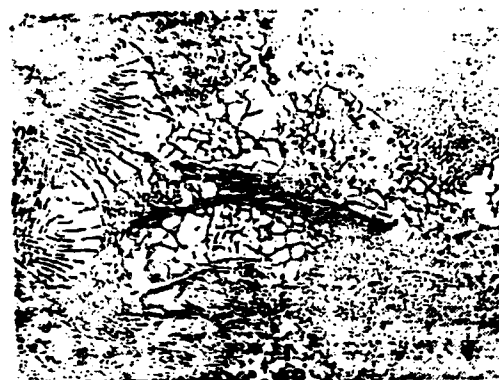
Key: (a) Without Hf.

15

Fig. 4   Strip shape in alloy containing 1.5% Hf, $(M, Hf)_2SC$
phase, x 500.

(a) 无Hf 纵向

(b) 无Hf 横向

(c) 2.0%Hf 纵向

(d) 2.0%Hf 横向
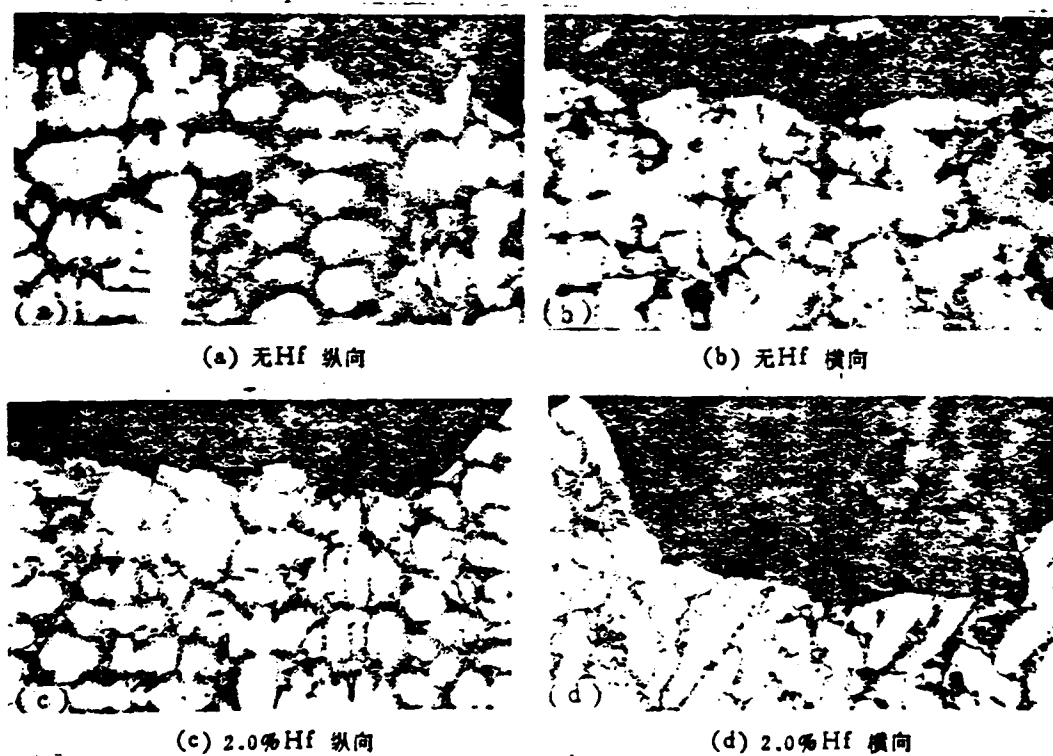
Fig. 6   Influence of Hf on medium temperature endurance crack

16

properties (P.D. method), x 50.

Key: (a) Without Hf, longitudinal; (b) Without Hf, transverse; (c) 2.0% Hf, longitudinal; (d) 2.0% Hf, transverse.

Fig. 7   The r/r' eutectic of a sample with 1.5% Hf is elongated in the 1040°C endurance process, x 1000.
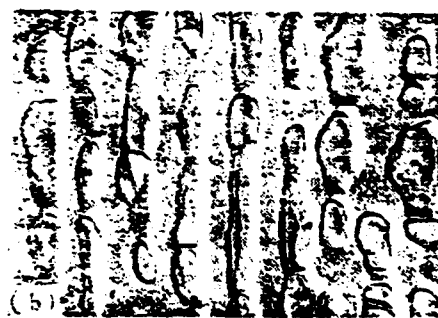
(a) 无Hf   (b) 2.0%Hf

Fig. 8   Influence of Hf on r' phase high temperature stability, x 10,000.

Key: (a) Without Hf.

17

Fig. 9   In the endurance tensile fracture sample, the remaining
         Ni_5Hf has holes and microcracks, x 800.

A STUDY OF THE TEMPERING TRANSFORMATION OF RETAINED AUSTENITE IN ISOTHERMAL QUENCHING STRUCTURES, "BAINITE TEMPERED EMBRITTLEMENT"

Wang Ping, Yang Zheng and Kang Mokuang
(Northwestern Polytechnical University)

Abstract

This paper determined the Ar tempering dynamics after 30CrMnSiNi2A steel isothermal quenching, carried out dynamic and static observations of tempering structures and studied the stability of Ar and tempered embrittlement in this steel. The results show that: the upper branch of the-C curve of Ar after isothermal quenching corresponds to the upper (or inverse) bainite transformation and the lower branch corresponds to the lower bainite or isothermal martensite transformation; the heat treating technique can control the stability of Ar; the major factors causing tempering embrittlement (especially in structures containing large amounts of Ar) are - Ar decomposition into upper (or inverse) bainite and the cementite film and temper-cooling and deformation transforming into martensite. After isothermal quenching, the workpiece should be tempered between 250-300°C.

It is well known that for certain alloy structure steel, because of the limitations of the hardenability, there can often exist a certain amount of bainite structure in the large dimension workpiece. At the same time, there also exists a relatively large amount of retained austenite (Ar) and the quenching workpiece must often be tempered. Therefore, it is necessarily related to the problem of Ar decomposition in structures primarily of martensite and bainite. Further, it is generally considered that the workpiece does not require tempering after isothermal quenching of bainite and we cannot

use the isothermal quenching method to lower the hardness [1] yet we have still not seen reports on its theoretical data. Although there have been previous material [2-5] on the isothermal quenching of alloy structure steel, especially the Ar tempering transformation in mixed structures predominately of bainite formed after bainite area isothermal quenching, yet they are very incomplete. Therefore, to study bainite quenching, it is especially important to study the tempering decomposition of Ar in mixed structures predominantly of bainite. The aim of this paper is to study the Ar temperature decomposition dynamics in the structure after quenching as well as its structure and the bainite tempered embrittlement, to investigate the influence of heat treatment on Ar tempering stability in order to provide theoretical data for the partial heat treatment technique of structural alloy steel and to find a tempering technique rational for the bainite structure.

Test Steel and Test Method

1. This paper used an ultrahigh tensile steel 30CrMnSiNi2A. Because this steel widely uses bainite or martensite isothermal quenching techniques in production, the large parts made by this steel possibly have bainite and Ar when in martensite area isothermal quenching or quenching oil and when there is tempering. It is also related to the problem of bainite structure and Ar tempering decomposition.

The chemical composition of the test steel is (weight %): 0.30C, 1.09Cr, 1.16Mn, 1.09Si, 1.51Ni, 0.09Cu, 0.004S and 0.011P. The preheat treatment standard is: 900°C normalizing + incomplete annealing (after keeping the temperature at 780°C, cool the furnace to 650°C and then maintain temperature at air cooling for 2 hours).

2. Test Contents and Method
(1) The Ar tempering decomposition dynamic curve. See

20

Table 1 for the pretreatment standards used for the tempering tests. In the table, the three groups of A, B and C are bainite area isothermal quenching and the D group is martensite area isothermal quenching [6]. The above mentioned test sample is serially temperature tempered in the Pb-Sn furnace of a thermomagnetic instrument. Afterwards, it is air cooled for 15 minutes, then we blow with cold wind for 5 minutes and use the x-ray recorder to record the changes in the magnetizing strength. After the sample was tempered, it was directly air cooled at 600±10°C and then the temperature was maintained for one hour.

(1) 编 号	(2) 预处理规范	(3) 预处理后 Ar量,%	(4) 回火温度,±5°C							
A	900±10°C, 10′ 390±10°C, 等温30′ (5)	24.4	260, 420,	280, 440,	300, 460,	320, 490,	340, 530,	350, 570*,	380, 600*	400,
B	900±10°C, 10′ 390±10°C, 等温1ʰ (6)	24.8	270, 470,	300, 510,	350, 550*,	410, 600*	430.	450.		
C	900±10°C, 10′ 390±10°C, 等温15′ (7)	23.2			260,	300,	340			
D	900±10°C, 10′ 240±10°C, 等温1ʰ (8)	14.1	250, 425,	280, 450,	300, 475,	325, 500*,	350, 550*,	375, 600*	400	

(9) * 在空气炉中回火1小时. 温度波动为±10°C.

Table 1 The heat treatment standard used in the tests.
Key: (1) Number; (2) Preheating standard; (3) Ar quantity after preheating, %; (4) Tempering temperature; (5)-(8) Isothermal; (9) When tempered in an air furnace for one hour, the temperature fluctuation is ±10°C.

(2) Structure observations and determination of blast toughness.. We carried out constant temperature static structure observation on a JEM-200CX for the samples with the above mentioned treatment standard which used metallic film. The metallic film made from A group pretreated standard samples was placed in an electronic microscope heating platform,

temperature was maintained at 500°C for 30 minutes and we directly observed the changes in the tempering process and photographed and recorded.

We used the V type notch sample to determine the blast toughness value after A group series temperature tempering.

Test Results
1. Transformation Mechanics of Ar Tempering
The C curve (solid line in Fig. 1) Ar tempering transformation of A group samples is divided into two branches and there is an Ar stability area between 350-400°C. Its lower branch curve has a nose section at 290°C which shows that at this time the inoculation period of the Ar decomposition is short. On the dynamic curve of tempering transformation there appear inflection points many times (Fig. 2) (this is possibly related to the carbon content level between each Ar microregion being different, the amount of carbon in each Ar microregion being nonuniform and the differences of the other physical conditions [3]). This shows that the tempering decompositon of Ar is a very complex process.

The form of the C-curve transformed by the Ar of the B group samples (the dotted line in Fig. 1) is the same as that of the A group. The difference is that its decomposition inoculation period is lengthened which is even more noticeable when it is in low temperature tempering. When tempered for one hour in the vicinity of 300°C (near the nose section), there is only a small amount of decomposition; but when tempered at 270 and 350°C, even if the temperature is maintained for two hours, there are no noticeable changes.
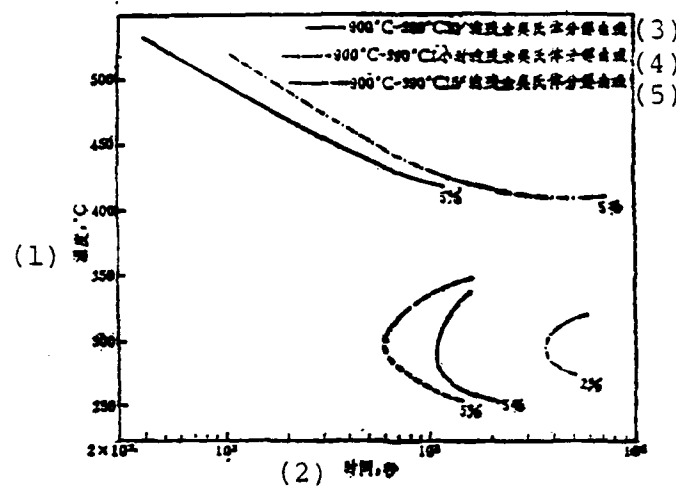
22

Fig. 1 The C-curve of Ar tempering transformation after isothermal quenching at 390°C and 900°C heating.

Key: (1) Transition; (2) Time, seconds; (3) Retained austenite decomposition curve; (4) Retained austenite decomposition curve of 900°C-390°C for one hour; (5) Retained austenite decomposition curve.
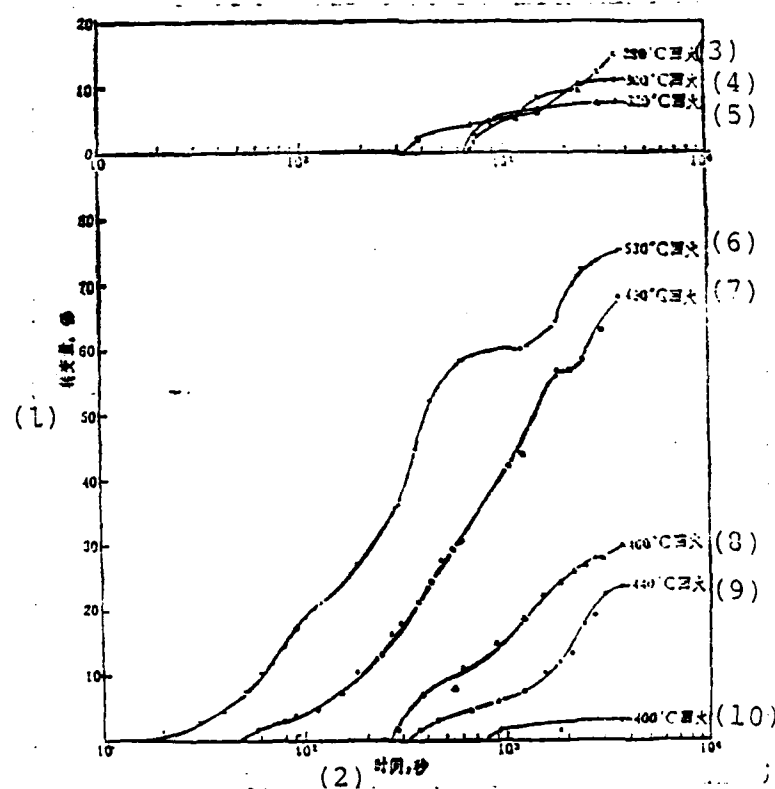

Fig. 2 (See next page)

23

Fig. 2 (continued) The Ar tempered transformation dynamic
curve [Ar(24.4%) is taken as 100%] after 390°C
isothermal quenching for 30 minutes and 900°C heating.

Key: (1) Transformation quantity; (2) Time, seconds;
(3) -(10) Tempering.

By comparing the test results (Fig. 1) of the A, B and C
groups of samples, we discover that the isothermal time can
influence the tempering decomposition dynamics of Ar. The
inoculation period of the Ar tempering decomposition also
lengthens with the increase of the isothermal time and the dif-
ference is especially noticeable when there is relatively low
temperature tempering.

The C-curve form (broken line in Fig. 3) of the Ar trans-
formation of the D group samples is similar to the C-curve of
the Ar transformation after martensite area isothermal quench-
ing; the difference is that the inoculation period of the former
decomposition is short. Moreover, there is also a small amount
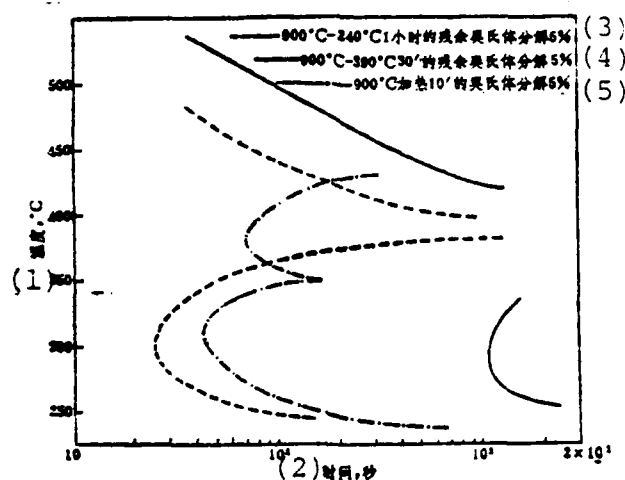of decomposition between 350-400°C.

Fig. 3 Comparison of the C-curves of the Ar transformation and
the original super-cooling austenite.

Key: (1) Temperature; (2) Time, seconds; (3) Retained
austenite decomposition of 5% at 900°C-240°C for one hour;
(4) Retained austenite decomposition of 5% at 900°C-390°C
for 30 minutes; (5) Austenite decomposition of 5% at 900°C
with heating for 10 minutes.

24

We can see from this test that the C-curve of the Ar after isothermal quenching is not the same as that of the original super-cooling austenite (Fig. 3). Firstly, above 400°C, a separate branch of the C-curve of the Ar transformation after isothermal quenching of this steel intersects with the transformed C-curve of the original super-cooling austenite. This is different from the research conclusions of researchers on certain steels [2,7]. Further, under 400°C, when compared with the original super-cooling austenite, the inoculation period of the Ar decomposition after bainite isothermal quenching is noticeably lengthened. The Ar does not decompose in the very long period of maintained temperature tempering and even though there is decomposition of a very small amount, this is different from past research results. However, after martensite isothermal quenching, the inoculation period of the Ar transformation is advanced and the pattern of transformation quantity decrease is the same as that of past research results. The dynamic data shows that the stability of Ar is noticeably raised after bainite transformation. The test results in references [2-4] can also prove this conclusion in this paper obtained from dynamic data.

2. Martensite Transformation in the Temper Cooling Process

In the tempering maintained temperature process, the Ar portion decomposes into bainite (its quantity is the bainite quantity in Fig. 4). The non-decomposed Ar can transform when in the following air cooling, its transformation starting point is low and therefore should be martensite [6] (its quantity is the martensite quantity in Fig. 4). Under relatively low temperature tempering, the Ar does not transform in the cooling process or the transformation quantity is very small; in tempering about 400°C, the quantity of martensite obtained during the cooling process increases with the maximum occuring when near 450°C. For tempering at even high temperatures, because the decomposition quantity of Ar in the tempering maintained

25

temperature process increases when followed by cooling, the
quantity of formed martensite decreases; when tempered at
about 570-600°C, the Ar is completely decomposed at maintained
temperature and therefore there is no further formation of
martensite during cooling (Fig. 4).

Fig.4(a) Transformation quantity of Ar with one hour of tem-
          pering after 390°C isothermal quenching for 30
          minutes and 900°C heating.

          Key: (1) Transformation quantity; (2) Tempering tem-
          perature; (3) Total transformation quantity;
          (4) Quantity of martensite; (5) Quantity of bainite.
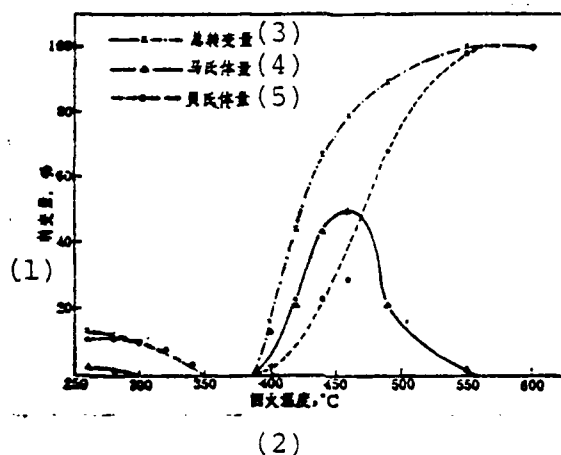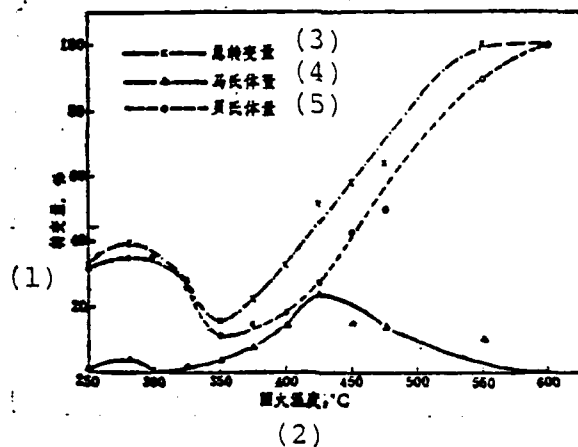

Fig. 4(b) Transformation quantity of Ar with one hour of tem-
           pering after 240°C isothermal quenching for one
           hour and 900°C heating.

           Key: (1) Transformation quantity; (2) Temperature tem-
           perature; (3) Total transformation quantity; (4)
           Quantity of martensite; (5) Quantity of bainite.

26

3. Dynamic and Static State Structural Observations

Optical and electronic metallographic static state observa-
tions show that the structure after 390°C isothermal quenching
is bainite and a relatively large amount of M/A (occupies
about 50%) [6] (see Fig. 5, Plate 3); the structure after 240°C
isothermal quenching is mainly martensite, there is still some
lower bainite, island and strip shaped M/A between the strips
(see Fig. 6, Plate 3). When there is 300 and below 300°C
tempering, the bainite base along with the M/A island has no
noticeable decomposition (see Fig. 7, Plate 3) which shows that
when there is bainite and M/A tempering, there is relatively
high stability. When there is 400°C and even higher temperature
tempering, the bainite body has noticeable traces of decomposi-
tion, the bainite carbide maintains its original shape (see
Figs. 8 and 9 (area 5), Plate 3) and the martensite of M/A has
noticeable decomposition, often in the center area of the
island. Even more important is the decomposition of Ar in the
M/A island: we separate out many chopping carbide pieces (Figs.
8 and 9, see Plate 4) in the Ar inserted between the bainite
and martensite strips; for the Ar decomposition in the island,
some carbides are separated out in their boundaries, become
chopping carbide film (Figs. 9 and 11, see Plate 4) and often
selecting the area of electron diffraction we reliably prove
that it is cementite (Fig. 11); some structural forms appear
as upper bainite (Figs. 8 and 10) and some are intermediate,
the backbone of the carbide. However, the inverse bainite is
surrounded on all four sides by a ferrite sheath (Fig. 9).

The dynamic state observations of an ultrahigh piezoelectric
mirror of the Ar transformation of the tempering process show
that: the Ar decomposition inserted between the bainite strips
form chopping carbide film (as shown by the arrow in Fig. 12,
see Plate 4) and the selected area of the electron diffraction
proves the separating out of the carbide (Fig. 12). At the
same time, during observations, we discovered that the cement-
ite or carbide have nucleation in certain areas of the Ar,

27

then grow larger in the austenite and the transformed product
assumes the form of bainite or inverse bainite.

4. Impact Toughness

Impact test results show that after isothermal quenching,
the structure also has noticeable tempering embrittlement.
Among them, the lowest impact value is about 450°C (Fig. 13).
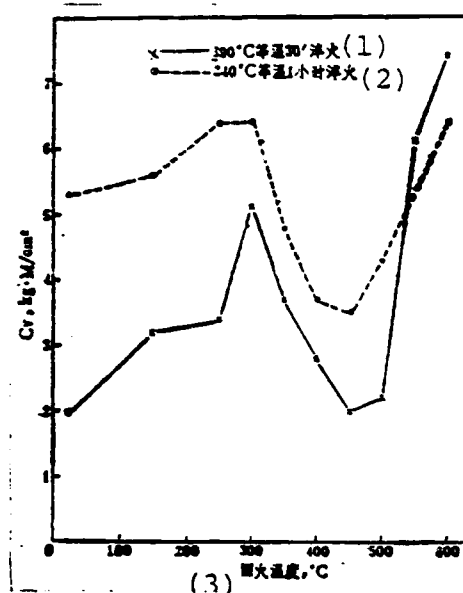
Fig. 13 Relationship of impact toughness and tempering
         temperature.

         Key: (1) 390°C isothermal 30 minute quenching;
         (2) 240°C isothermal quenching for one hour;
         (3) Tempering temperature.

Discussion

1. Ar Tempering Dynamics

Ar tempering dynamics research shows that below 400°C, the
Ar decomposition assumes an independent C-curve. At this time,
the body transformation activation energy is 12 kilocalories/
gram atom (the body transformation quantity of 5% for A group
samples) [6], the values of its dynamic curve form and body
transformation activation energy are both similar to isothermal
martensite and lower bainite. Its structually determined

28

composition still awaits study.

The transformation of Ar above 400°C appears complex, the body transformation activation energy of the reaction initial stage is 34 kilocalories/gram atom (the body transformation quantity for A group samples is 5%) [6] and for steel containing silicon, from the value of the activation energy, it possibly belongs to upper bainite type transformation [10]. Based on the estimations of reference [2], the carbon containing quantity of Ar after isothermal quenching of this steel can approximately increase to 0.6-1.2% which is the same as the carbon containing quantity of eutectoid and hypereutectoid steel. In eutectoid and hypereutectoid steel, the leading phase of the bainite can be ferrite, that is, produce normal bainite. It can also be lead by cementite and this type of structure is called inverse bainite [1]. Metallographical research points out that: tempering structure observations found the Ar transformation is a normal or inverse bainite formed structure (Figs. 8 and 9). From an analysis of the activation energy, structural form and Ar transformation dynamic state observations, the above branch curve possibly corresponds to the transformation of the upper (or inverse) bainite of the Ar.

2. The Influence of the Heat Treating Technique on Ar
   Stability

The Ar stability mentioned here includes its heat stability and mechanical stability. Here, we consider that the heat stability of Ar is the level of difficulty of it decomposing at different tempering temperatures. The mechanical stability of Ar then points to the level of difficulty of deformation bringing about phase changes under loading (deformation).

(1) After bainite transformation, the heat stability of Ar is raised. The C-curve of Ar reflects its heat stability. In the different structures obtained from the different heat treating techniques, the heat stability of Ar is different: the

Ar in the bainite area's isothermal quenching structure is higher than the heat stability of Ar in the martensite area's isothermal quenching structure (Fig. 3). However, the iso-thermal time is lengthened and the heat stability of Ar in the obtained structure is higher.

Because martensite and bainite phase changes have differ-ent special features, two types of Ar with different original conditions are created which influences the Ar tempering decom-position. Firstly, carbon is one of the important factors which influences bainite transformation and an increase in the quantity of carbon delays bainite transformation. Martensite phase changes do not exist in the redistribution of alloy elements and carbon atoms. Therefore, the alloy elements and carbon concentration in Ar is basically close to the concentra-tion in martensite; but when there are bainite phase changes, only the carbon atoms are redistributed, noticeably raising the carbon quantity in Ar and the distribution nonuniformity after it transforms. This postpones the transformation of Ar to bainite during tempering which causes the heat stability of Ar to be high after bainite area isothermal quenching.

Further, the tempering transformation of Ar is also a nucleation and nuclear growth process. The nonuniform nuclea-tion theory explains that the phase change easily has nuclea-tion on the grain boundary of the parent phase, fault, disloca-tion, vacancy and other crystalline defects. Because the volume effects of the martensite phase changes are larger than the bainite phase changes, after martensite transformation the Ar has more dislocations, quenching vacancies and other crystal-line defects than the Ar after bainite transformation. More-over, during tempering, the changes of the specific volume of the martensite are small which accelerates the Ar tempering decomposition. Further, because the tempering decomposition of Ar is checked by carbon atom diffusion, the dislocations and

30

and vacancies can accelerate the diffusion of the solute atoms
and therefore it is beneficial to Ar transformation after the
martensite phase changes. On the contrary, during the bainite
area isothermal quenching, because the temperature is high,
the carbon atom energy carries out diffusion (especially along
the dislocations) and is redistributed forming many Clausius
air masses which are not favorable to the rediffusion of the
carbon atoms during tempering, that is, not favorable to Ar
transformation. Therefore, the Ar heat stability is high after
bainite area isothermal quenching.

(2) The relationship of Ar heat stability and mechanical
stability during medium and low temperature tempering. Tests
show that Ar does not easily decompose in the 350-400°C range
(Figs. 1 and 4) but research on Ar mechanical stability shows
that between 350-400°C its mechanical stability is very low
[12] (Table 2) which can bring about martensite after deforma-
tion. This is possibly related to the composition of the micro-
region by different physical and chemical states. Because each
of the Ar microregion states is different, during tempering,
their manifested stabilities are different. The stability dif-
ferences in the 250-300°C tempering can have large amounts of
decomposition (Figs. 1 and 4) and this raises the mechanical
stability on the Ar macrostructure; when there is no tempering
or about 350-400°C tempering, these unstable Ar microregions
do not decompose but have phase changes during later deforma-
tion. Therefore, the mechanical stability is poor. This shows
that the heat stability and mechanical stability of Ar have a
certain inherent connection.

(1) 回火温度，°C	(4 未回火	200	250	300	350	400	500
(2) 回火后经0.2%变形时Ar转变量*，%	64	0	4.4	0	35.1	66.7	100

(3)° 油淬、回火后未变形时Ar量作为100%.

Table 2 (see next page)

31

Table 2 (continued) The relationship of Ar mechanical stabil-
ity and tempering temperature.

Key: (1) Tempering temperature; (2) Ar transformation
quantity* when there is 0.2% deformation after tem-
pering; (3)* The Ar quantity is 100% when there is no
deformation after oil quenching and tempering;
(4) No tempering.

3. Investigation of Bainite Tempered Embrittlement and
Tempering Technique

Research has discovered that the lowest value of tempering
impact roughness after isothermal quenching (Fig. 13) corres-
pond well with the Ar transformation being the upper (or
inverse) bainite quantity increase as well as the air cooling
transformation into the peak value of the martensite quantity
(Fig. 4). Moreover, tempering structure observations show
that the bainite body separates out a small amount of carbide
during the tempering process. The bainite carbide form and
distribution do not have any noticeable changes and therefore
the influence on the roughness is not large. In the M/A, the
martensite separates out cementite pieces at about 400°C [13]
and therefore in relatively low temperature tempering it can-
not cause the toughness to decrease. We believe that bainite
tempered embrittlement is mainly controlled by Ar tempering
decomposition as upper (or inverse) bainite, cut off carbide
film and the transformation into martensite when there is
deformation during the cooling and impact processes. When
there is tempering above 400°C, the M/A decomposes into upper
(or inverse) bainite, cementite pieces or film and thus causes
the impact value to lower; but after bainite area isothermal
quenching the carbon containing quantity of Ar is high, the
transformation into high carbon martensite when there is tem-
pering air cooling or deformation also causes the toughness
to decrease. Moreover, the distribution of these structures
between the bainite strips has even stronger effects. When
there is tempering in the 350-400°C range, its embrittlement is
mainly controlled by the deformation bring about martensite.

32

After martensite area isothermal quenching, the tempering
situations are basically the same. Therefore, the various
factors mentioned above cause tempered embrittlement and this
is especially the case for structures containing a relatively
large amount of Ar.

When tempering is done again at 300 and below 300°C after
bainite isothermal quenching, there are no noticeable changes
in the structural form and the Ar decomposed products are low-
er bainite or isothermal martensite which do not cause the
toughness to decrease. Moreover, suitable temperature temper-
ing can raise the mechanical stability of Ar. Therefore, the
workpiece with bainite contained in the bainite isothermal
quenching or quenching structure should be tempered in a 250-
300°C temperature area under guaranteed strength requirements
in order to obtain very good support of strong toughness.

Conclusion

Based on research on the Ar tempering dynamics and struct-
ural form dynamic and static state observations of
30CrMnSiNi2A steel, we can make the following several prelim-
inary conclusions:

1. After isothermal quenching, Ar tempering decomposition
is a complex process and its C-curve is separated into two
branches in this test's temperature region. The upper branch
is the upper (or inverse) bainite transformation and the lower
branch is the lower bainite or isothermal bainite transforma-
tion.

2. After isothermal quenching, the Ar transformation C-
curve is different from the original austenite. When tempered
below 400°C and compared to the original overcooled austenite,
after the martensite isothermal quenching, the C-curve of the
Ar shifts to the left but after bainite area isothermal quen-
ching, the C-curve of the Ar shifts to the right. After

bainite area isothermal quenching, the Ar stability is higher than the Ar stability after martensite isothermal quenching. For isothermal quenching under the same temperature, the isothermal time is lengthened causing the C-curve of Ar to shift to the right and the mechanical stability of the Ar tempered between 200-300°C is high. Therefore, the heat treatment can control the stability of Ar.

3. When there is tempered cooling, the quantity of Ar which transforms into martensite differs with the variations in temperature and it is maximum near 450°C. This is a factor which causes the tempered embrittlement of structures with relatively large amounts of Ar; when there is tempering in the 400-550°C range, the Ar decomposes into upper (or inverse) bainite and the carbide film is also a factor causing tempered embrittlement. However, when there is tempering in the 350-400°C range, the mechanical stability of Ar is poor which produces tempered embrittlement.

4. The workpieces after isothermal quenching and workpieces with bainite after other quenching which can be tempered at 300 and below 300°C can raise the impact value but tempering in the 250-300°C range is the relatively optimal tempering technique after isothermal quenching.

References

[1] Heat Treatment of Aeronautical Structure Steel, HB/Z5025-77, 1978.

[2] ЭHTИH, P.И., The Transformation of Austenite in Steel, China Industrial Press, 1965.

[3] Kang Mokuang et al, Physical Chemistry Test Communications (Physics Fascicle), 1979, No. 5-6, Pl.

[4] Шнеймерман, A.Ш., МИТОМ, 1978, No.12, P2.

[5] Cameron, J.A., JlSl, 183 (195-), NO. 3, P260.

[6] Wang Ping, Dynamics of 30CrMnSiNi2A Steel Isothermal Quenching and Tempered Austenite Transformation, Graduation Thesis of Masters Student of the Northwestern Polytechnical University, 1981.

[7] Yang Rang, Collection of Papers From the First All China Heat Treatment Annual Meeting of the China Mechanical Engineering Society, Machine Industry Press, 1966, P80.

[8] Entwisle, A.R., Met.Trans., 2A(1971), No. 9, P2395.

[9] Hawkings, M.J. and Bardord, J., JlSl, 210(1972), P97.

[10] Owen, W.S., TASM, 46(1954), P812.

[11] Kinsman,K.R. and Aaronson, H.I.,Met.Trans.,lA(1970), No. 5, Pl485.

[12] Huang Linqi et al, Martensite Tempered Embrittlement of 30CrMnSiNi2A Steel, Northwestern Polytechnical University Scientific and Technological Materials. 1982,No.8134.

[13] Liu Zhengtang, Study of Granular Bainite Tempered Embrittlement of 15CDV6 Steel, Graduation Thesis of Masters Student of Northwestern Polytechnical University, 1981.

Fig. 5   Photographs of 900°C10' - 390°C30' electron diffration.

Key: (a) Upper bainite + M/A island, (bright field),
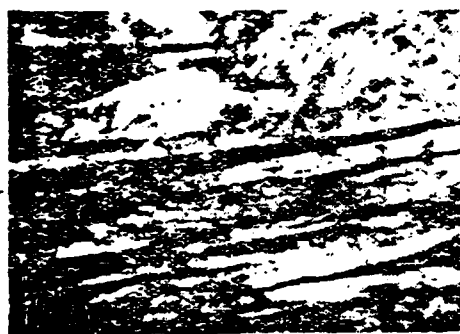x 15,000; (b) Electron diffraction spectrum of M/A island
in left figure.

Fig. 6   Photogragh of 900°C10' - 240°C1h electron diffraction
(bright field), x 22,0000, martensite + lower bainite
+ M/A.

Fig. 7   Photogragh of 900°C10' - 390°C30' - 300°C1h electron
diffraction (bright field), x 16,000, upper bainite
+ M/A.

Fig. 8   Photogragh of 900°C10' - 390°C30' - 500°C1h electron
diffraction (bright field), x 26,000. The chopping
carbide film between the lower bainite and strips
(pointed to by the arrows) assumes a shape similar to
that of upper bainite.

37
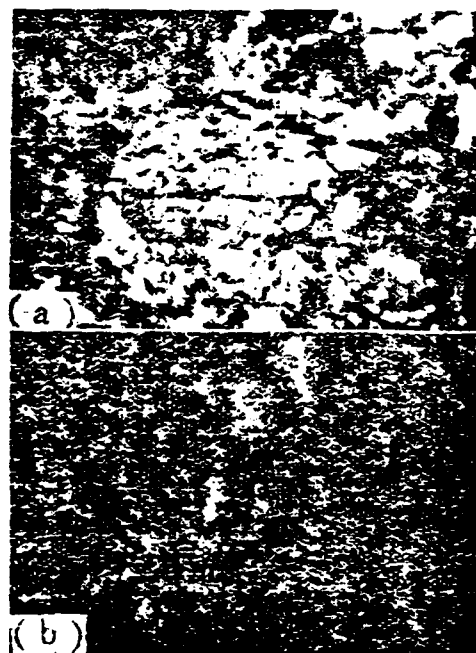
Fig. 9 Photographs of 900°C10' -390°C30' - 500°C1h electron
diffraction. In the M/A island, M decomposition (area 1)
and Ar decomposition products assume shapes on the B
(area 2) and B (area 3). The Ar decomposition product on
the side of the island is a spheroidal cementite chopping
film (area 4).

Key: (a) Bright field, 22,000; (b) Dark field.
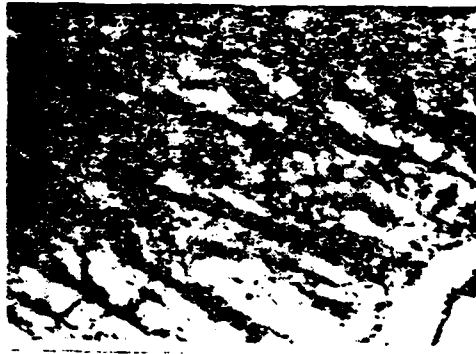
Fig. 10 Photograph of 900°C10' - 240°C1h - 450°C1h electron
diffraction (bright field). The Ar between the bainite
and strips separates out the carbide pieces (pointed to
by the arrows) and assumes a shape similar to that of
the upper bainite.
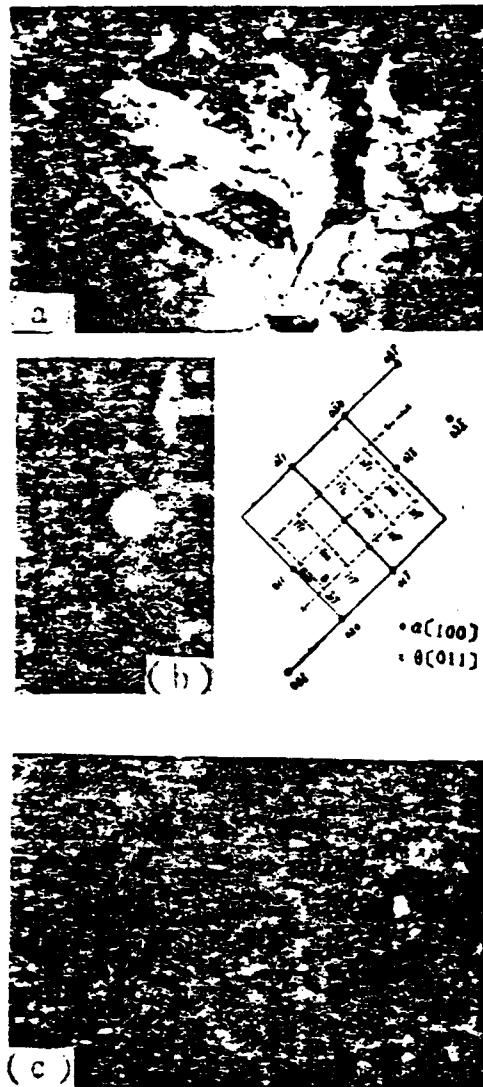
Fig. 11   Photographs of 900°C10' - 390°C30' - 450°C1h electron
diffraction.   The M/A island has side decompositon.

Key: (a) Bright field, x 36,000; (b) Electron diffraction
spectrum; (c) Photograph of point B dark field.
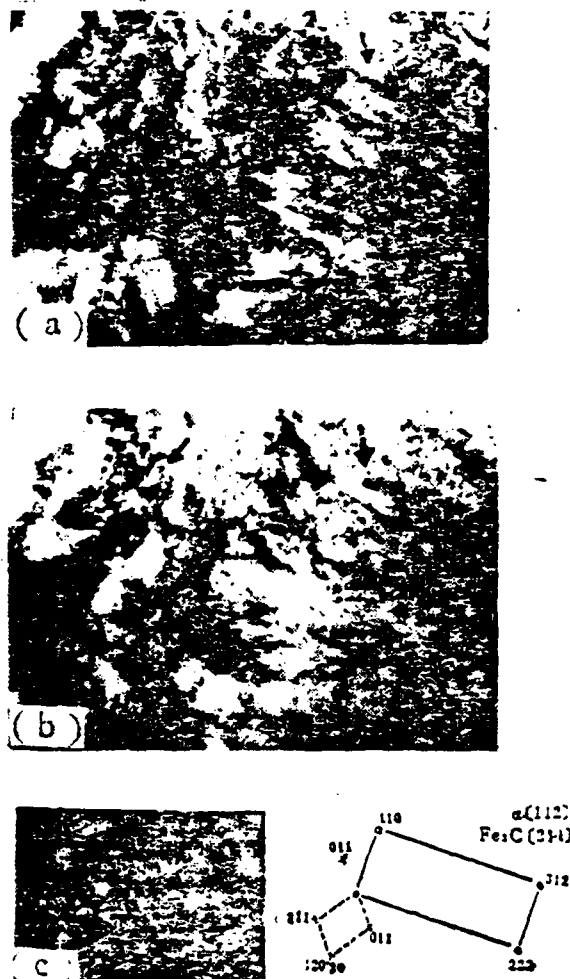
Fig. 12   Photographs of Ar decomposition (pointed to by the
          arrows) and Ar tempering dynamic state observations of
          electron diffraction.

          Key: (a) x 1000, photographed in 900°C - 390°C30' at
          room temperature. Upper bainite + M/A (pointed to by
          arrows); (b) 1000 x, field of vision same as (a),
          photographed at 500°C after 500°C tempering 21';
          (c) Selected area electron diffraction spectrum in Fig. b.

THE EFFECTS OF SOLID SOLUTION TEMPERATURES AND COOLING RATES ON THE MICROSTRUCTURES OF BT3-1 TITANIUM ALLOY

Zhang Shaoqing and Huang Heng

Abstract

We used x-rays, optical metallography and transmission electron microscopy to study the effects of various heating temperatures and cooling rates (water quenching, air cooling and furnace cooling) on the microstructures of BT3-1 titanium alloy. The α" martensite was formed by water quenching from β field temperatures; the α" and α phases were obtained by water quenching from upper temperatures of the $(\alpha + \beta)$ phase field; the α and β phases were obtained by 850°C water quenching. We also investigated the lattice constant changes of the α" martensite as well as substructure and hardness changes. We obtained the various morphologies of the α and β phases from various solid solution temperature air cooling or furnace cooling.

a", a and β phases can be obtained by 900°C water quenching;

I. Preface

The BT3-1 alloy is a martensite type $\alpha + \beta$ two phase titanium alloy which can operate for a long time below 400°C and be used in aviation turbojet engines. Based on usage and requirements for performance, the heat treatment of the BT3-1 alloy can be isothermal annealing, double annealing, strengthened heat treatment and high temperature deformation heat treatment etc. This alloy can carry out pressure processing in the β phase field or the $\alpha + \beta$ two phase field temperatures. In order to rationally formulate the heat processing technique as well as understand the effects of different structural states on performance, it is necessary to make clear the microstructures of this alloy under different solid solution treatment temperatures and different cooling rates. This is of real reference value to the development and use of this

42

alloy. The Soviet Union already has reference reports [1-5]
on the effects of solid solution temperatures and cooling rates
on the microstructures of BT3-1 alloys yet most are the anal-
ysis results of x-ray phases and have contradictions. The
reports on microscopic forms, especially observation results
from transmission electron microscopes, are even more de-
ficient.

II. Raw Materials and Test Method

The chemical composition of the 20 millimeter diameter BT3-1
alloy bar used in this test is:

Element	Al	Mo	Cr	Fe	Si	C	O	H
Quantity,%	6.56	2.53	1.97	0.45	0.25	0.15	0.09	0.01

Element	N	T
Quantity,%	0.0006	remainder

The bar was cast in the $\alpha + \beta$ phase field at about 940°C.
The metallographic structure is a small isometric $\alpha + \beta$
structure. We cut a 10x12mm diameter sample from this bar and
the sample carried out solid solution processing in a box
muffle furnace. The heating tempera tures were separately 1000,
980, 970, 960, 940, 900 and 850°C, the maintained temperature
time was always one half hour and afterwards we carried out
water quenching (WQ), air cooling (AC) and furnace cooling (FC).

In the tests, we used x-ray diffraction, optical metallo-
graphy, transmission electron microscopy and electron probe
etc. measures. The x-ray diffraction was carried out on an
RU-200 rotating anode x-ray diffraction instrument and used a
CO target. The microfield component was determined on an a JXA-733
electron probe and the instrument directly provided quantita-
tive analysis results. We used the JEM-200A transmission
microscope to observe the BT3-1 alloy and the acceleration
voltage was 200kv.

43

III. Test Results and Discussion

3.1 Test Results

(1) X-Ray Diffraction

X-ray diffraction results show that the BT3-1 titanium alloy has three phases: the α phase of the hexagonal lattice, the β phase of the body-centered cubic lattice and the α" phase of the orthogonal lattice.
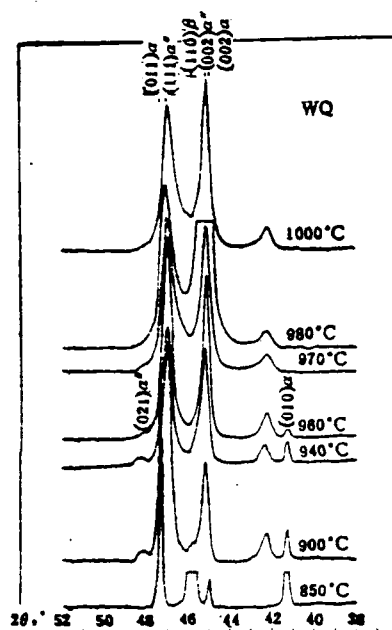
Fig. 1 X-ray diffraction chart of water quenched sample, Cokα

Figure 1 is an x-ray diffraction chart of the water quenched sample. We can know from Fig. 1 that from 1000, 980 and 970°C water quenching, we only form a single α" martensite phase. Because the (002) α'" peak and (111) α" peak local phases superimpose eachother, two peaks with unsymmetrical forms are created. We obtained the α and α" phases from the 960 and 940°C water quenching. The (002) α peak and (002) α" peak, and the (111) α" and (011) α peak of 960°C water quenching as well as the (002) α peak and (002) α" peak of 940°C water

quenching overlapped. In the 900°C water quenched sample, there were the α, α'' and β phases and the (002) α peak and (002) α'' peak and the (111) α'' peak and (011) α peak overlapped. We only found the α and β peaks from the 850°C water quenching.

There were only the two phases of α and β in the air cooling and furnace cooling samples. Table 1 lists the phase compositions obtained from the x-ray diffraction results under different solid solution temperatures and cooling rates.

	1000°C	980°C	970°C	960°C	940°C	900°C	850°C
WQ	α''	α''	α''	α'',α	α'',α	α'',α,β	α,β
AC	α,β	α,β	α,β	α,β	α,β	α,β	α,β
FC	α,β	α,β	α,β	α,β	α,β	α,β	α,β

Table 1 Phase compositions of BT3-1 titanium alloy.

See Fig. 2 for the relationship of the martensite α'' phase lattice constant and the quenching temperature. Following the rise of the quenching temperature, α decreases and b and c rise.
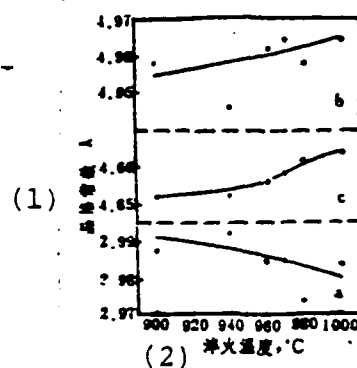

Fig. 2 Relationship of the α'' phase lattice constant and the quenching temperature.
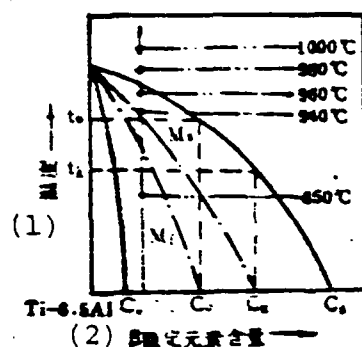Key: (1) Lattice constant; (2) Quenching temperature.

Fig. 3   Schematic of the pseudobinary state of the BT3-1 alloy.
Key: (1) Temperature; (2) β stable element quantity.

(2)   Optical Metallography

Figure 3 is a schematic of the pseudobinary state of the BT3-1 titanium alloy. The figure notes each of the heating temperatures. The metallographic structures obtained after water quenching, air cooling and furnace cooling are shown in Fig. 4 (see Plates 5 and 6).

We obtained the needle shaped martensite α" phase structure from 1000 and 980°C water quenching. Each bundle of martensite chips were perpendicular to eachother or intersected at different angles (Figs. 4a and d). The structure of the 960 and 940°C water quenched samples were composed of sheet α" martensite and isometric primary α and the primary α phase is distributed on the martensite base (see Figs. 4g and j). From 900°C water quenching, we can find the small sheet martensite and from 850°C water quenching, we obtain the isometric $\alpha + \beta$ structures (see Fig. 4m). We can see from the metallographic structure that following the decrease of the quenching temperature, the martensite chip gradually becomes small. Among the 960°C water quenched samples, we found the isometric primary α phase. The lower the quenching temperature, the greater the quantity of primary α phase.

We obtained the woven shaped Widmanstaetten structure from 1000 and 980°C air cooling. In the original β crystal, there are a large number of thin, long, flat and straight sheet phases and there are β phase thin sections between the α phases (see Figs. 4b and e). We obtained the isometric primary α phase and β transformation structure with small needle from 960 and 940°C air cooling (Figs. 4h and k). However, the isometric α and β structures exist in the 850°C air cooled samples (Fig. 4n).

We obtained the flat and straight juxtaposed Widmanstaetten structure from 1000 and 980°C furnace cooling. The sheet were relatively long and thick and were arranged parallel to each other. The clusters formed one by one in the original β crystal grain (Figs. 4c and f). The 960 and 940°C furnace cooled samples had coarse and large isometric α and coarse strip α and the β phases were between the α phases (Figs. 4i and l). We obtained isometric $\alpha + \beta$ from 850°C furnace cooling (Fig. 4o).

(3)   Transmission Microscope Film Observations

The observation results of the water quenched samples are shown in Fig. 5 (see Plate 7). Figs. 5a, b and d show the shape of the α'' martensite chip. However, there are also some martensite fields which do not have noticeable chips but appear as indistinct dirty spots (Fig. 5e). There are dislocations in the α'' martensite which decrease with the quenching temperature. There are relatively noticeable microtwin crystals in the α'' sheet (Fig. 5d). It is worth paying attention that there exists a strong expanded stripe on the electron diffusion spot of the α'' quenched martensite (Figs. 5c and f). We initially considered that this was due to the formation of the ω phase during quenching. We obtained the isometric α and intercrystalline β phases from 850°C quenching and there were twin crystals among them (see Fig. 5g).

47

Figure 6 (see Plate 8) gives the microscopic appearance of the air cooled sample. There were dislocations and twin crystals in the sheet α phase formed from 1000°C air cooling and secondary α phases in the β phase transformation fields between the α sheets (Fig. 6a). The primary α phase, sheet α as well as β transformation structures were formed by 960°C air cooling and there were dislocations and twin crystals in the sheet α (Fig. 6b). We obtained isometric α and β structures from 850°C air cooling and the β phase had twin crystals (Fig. 6c).

The microphotograph of the air cooled sample is shown in Fig. 7 (see Plate 8). The α strip of the 1000°C furnace cooled sample had twin crystals and twin crystals were also found in the β phase field. Further, there were interface phases between the α and β phases (Figs. 7a and b). The situation of each phase of the 960°C furnace cooled sample were also roughly like this.

(4) Analysis of Electronic Probe Microfield Composition

Figure 8 is the relational curve of the alloy element content in the α " martensite phase and the quenching temperature. Following the use of the quenching temperature, the molybdenum, chromium, iron and silicon content in the α " phase decreases but the aluminum content rises. The composition of the 900°C water quenched sample is the mixed composition of the α and β phases.
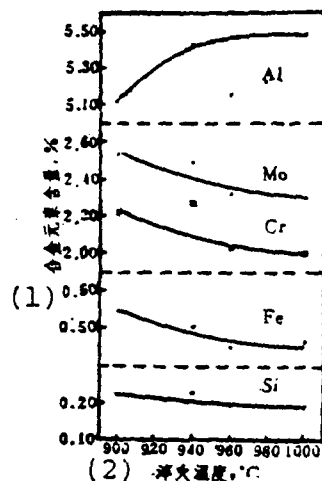
Fig. 8   Relationship of the alloy element contents in a'' phase and the quenching temperature.

Key: (1) Alloy element content; (2) Quenching temperature.

3.2   Discussion of Test Results

(1) Determination of $(a+\beta)/\beta$ Phase Change Temperature

In order to determine the $(a+\beta)/\beta$ phase change temperature of the BT3-1 alloy bar used in this test, we referred to the x-ray diffraction and metallographic observation results. In the diffraction spectrum of 970°C water quenched samples there was only the diffraction peak of the a'' phase but in the diffraction spectrum of 960°C water quenched samples, the diffraction peak of the a phase appeared (Fig. 1). Correspondingly, in the metallographic structure, there was only a'' martensite among the 970°C water quenched samples but aside from the a'' martensite among the 960°C water quenched samples there was also the primary a phase. Therefore, we can determine that the $(a+\beta)/\beta$ phase changing point of the BT3-1 alloy is between 960-970°C, about 965°C.

(2)   The Quenching Phase Change of BT3-1 Alloy and Its Structure

1) The $\beta \to \alpha$ " martensite transformation. During water quenching, the BT3-1 alloy occurrence of $\beta \to \alpha$ " transformation is carried out by the shearing method. The martensite phase change of $\beta \to \alpha$ " is explained as follows:

Figure 9a shows the lattice relationship of the $\alpha(\alpha')$, α " and β phases. The α " phase and β phase have the following directional relationship: [100] β corresponds to [100] α ", [01$\bar{1}$] β corresponds to [010] α " and [011] β corresponds to [011] α ". When there is water quenching, because there is not enough time for diffusion, the transformation of $\beta \to \alpha$ " is completed by the following steps: compression along the [100] β direction and expansion along the [01$\bar{1}$] β and [011] directions (Figs. 9b and c). The $\beta \to \alpha$ " transformation can be viewed as the $\beta \to \alpha$ ' transformation still not thoroughly carried out but the state of having stopped halfway [6,7]. Following the use of the quenching temperature, lattice constant α of the α " phase decreased, b and c rise (Fig. 2) and the molybdenum, chromium, iron and silocon contents decrease (Fig. 8). The molybdenum, chromium, iron and silicon are displaced and dissolved in the solid solution. Their atom radii are smaller than the atom radii of titanium and the smaller the quantity dissolved in, the smaller the lattice distortion and the larger the lattice constant. Therefore, following the rise of the quenching temperature, b and c increase. Following the rise of the quenching temperature, the β stable element content in the β phase lowers and the phase change resistance decreases causing the shearing to be carried out thoroughly. That is, contraction along the [100] β direction, expansion along the [01$\bar{1}$] β and [011] β directions (separately corresponding to [100] α ", [010] α " and [001] α " is obtained more which reduces a but b and c increase. The reduction of α of the 900°C water quenched samples with b and c increasing is related to the segregation of the β stable elements. During cooling, the field of the β-rich stable

elements becomes the remaining β phase but the field of the β -poor stable elements produces $\beta \rightarrow \alpha$ " transformation. Because of this, the alloy element contents in the α " phase decrease causing a to decrease and b and c to increase.

After the BT3-1 alloy used in this test goes through water quenching near the phase change point, the x-ray diffraction has not determined a β phase but only an α " phase. This can be explained by the schematic in Fig. 3: the β phase stable element contained in the BT3-1 alloy is smaller than Co and at this time the M_f point is higher than room temperature. After water quenching, it can cause the β phase to completely transform into the α " phase.
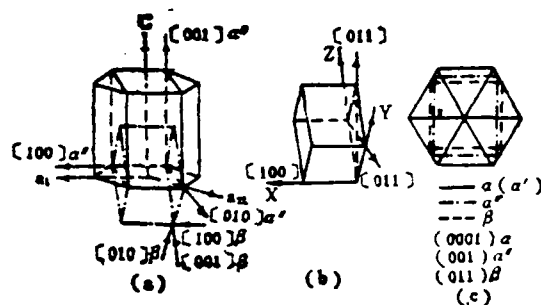

Fig. 9 Relationship of the α , α " and β phases.
Key: (a) Lattice relationshp; (b) Deformation direction; (c) Deformation results.

As regards the water quenched martensite structure of the BT3-1 alloy, some references report it as the α " phase [4,5] while other papers point to the a' phase of the closely arranged hexagonal lattice formed when there is temperature water quenching near the ($a + \beta$)/β phase change point [2,3]. This test obtained α " martensite. The quenching formed α' or α " martensite has a very strong relationship with the β stable element content in the alloy. As regards the Ti-Mo alloy, when the β stable element content exceeds a certain critical concentration ($\sim$ 4%), the martensite

structure transforms from the hexagonal lattice to the ortho-
gonal lattice [8]. The past contradiction regarding the water
quenched martensite structure of the BT3-1 alloy was possibly
due to the changes of the element contents in this alloy. In
the Soviet Union, the molybdenum content in the later produced
BT-3-1 alloy was raised [1] and the molybdenum content in the
alloy which was used by the author to obtain the α'' phase
tended to be high. When martensite transformation occurred,
the atoms in the β phase made collective and patterned short-
range migration. The migration distance when $\beta \to \alpha''$ trans-
formations occur are shorter than when there are $\beta \to \alpha'$
transformations (Fig. 9c) and thus the produced strain is small
and the strain energy is also small. When the β stable
element content is relatively high, the β phase is stable, the
phase change resistance is relatively large and the volume free
energy is poor, only being able to supply the driving force of
the $\beta \to \alpha''$ transformation and thus producing $\beta \to \alpha''$ trans-
formation. This is the situation of the martensite transform-
ation in the BT3-1 alloy.

2) The fine structure of α'' martensite. Most of the
references consider that there are twin crystals contained in
α''. The observations of this test show that the twin crystals
in 960°C water quenched samples are more noticeable than those
of 1000°C water quenched samples, yet the dislocation density
has decreased. This is because following the decrease of the
quenching temperature, the molybdenum content in β increases,
the Ms point decreases, the critical shearing stress of twinning
decreases and the critical shearing stress of the slip rises.
The lattice unchanged shearing method transforms from slipping
to twinning which causes the twin crystals to increase [8].

It was discovered in this test that strong expanded strips
exist on the electron diffraction spots of the α'' martensite.
Many references report that when there is β alloy quenching,

52

this can form the heatless ω phase and in the initial stage of its formation, strong strips appear on the electron diffraction spectrum of the quenching phase [9,10]. Because the α " phase is located in the transition state from β to α, the ω phase can also appear in α". As mentioned in Reference 7, it seems that the ω phase forms when in BT3-1 quenching yet its formation is still unable to be seen with an electron microscope.

3) The hardness of the α" martensite and the total hardness of the alloy. Based on the report in Reference [2], after the BT3-1 alloy is water quenched near 920°C, they obtained the minimum value of $\sigma_{1.2}$, σ_b and the hardness. These authors generally classified the lowering of the strength and hardness to the formation of the α" phase yet have not yet made detailed explanations. This test showed that the higher the quenching temperature, the more the α" phase. After the temperature is higher than the phase change point, we only obtain the α " phase. In quenching below the phase change point primary α phase appears and its number increases with the decrease of the quencing temperature. Aside from this, the remaining β phase also appears. We determined the hardness of this test's alloy α" phase and the overall hardness of the alloy. The results are shown in Fig. 10. The test shows that following the lowering of the quenching temperature, the hardness of the α" phase decreases and the hardness value of the 940°C water quenched α" phase reaches the minimum value (Fig. 10a).
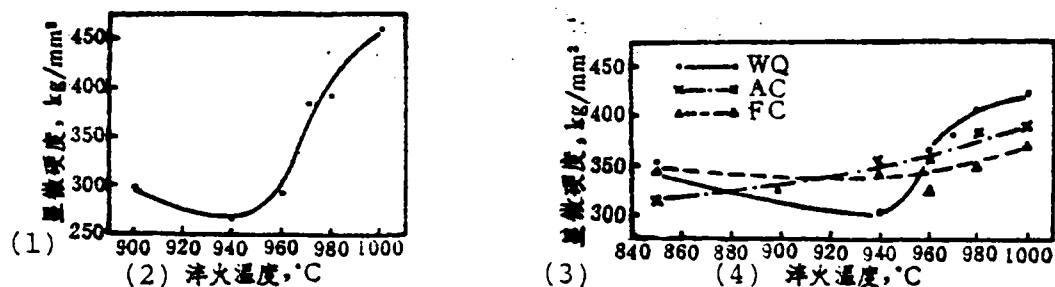
Fig. 10 Hardness of the BT3-1 alloy.

Key: (a) Relationship of microhardness of a " phase
and quenching temperature, load 50 grams;
(b) Relationship of overall hardness of the alloy
and the solid solution temperature, load 200 grams;
(1) Microhardness; (2) Quenching temperature;
(3) Microhardness; (4) Quenching temperature.

The explanation of the a" hardness changes is as follows:
the reason why the quenching temperature as well as the hard-
ness value are high is the formation of the ω phase and the
dislocation density is high; following the decrease of the
quenching temperature, the dislocation density in the a" phase
decreases, twinning deformation easily occurs and the volume of
the a" phase has a percentage decrease because of the appear-
ance of the primary a phase which promotes the decrease of the
hardness value.

Figure 10b shows that with water quenching from temperatures of 960°
and higher, the hardness of the a" phase is higher than that of the a and b
phases (only a and β phases are included in Ac and Fc samples) but with water
quenching from temperatures below 960°C the hardness of the a" phase is then
less than that of the a and β phases. We can know from Figs. 10b, 4b, c and
c, f that the hardness of the thin section a phase is larger than the hard-
ness of the thick section a phase; but the hardness of structures with
isometric a phases is somewhat lower. The overall minimum hardness of the 940°C
water quenched samples is related to the minimum hardness of the a" phase.

54

The upwards return of the overall hardness of the below 940°C temperature water quenching is related to the lowered of the α and β phases.

(3) The $\beta \rightarrow \alpha$ Phase Changes of the BT3-1 Alloy

When the BT3-1 alloy is being slow cooled, the separating out of the α phase from the β phase uses the nucleation growth method to carry out $\beta \rightarrow \alpha$ difffusion phase changes. Air cooling can satisfy the conditions of the $\beta \rightarrow \alpha$ transformation. The solid solution temperature and cooling rate control the shape and size of the alloy structure. When there is β and ($\alpha + \beta$) phase area temperature air cooling and furnace cooling, the α phase nucleates in the easily nucleated β grain boundary and primary α interface. This is possibly due to the thermal stagnation of the air cooling being larger than that of the furnace cooling and the critical nucleation power is small causing the nucleation rate during air cooling to be greater than the nucleation rate during furnace cooling. Thus, during air cooling, the α phase can also have a large amount of nucleation in the β grains and therefore the air cooled structures are smaller than the furnace cooled structures. Beeause the cooling rate of air cooling is relatively fast, atom diffusion cannot be completely carried out, the β phase decomposition and separated out α phase cannot fully grow and thus we obtain fine stripped β transportation structures. Because the cooling rate of furnace cooling is relatively slow, α phase nucleation attains to full growth thus forming coarse Widmanstaetten strip structures.

IV. Conclusion

1. The α" martensite phase is formed from β phase field temperature water quenching. We obtained the α and α" phases from the temperature water quenching near the ($\alpha + \beta$) phase field phase change point. We obtained the α, α" and β phase

55

from 900°C water quenching. In 850°C water quenching, we were only able to form the α and β phases.

The sheet α" martensite structure becomes small following the decrease of the quenching temperature, the dislocation density decreases and twin crystals appear.

2. The α" martensite is an orthoganal lattice, its lattice constants b and c increase with the rise of the quenching temperature and α becomes small, forming a close to hexagonal lattice α' phase. Following the rise of the quenching temperature, the β stable element contents in the α" phase decrease.

3. The hardness of the α" martensite decreases with the lowering of the quenching temperature and reaches the minimum value at 940°C. When there is above $(\alpha + \beta)/\beta$ phase change point temperature quenching, the α" phase gives a very high hardness value.

4. We always obtained the two phase $(\alpha + \beta)$ structures from the solid solution temperature air cooling or furnace cooling. We obtained the mean value thin section α phase and β transformation structures between the sections from the temperature air cooling on the β phase field and $(\alpha + \beta)$ phase field. Isometric primary α phases occur at lower than β transformation temperature cooling and its quantity increases with the lowering of the solid solution temperature. We obtained coarse sheet α from the temperature furnace cooling on the β phase field and $(\alpha + \beta)$ phase field and in the original β crystal they form bunched structures and there are β phase thin layers between the α sections. The α phase becomes more and more isometric following the lowering of the solid solution temperature.

References

[1] O. π.Suolangningna and C. Γ. Gelazunuofu, Heat Strong
    Titanium Alloys, translated by Zhang Zhifang and
    Ge Zhiming, Beijing Institute of Aeronautical Materials,
    P129-137.

[2] M. H. Yeerrongluwa et al, Collection of Foreign Papers on
    Titanium Alloys, Translated by the Huanghe Smelting
    Factory, Metallurgy Industries Press, P118.

[3] Локшин,Ф.Л.и др., Новый Конструкционный Материал-титан, изд. (наука),
    (1972),   p78

[4] Дьякова М.А.и др.,Физика металлов и металловедение,том.42.вып.2,(1976), p333.

[5] Львова Е.А.и др., Металлы, изв.АН СССР, No.1,(1979), p154.

[6] Hisaoki Sasano et al, Titaium'80 Science and Technology,
    Proceedings of the Fourth International Conference,
    1(1980), P717.

[7] Duering, T.W., Titanium'80 Science and Technology,
    Proceedings of the Fourth International Conference,
    2(1980), P1503.

[8] Dawis, R. et al, Journal of Materials Sciencl, 14(1979).
    P712.

[9] Williams, J.C. et al, Met. Trans., 4(1973), No.12, P2701.

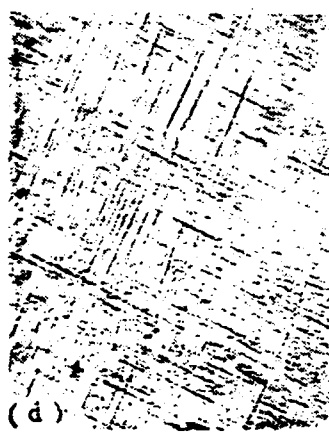[10] Min chung Jon et al, Metallography, 5(1972), No.2. P139.
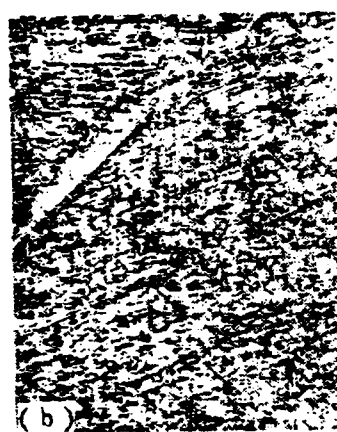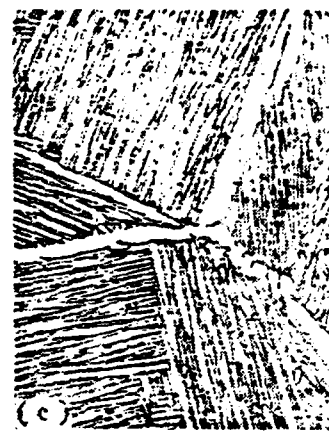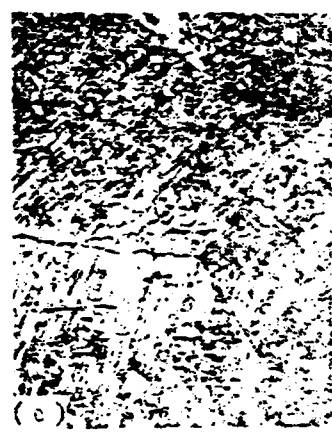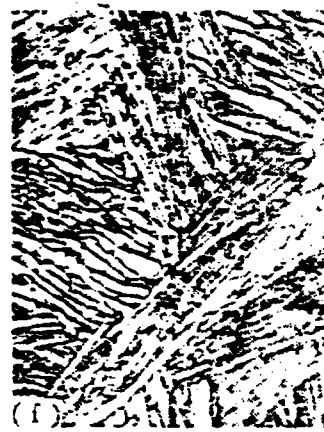
(a) 1000°C WQ (b) 1000°C AC (c) 1000°C FC

(d) 980°C WQ (e) 980°C AC (f) 980°C FC

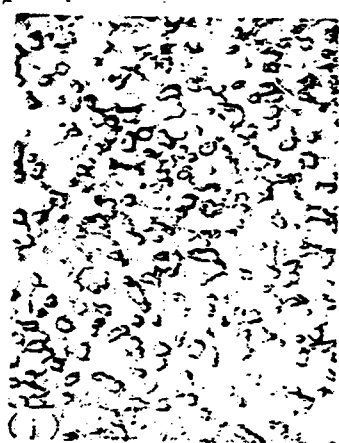(g) 960°C WQ (h) 960°C AC (i) 960°C FC
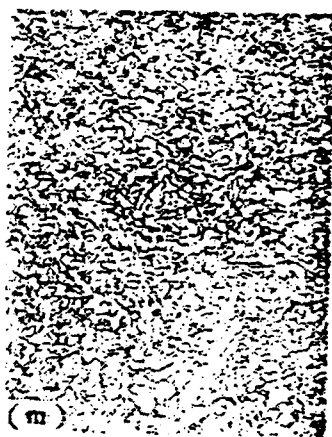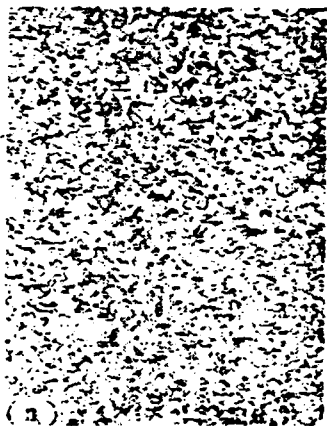
Fig. 4 (cont. on next page)

(j) 940°C WQ   (k) 940°C AC   (l) 940°C FC
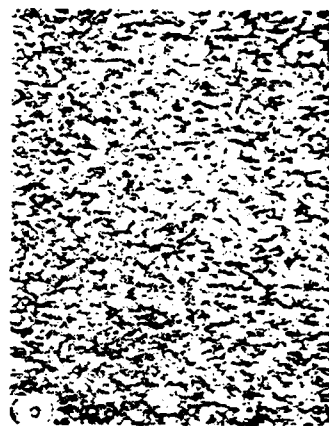
(m) 850°C WQ   (n) 850°C AC   (o) 850°C FC
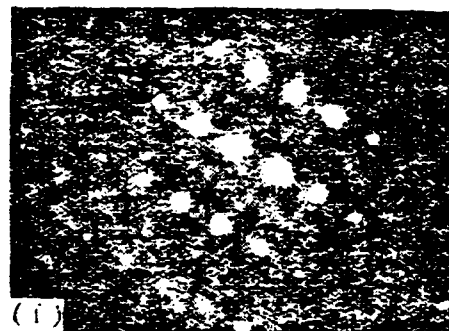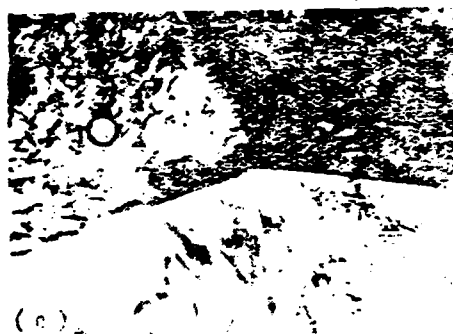
Fig. 4 Metallographic structures of BT3-1 alloy, x 500.
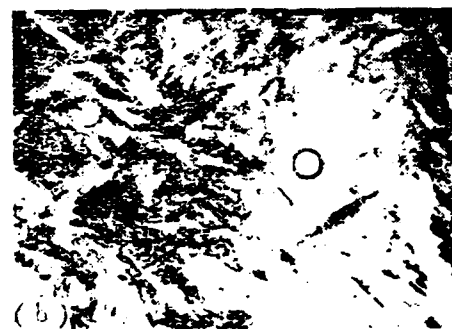
(a) 1000°C　WQ　×24000:

(b) 1000°C　WQ　×38000:

(1) (c) b照片所示区域的电子衍射谱，为〔111〕β
晶带轴和＜110＞α″晶带轴，有强度条纹;

(d) 960°C　WQ　×38000:

(e) 960°C　WQ　×38000:

(2) (f) e照片所示区域的电子衍射谱，为〔134〕α″
晶带轴，和＜212＞α″晶带轴，有强度条纹:

(g) 850°C　WQ　×6000

Fig. 5　Transmission electron microscopic photographs of the film of the water quenched sample.

Key: (1) (c) Electron diffraction spectrum of area shown
in photo b which is the [111] β zone axis and $\langle 110 \rangle$ a"
zone axis has strong stripes; (2) (f) Electron diffraction
spectrum of area shown in photo e which is the [134]a"
zone axis and $\langle 212 \rangle$ a" zone axis has strong stripes.

图 6 空冷试样的薄膜透射电镜照片
(a) 1000°C AC, ×15000;
(b) 960°C AC, ×9000;
(c) 850°C AC, ×6000

Fig. 6 Transmission electron microscopic photographs of the
film of the air cooled sample.

图 7 炉冷试样的薄膜透射电镜照片

(a) 1000°C FC, ×9000;   (b) 1000°C FC, ×38000;
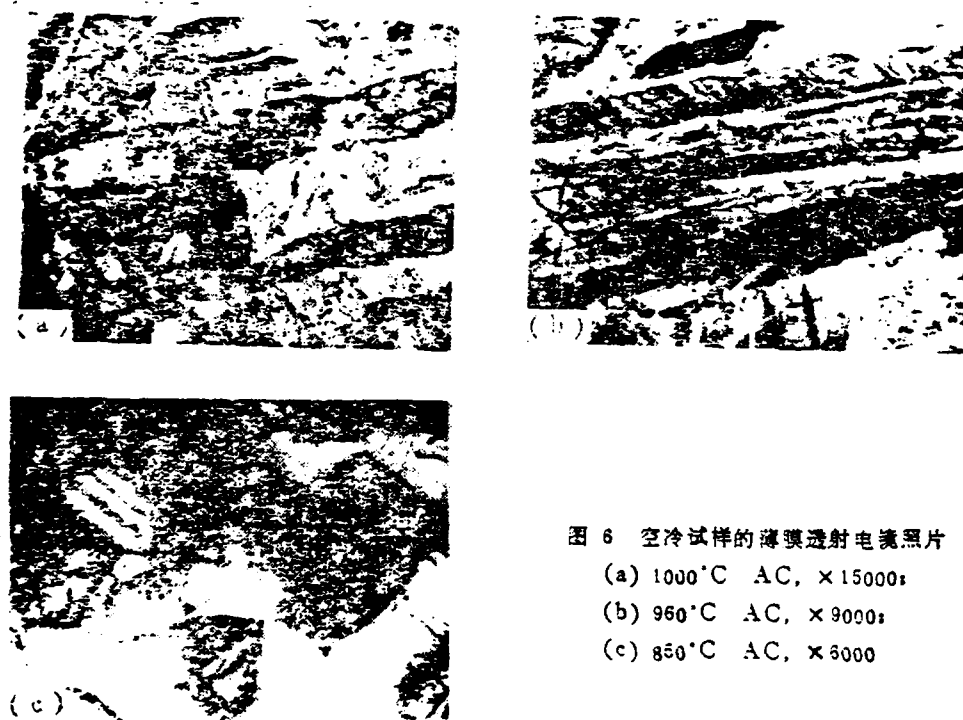(c) 960°C FC, ×6000;   (d) 850°C FC, ×6000

Fig. 7 Transmission electron microscopic photographs of the
film of the furnace cooled sample.

INFLUENCE OF TEMPERATURE ON THE ΔK_{th} AND da/dN OF LY-12CS
ALUMINUM ALLOY

Mu Zaiqin and Yin Huazi
(Institute of Metallurgy, Academia Sinica)

Tian Tiezhong (Design Department of the Shenyang Aircraft
Manufacturing Company)

Abstract

This paper used central crack tension samples (CCT samples)
in an air medium to test the fatigue threshold value ΔK_{th} of
LY-12CS aluminum alloy from room temperature to 250°C as well
as the crack growth rate da/dN above the threshold value under
200°C three load ratio (R=0,0.33, 0.67) conditions. Results
showed that:

(1) In the test temperature range, the threshold value
ΔK_{th} increased with the increases of the temperature.

(2) The rising temperature did not raise the crack growth
rate da/dN below 250°C but lowered the da/dN. Under the condi-
tions of three load ratios, ΔK ranged from 7-12kg/mm$^{3/2}$ and
the da/dN at room temperature was 1-3 times higher than that
at 200°C.

I. Preface

Under low stress intensity, fatigue crack growth properties
and the threshold strength factor ΔK_{th} value are essential
important parameters in engineering design. However, these
parameters of the material are often influenced by the structure,
test method, loading history, load ratio, frequency, environ-
mental medium and temperature etc. We studied the influences
of the load ratio and environmental medium (salt solution and
laboratory air) of LY-12CS aluminum alloy on the threshold and
above threshold da/dN [1].

63

Sometimes the LY-12 aluminum alloy used on aircraft was required to operate in about 200°C environments and it was therefore necessary to study the influence of temperature on the fatigue threshold value and growth rate. We provided related test data for the engineering design and service and protection. There are relatively few test reports on the influence of temperature changes on threshold value and da/dN. Many research results points out [2,3] that in the relatively low temperature range (20-350°C), the influence of temperature on the da/dN of A533B and 9Ni-4Co-0.30C structure steel is not noticeable yet in the even higher temperature range, the temperature more noticeably accelerates the crack growth rate. References [3-6] also report that for 304 type and 316 type stainless steel, Cr- Mo-V steel and A-212B, the fatigue crack growth rate increases with the increases of the temperature. What is the influence of temperature on the LY-12CS material's fatigue threshold value and da/dN? Do they have the above mentioned law? This paper focuses study on this problem.

II. Material and Test Procedure

2.1 Chemical Composition and Conventional Properties of the Material

The chemical composition and conventional properties of the material are shown in Table 1.

(1) 板材规格	(2) 化学成分, wt%				(4) 热处理制度		(9) 力 学 性 能			
及原始状态	Cu	Mg	Mn	Al	(5) 淬 火	(6) 人工 时 效	σ_b kg/mm²	$\sigma_{0.2}$ kg/mm²	δ %	ψ %
LY12-M-3.0 LY12-M-4.0	4.65	1.37	0.76	(3) 余量	500±5°C 10分钟	190°C 12小时	44.5	36.0	5.25	12.8

(7)　　(8.)

Table 1 (see next page)

64

Table 1   Chemical composition and conventional properties of
         material.
         Key: (1) Board specifications and original state;
         (2) Chemical composition; (3) Remainder; (4) Heat
         treatment technique; (5) Quenching; (6) Artificial
         ageing; (7) Minutes; (8) Hours; (9) Mechanical
         properties.

2.2   Samples

We used 3mm and 4mm thick central crack tension samples
(CCT samples). The length x width=240x100mm. Prior to the
test, we used a diamond abrasive to measure the partial polish-
ing of the crack length of the sample's center.

2.3   Test Conditions

The entire test was carried out on a Chinese made 10 ton
high frequency fatigue tester produced by the Hongshan Tester
Factory. The load was a constant amplitude sinusoidal wave-
form, the frequency was 140-150HZ, the two loading methods
were the pull-zero and pull-pull methods. The sample heating
used the following method: the middle section of one side of
the sample used three connected tubular infrared iodine tung-
sten lamp back-out heating (the power of each is 1 kilowatt),
used a pressure regulating transformer to regulate the tem-
perature and the 0.15mm thick microthermocouple used 204 cement
to stick on the side of the bake heated sample to measure tbe
temperature. The joining place of the two ends of the sample
and the tong hold used cyclic cooling and water cooling to
prevent the tester's tong hold from becoming hot.

Another side of the sample used an 80 power reading micro-
scope to directly measure the crack length. The precision
could reach 0.01mm, the recorded crack length 2a and corres-
ponding cycle number N. Its stress strength factor ΔK is
calculated by the following formula [7].

$$\Delta K = \frac{\Delta P}{B\sqrt{W}}\sqrt{\frac{\pi x}{2} \sec \frac{\pi x}{2}} \qquad (1)$$

In the formula, X=2a/W; B is the thickness of the sample; W is the width of the sample; and 2a is the crack length.

2.4 Test Procedure and Data Processing

The determination of fatigue threshold value ΔK_{th} and growth rate da/dN as well as the data processing method are the same as in Reference [1].

III. Test Results

3.1 Threshold Value ΔK_{th} Changes With the Temperature

The sample used to test the threshold value was the 4mm thick CCT sample. The fixed load ratio was 0.33 to avoid the property differences between the samples. On the same sample, we used the step reduced load method to separately test the threshold value ΔK_{th} at room temperature, 50, 100, 150, 200 and 250°C and its test sequence ranged from low to high temperature. The threshold value which changes with the temperature is shown in Fig. 1. Each test point in the figure is the mean value of two samples. We can see from Fig. 1 that in the room temperature to 250°C temperature range, following the increase of the temperature, the threshold value increases.
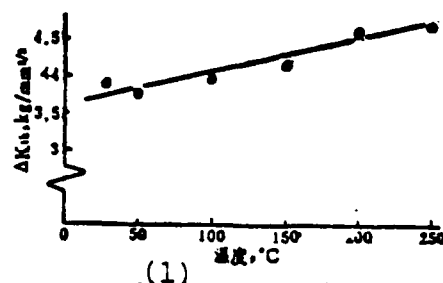

_(1)

Fig. 1 (see next page)

66

Fig. 1 (continued) The influence of temperature on the threshold value ΔK_{th}.

Key: (1) Temperature.

3.2 Fatigue Crack Growth Rate Under 200°C Conditions

We tested fatigue crack growth rate da/dN under low stress intensity above the threshold value with three load ratio (R=0, 0.33, 0.67) at 200°C. The sample used was the 3mm thick CCT sample and the fixed load range ΔP was 360kg. The relationship between da/dN and ΔK is separately drawn in Figs. 2, 3 and 4. For convenience of comparison, the solid lines used in the figures indicate the relational curve between da/dN and ΔK under room temperature conditions (used the least square method fitted test data). Under 200°C temperature conditions, the relationship between da/dN and ΔK_{th} can still be expressed by the Paris formula

$$da/dN = C(\Delta K)^n \qquad (2)$$

By using linear recurrent analysis we can calculate the C and n values (see appended table). We can see from Figs. 2-4 that the data points of three load ratios under 200°C are all on the lower side of the room temperature fitting line and fatigue crack growth rate da/dN is lower than room temperature. Under three load ratio conditions, ΔK range from 7-12 kg/mm$^{3/2}$ and fatigue crack growth rate da/dN at room temperature is 1-3 times higher than that at 200°C. This shows that increasing the temperature delays crack growth.
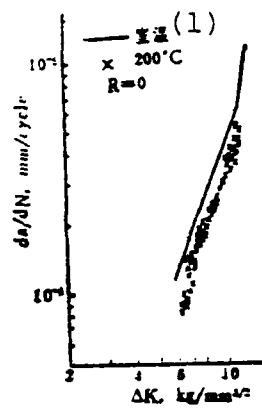
67

Fig. 2   Relationship of da/dN and △K (R=0).
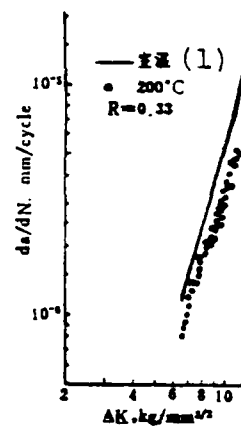   Key: (1) Room temperature.

Fig. 3   Relationship of da/dN and △K (R=0.33).
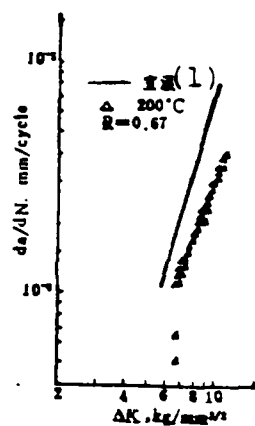   Key: (1) Room temperature.

Fig. 4   Relationship of da/dN and △K (R=0.67)
         Key: (1) Room temperature.

3.3 Influence of Temperature on Fatigue Crack Growth Rate

In order to further prove the effects of rising temperature on delaying crack growth, we designed this type of test: we selected four samples with basically the same initial crack lengths and fixed the same load range and load ratio (R=0.33). The first sample was done at room temperature, circulated 3×10^6 times and each cycle of 1×10^5 times recorded the crack length once. Based on the computer program given in Reference [7], we calculated the stress intensity factor ranges of $\triangle K$ and da/dN under each crack length. The relationship of da/dN and $\triangle K$ (i.e. with the crack length) is shown by the solid lines in Figs. 5, 6 and 7. The da/dN increases with the $\triangle K$ monotone. The second, third and fourth samples are separately tested at three temperature stages. The first stage was carried out at room temperature, circulated 1×10^6 times and afterwards separately heated to 100, 200 and 250°C. After waiting for the temperature to stabilize, we again circulated 1×10^6 times, finally again cooled to room temperature and then circulated 1×10^6 times. During the entire test process, we maintained the load range and load ratio the same as the first sample. Each cycle of 1×10^5 times recorded the crack length once and afterwards we separately calculated the relationship between stress intensity factor ranges $\triangle K$ and da/dN, and da/dN with $\triangle K$ under each crack growth as shown by the broken lines in Figs. 5, 6 and 7. We can see from Figs. 5, 6 and 7 that the first third stages of the second, third and fourth samples were room temperature tests. The da/dN all increased with $\triangle K$ (i.e. increase of the crack length) and the increase of the monotone tended to be the same as the changes of the first sample. Only during the second stage, that is, after the sample rose to 100°C, 200°C and 250°C did the da/dN change with the $\triangle K$ and manifest a concave valley (the bc section) and the da/dN was clearly lower than the first sample under the same type of crack growth room temperature conditions. After reaching the third stage, that is, returning to room temperature, the crack growth rate · gradually returned to the level of the first sample.

Fig. 5   Influence of rising temperature on da/dN (100°C).

Key: (1) Room temperature; (2) ab section, room temperature; (3) bc section, 100°C; (4) cd section, room temperature.
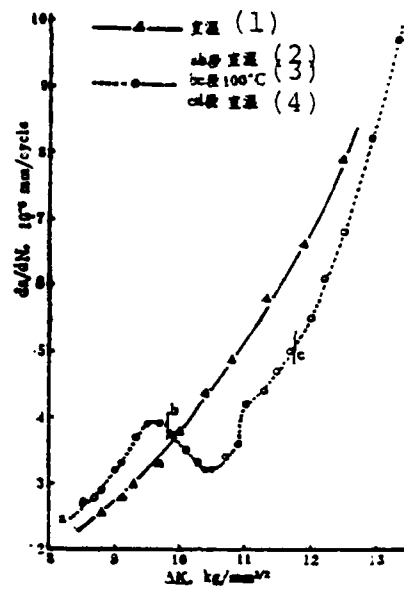

Fig. 6   Influence of rising temperature on da/dN (200°C).

Key: (1) Room temperature; (2) ab section, room temperature; (3) bc section, 200°C; (4) cd section, room temperature.
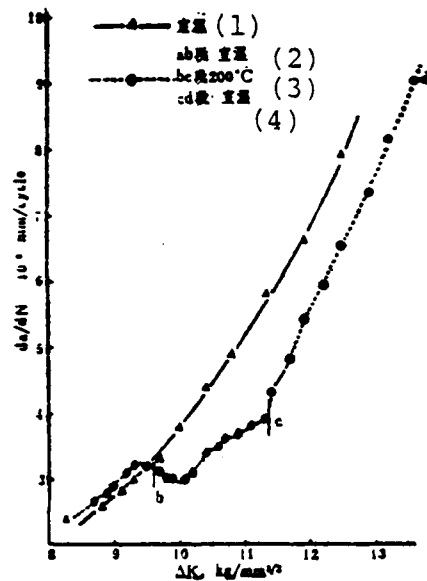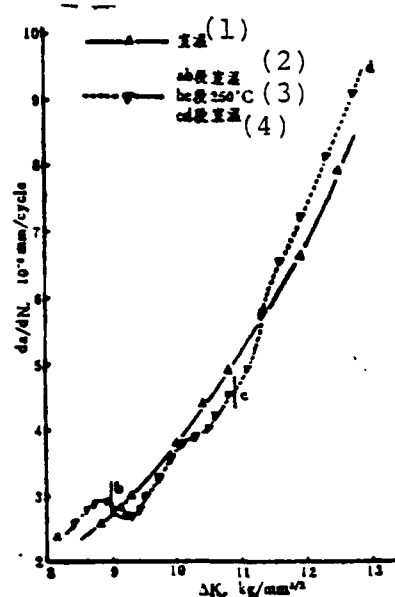
Fig. 7 Influence of rising temperature on da/dN (250°C).
Key: (1) Room temperature; (2) ab section, room temperature; (3) bc section, 250°C; (4) cd section, room temperature.

We can fully prove from the above mentioned test that when the temperature rises within the 100-250°C range, it noticeably lowers the fatigue crack growth rate. This is opposite of the test results of other materials.

When observing the fracture shape of the room temperature and 200°C fatigue test threshold area and the slow growth area with a scanning microscope, we find that whether it is the threshold area or slow growth area fracture shape between room temperature and 200°C, there are always noticeable differences. The room temperature threshold area has noticeable cleavage fractures and aside from the cleavage fractures the slow growth area also has relatively few fatigue stripes, but at the 200°C, in the threshold area and slow growth area fractures, we see noticeable plastic deformation which shows that it is necessary to consume a relatively large amount of energy during the fatigue crack growth process as compared to when at room

71

temperature. See Figs. 8-9 (see Plate 9).

IV. Discussion of Results

4.1 Threshold Value ΔK_{th} Changes With the Temperature

Rising temperature causes ΔK_{th} to rise. We consider
that this is possible mainly because the rising temperature
causes the strength of the material to lower. A large number
of tests show that the fatigue limit increases with the in-
creases of the strength of the material. The fatigue limit
reflects the resistance of the material to crack sprouting and
the fatigue threshold reflects the resistance of the material
to fatigue crack growth. The physical qualities of the two
are possibly different. Therefore, following the changes of
the strength, σ_e and ΔK_{th} have opposite laws of change and
many tests prove this law.

During the fatigue process, the external load increases to
maximum load P_{max} and the crack tip cannot avoid forming a
plastic region parallel to the direction of the crack. For
the small range yielding, the plastic region

$$\omega = \frac{\pi}{8} \left(\frac{K_{max}}{\sigma_s} \right)^2 \tag{3}$$

Because of the effects of the external load, the crack tip
must open up and thus become dull, acting as the approximate
processing. The tip dulls and becomes semicircular. The
semicircular dull tip curvature radius ρ_{max} takes one half
of the crack tip's open displacement, that is

$$\rho_{max} = \frac{K^2_{max}}{2E'\sigma_s} \tag{4}$$

72

In the formula

$$E' = \begin{cases} E & \text{plane stress} \\ \dfrac{E}{1-v} & \text{plane stress} \end{cases}$$

E is the modulus of elasticity and v is Poisson's ratio.

We can see that following the decrease of the intensity, the level of the crack point's dulling rises weakening the stress concentration and thus strengthening the resistance to crack growth and raising threshold value ΔK_{th}.

As regards the relationship of the threshold value and the intensity, Ritchie [8] reported that the ΔK_{th} of 300M steel increases with the decreases of the intensity. Vosikovsky [9] counted 33 types of ferrite-pearlite steel ΔK_{th} and strength relationships and obtained the linear relationship of ΔK_{th} and σ_y, σ_b

$$\Delta K_{th} = 11.17 - 0.0032\sigma_b \tag{5}$$
$$\Delta K_{th} = 11.40 - 0.0046\sigma_y \tag{6}$$

(ΔK_{th} uses $MPa\sqrt{in}$ as the unit, σ_b, σ_y uses MPa as the unit.) Our test results change with the temperature and the relationship between ΔK_{th} and σ_s also coincides with the above law. Figs. 10 and 11 separately show that the σ_s of the LY-12CS material changes with the temperature as well as the relationship between ΔK_{th} and σ_s. From Fig. 11, we can obtain

$$\Delta K_{th} = 7.53 - 0.11\sigma_s \tag{7}$$

When compared with formula (5), the first term in formula (7) is smaller than in formula (5) but the second coefficient is larger than in formula (5).
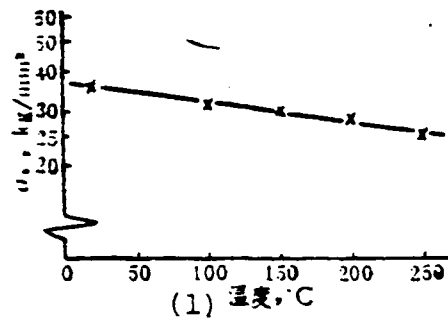
Fig. 10 Relationship of yielding strength and temperature.
Key: (1) Temperature
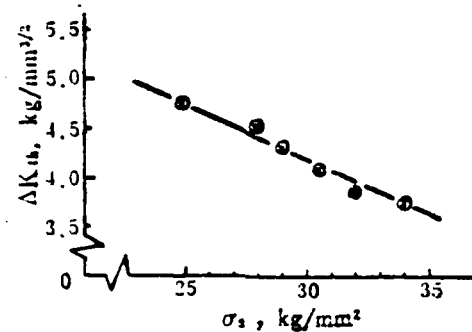
Fig. 11 Relationship of threshold value ΔK_{th} and the yielding
strength.

4.2 Slowing Effects of Rising Temperature on Crack Growth

Below 10^{-5}mm/c, our test crack growth rate belongs to the
low speed growth area. The crack growth in this area is non-
continuous growth and generally grows along certain crystal-
lization. It is not a cyclic crack which grows forward but
uses repeated slip disconnected growth. The slips are not
uniformly distributed but often concentrated in sustained slip-
ping zones. These slipping zones have relatively high strain
amplitude which causes the slipping to only be limited to be
carried out in these sustained slipping zones because the
repeated slipping in the sustained slipping zones possibly pro-
duce very high dislocation density and stores very high strain

74

energy. This will be of aid in the production of new free surfaces which will create cleavage fractures along the sustained slipping surface.

Following the temperature rise, σ_b decreases, atom activity strengthens and the sustained slipping zone of the crack tip possibly increases. Following the rise in temperature although the crack tip's total energy possibly increases, yet the slipping is possibly more uniform than the previous ones and the distribution of the dislocations tends to be uniform. This causes the stress concentration level to weaken and the crack growth necessarily consumes even more energy. Further, because the crack growth rate is controlled by ΔK_{th}, following the rise of the temperature, ΔK_{th} rises, the crack growth resistance increases and therefore da/dN slows down.

V. Conclusion

As regards the LY-12CS aluminum alloy in the room temerature to 250°C range:

1. Following the rise of the temperature, the threshold value ΔK_{th} also gradually rises;

2. In the low speed growth area (da/dN $<$ 10^{-5}mm/cycle), the rising temperature decreased the crack growth rate and under the 200°C three load ratio test conditions, ΔK ranges from 7-12 kg/mm$^{3/2}$ and the fatigue crack growth rate is 1-3 times higher than that at 200°C;

3. In the low speed growth area, from toom temperature to 250°C, the rising temperature will delay the growth of fatigue cracks;

4. The reason why the rising temperature increased the fatigue threshold value and decreased the crack growth rate is

possibly because after the temperature rose the strength of the material lowered.

During the testing and research process of this work, we obtained the guidance and help of Wang Zhongguang, researcher, and Jie Sishi, engineer. Comrade Ai Suhua provided the computer program for the computer processing of the data. We would like to specially thank them here.

温 度 (1)	载荷比 (2)	拟 合 线 (3)	$K=7\sim12kg/mm^{3/2}$		
			C	n	注 (7)
200°C	0	(4) 95.4%频率分散带上限	1.45×10^{-8}	2.45	三个试样的结(8)果
		(5) 拟 合 线	1.15×10^{-8}	2.45	
		(6) 95.4%概率分散带下限	9.14×10^{-9}	2.45	
200°C	0.33	(9) 95.4%概率分散带上限	5.11×10^{-9}	2.85	两个试样的结(15)果
		(10) 拟 合 线	4.61×10^{-9}	2.85	
		(11) 95.4%概率分散带下限	4.71×10^{-9}	2.85	
200°C	0.67	(12) 95.4%概率分散带上限	9.44×10^{-9}	2.56	两个试样的结(16)果
		(13) 拟 合 线	8.77×10^{-9}	2.56	
		(14) 95.4%概率分散带下限	8.15×10^{-9}	2.56	

Appended Table The C.m. value of the da/dN=C(ΔK)^n fitting based on the Paris formula.

Key: (1) Temperature: (2) Load ratio; (3) Fitting line;
(4) Upper limit of 95.4% probability dispersion zone;
(5) Fitting line; (6) Lower limit of 95.4% probability
dispersion zone; (7) Notes: (8) Results of three samples;
(9) Upper limit of 95.4% probability dispersion zone;
(10) Fitting line; (11) Lower limit of 95.4% probability
dispersion zone; (12) Upper limit of 95.4% probability
dispersion zone; (13) Fitting line; (14) Lower limit of
95.4% probability dispersion zone; (15) Results of two
samples, (16) Results of two samples.

References

[1] Mu Zaiqin, Yin Huazi et al, Aeronautical Materials (Special Issue), 1(1981), no. 2,35.

[2] McHenry, H.I., J. of Materials, 6(1971), No. 4, 862.

[3] Clark, W.G., J. of Materials, 6(1971), No. 1, 134.

[4] James, L.A., Schwenk, E.B., Metallurgical Trans., 2(1971), No.2, 491.

[5] Haigh, J.R., Eng.Frac.Mech., 7(1975), No.2, 271.

[6] Mukherjee, B., Third Int Conference on Fracture, Vol.VI V-423.

[7] ASTM E647-78T, 1980 Annual Book of ASTM Standards, Part 10, p.749.

[8] Ritchie, R.O., Metal Sci. 11(1977), Nos. 8 and 9, 368.

[9] Vosikovsky, O., Eng. Frac. Mech., 11(1979), No. 3,595.
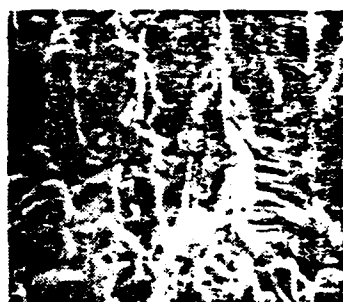
(1) 室温 (R=0)　　　　　　　　200°C (R=0)

(2) 室温 (R=0.33)　　　　　　200°C (R=0.33)

Fig. 8　Fracture shapes of the room temperature and 200°C
threshold areas, x 500.

Key: (1)-(2) Room temperature.
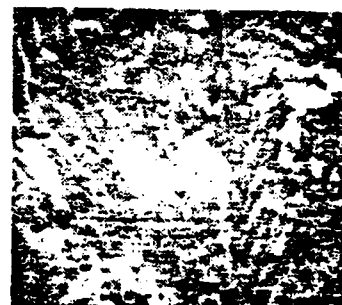
78

(1) 室温 (R=0.33)   200°C (R=0.33)

(2) 室温 (R=0.67)   200°C (R=0.67)

Fig. 9   Fracture shapes of the room temperature and 200°C
         fatigue cracking slow growth areas.

         Key: (1)-(2) Room temperature.

PRELIMINARY INVESTIGATION OF FATIGUE CRACK PROPAGATION OF
30CrMnSiA STEEL IN SALT SPRAY CORROSION CONDITIONS

Ma Yushan, Yu Xiuling, Gou Baocheng and You Dexuan

Abstract

This paper uses the method of fracture mechanics to make a
preliminary study of the fatigue crack propagation character-
istics of 30CrMnSiA structure steel in a salt spray medium and
in room temperature air.

Using compact tension samples, in the stress intensity
range of $\Delta K = 70\text{-}200 \text{kg/mm}^{3/2}$, the test results showed in the
early stages of the tests, the crack propagation rate in a salt
spray medium was higher than in room temperature air and it
sharply increased with the decrease of the test frequency. This
type of situation is commonly caused by a hydrogen embrittlement
mechanism. After the tests had been carried out for 20-40 hours
in the salt spray medium, due to the accumulation of corrosion
products on the crack surface, the crack propagation rate
gradually slows even below the da/dN curve in room temperature
air. During the final stage of the test, because of the in-
crease of the stress intensity range, the crack propagation
rates in the two mediums were getting closer to eachother.

Preface

In the last ten odd years, because the important components
of some aircraft and naval vessels, and the key locations of
oil, power stations and atomic power plants encounter corrosion
fatigue which results in serious destruction, this caused re-
lated domestic and foreign acientific research, production and
service departments to give serious attention to the problems
of corrosion fatigue.

In order to satisfy the pressing requirements of research on aeronautical materials, aircraft design and use, we began from the mechanical states and operating environments of the important components of some aircraft and considered the unavoidable existence of defects or cracks in component materials. We first carried out a preliminary investigation of the fatigue crack propagation characteristics of 30CrMnSiA structure steel under salt spray conditions. We referred to the B117-73 salt spray test standard method and E647-81 determination of the crack propagation rate test method provided by ASTM of the United States and used our existing technical and equipment conditions to carry out comparitive tests of the above mentioned materials under salt spray and air and tests on the different frequency influences in salt spray.

Test Conditions

1. Raw Materials

See Table 1 for the state and room temperature static test results.

(1) 产地 (2)	炉号	棒材 尺寸 (3)	(4) 化 学 成 分 , %								σ_b σ_s kg/mm²	ψ δ %	a_k kg·m/cm²	H_s kg/mm²
			C	Si	Mn	Ni	Cr	Cu	S	P				
(5) 齐钢	119003	Φ130	0.3	1.05	1.00	0.27	0.87	0.07	0.011	0.014	119 110	55 14	8	341
(6) *热处理状态 890±10°C, 空冷,510°C回火														

Table 1   Raw material states and mechanical properties
  Key: (1) Place of production; (2) Furnace number;
  (3) Bar dimensions; (4) Chemical composition;
  (5) Qigang; (6) *Heat treatment State, 890±10°C,
  air cooling, 510°C tempering.

2. Test Preparations

The sample was the CT type, thickness B=25mm, width W=100mm and the sample was selected based on LT. The initiation trough

of the prefabricated crack used 0.12mm molybdenum wire to carry out line cutting and the vertical surface of the open initiation trough also required the machining of thread holes commonly used for displacement.

3.   Test Equipment

(1) The entire test was carried out on a 50 ton electrolytic solution servofatigue tester produced by the MTS Company of the United States. This includes the salt spray test system and PDP11/34 computer system provided by this company.

After examination and determination, the static load error of the tester $\not> 1\%$, the dynamic load error $\not> 2\%$ and the maximum error of the crack open displacement measuring system is 0.25%. The sample's clamping apparatus used GH78 alloy and the loading system has sufficient rigidity.

(2)   The crack length under salt spray used the model 632-10C-01 displacement gauge to measure the COD value and the crack length could also use a 10 to 13 power toolroom microscope for direct measurements in air.

(3)   See Fig. 1 (see Plate 10) for the salt spray system.

The spray room is a sealed room. The inside walls are covered with white nylon, the ceiling is slanted to prevent non-test mediums and spray from falling on the sample (see Fig. 2, Plate 10).

The strain foil on the displacement gauge and its lead wire are separately installed in a stainless steel sealed shell and slender tube (see Fig. 3, Plate 10).

The temperature and salt spray quantity in the spray room can be regulated, the pressure is 3-8psi air passing through

warm water preheating and filtering. The salt solution is automatically supplied by a water pump.

(4) In the salt solution, the NaCl and tap water or distilled water are made up according to the weight ratio of 5:95. It is required that the total number of solids in the tap water not be greater than 200ppm. When the salt solution is in $35 \pm 2°C$, the pH value is in the 6.5-7.2 range. If it exceeds this range, it is necessary to adjust with HCl or NaO. The pH value can be determined by the pH determinating instrument or determined by precision test paper of a suitable range.

4. Test Parameters

Stress ratio: R=0.1; test frequency: 0.2-5Hz under 5-20Hz salt spray room temperature: $35 \pm 2°C$; salt spray deposit quantity: $1-2ml/hour/80cm^2$; laboratory temperature: $25 \pm 3°C$, humidity $60 \pm 10\%$.

Test Process and Results

1. Sample Standardization

Because the salt spray test conditions are limited, this test used the flexibility method to measure the amount of crack propagation. For this reason, it is necessary to standardize the corresponding relationship between the sample's flexibility and the crack length beforehand. During the test process, with each passage of a certain number of cycles, we measure its flexibility value (this is actually the open displacement quantity of the displacement gauge's spring arm area) and from the standardized curve we obtain the corresponding crack length. Thus, we also obtain the relationship between the crack length and the number of cycles.

This test used a sample to standardize in stages the 30CrMn SiA, that is, after line cutting a certain length standardize

83

once; then cut a certain length and standardize again. There
are seven stages to the standardization, that is, 25, 35, 40,
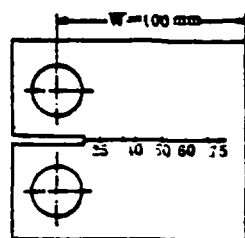50, 60, 70 and 75mm. The dimension intervals are as shown in
Fig. 4.

Fig. 4   Schematic of standardized sample.   -

The load and corresponding crack open displacement quantity
are monitored by the tester's digital measuring system.   In
order to avoid the occurrence of relatively large plastic de-
formation at the front edge of the cracks which create stress
relaxation, we must guarantee an excellent linear relationship
between the load and open displacement.   Therefore, the sel-
ection of the largest load must be suitable.   Table 2 gives the
numberical relationship of the P-V-a correspondence.

The a-V standardized results are transformed into the form
of dimensionless flexibility (EBV)/P-a/W (W is the width of the
sample, P is the pressure load, B is the thickness of the
sample and E is the elastic modulus) and we can obtain the
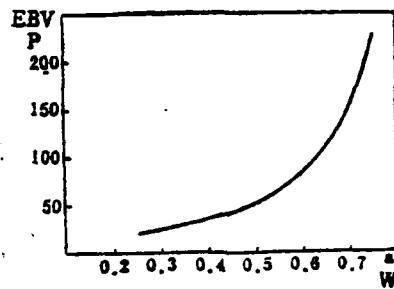standardized curve as shown in Fig. 5.

Fig. 5   Standardized curve of $\dfrac{EBV}{P} \sim \dfrac{a}{W}$.

a, mm \ V, 伏(1) \ P, kg	500	1000	1500	2000	2500	3000
25	0.052	0.104	0.154	0.203	0.251	0.298
35	0.077	0.153	0.225	0.295	0.365	0.433
40	0.093	0.180	0.263	0.347	0.430	0.511
50	0.139	0.272	0.401	0.528	0.654	0.779
60	0.224	0.435	0.644	0.849	1.055	1.261
70	0.404	0.710	1.169	1.547	1.927	2.29
75	0.602	1.170	1.730	2.29	2.86	3.46

Table 2   Open displacement quantity (V) when there are different
loads (P) and crack lengths (a).

Key: (1) Volt.

The above mentioned curve can be expressed by the following
mathematical expression:

85

$$a/W = -0.11337 + 0.0257052\left(\frac{EBV}{P}\right)$$

$$-4.5856 \times 10^{-4}\left(\frac{EBV}{P}\right)^2$$

$$+5.05926 \times 10^{-6}\left(\frac{EBV}{P}\right)^3$$

$$-3.07087 \times 10^{-8}\left(\frac{EBV}{P}\right)^4$$

$$+5.76707 \times 10^{-11}\left(\frac{EBV}{P}\right)^5$$

$$+3.9845 \times 10^{-13}\left(\frac{EBV}{P}\right)^6$$

$$-2.46167 \times 10^{-15}\left(\frac{EBV}{P}\right)^7$$

$$+4.00389 \times 10^{-18}\left(\frac{EBV}{P}\right)^8$$

2. Test Process and Results

(1) Crack preparation: to prepare the cracks, we use the gradual load decrease method. In order to avoid overloading effects, the latter load is equivalent to 80% of the former load and at each load level we guarantee sufficient crack propagation quantity. At the least, it must be larger than $\frac{3}{\pi} \frac{K'_{max}}{\sigma_s}$ so as to eliminate the influence of the upper load's overloading on the crack propagation (σ_s is the yielding strength, K'_{max} is the final value of the maximum stress intensity of the upper load level). The last stage of the load is the same as the formal test load. In order to avoid the influence of the linear cutting procedure possibly creating residual stress on the front edge of the fracture, the prepared crack length should be larger than 2mm.

(2) Measurement of crack length: under room temperature air conditions, the measuring precision of the crack length can reach 0.01mm and we take the mean value of the sum of the crack lengths on the two sides of the sample as the calculated crack length.

86

In the salt spray environment, measurement of the crack length is finding the open displacement V value obtained at any time on the (EBV/P) ~ a/W standardized curve. See Figs. 6 and 7 for the rela tionship between the crack length and the number of cycles.

Fig. 6   a-N curve of 300CrMnSiA steel.
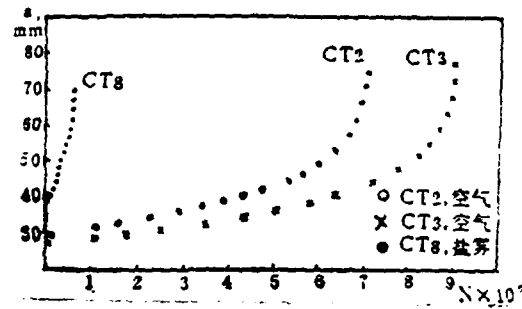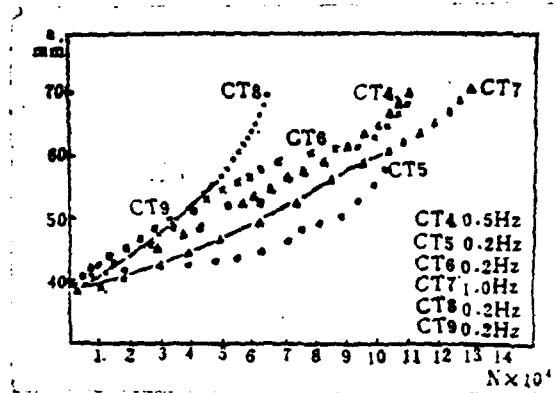   Key: (1) Air; (2) Air; (3) Salt spray.

Fig. 7   a-N curve of CT4-CT9 samples (in salt spray).

(3) The calculation of $\triangle K$ and da/d N is:

$$\Delta K = \frac{\Delta P}{B\sqrt{W}} \frac{(\alpha+2)}{(1-\alpha)^{3/2}} (0.886+4.64\alpha-13.32\alpha^2 +14.72\alpha^3-5.6\alpha^4)$$

In the formula: $\alpha = a/W$ is effective for the $a/W \geqslant 0.2$ expression.

87

da/dN is found by the seven point progressive increase multinomial fitting method.

The calculation of ΔK and da/dN is carried out on a PDP11/34 computer with a prewritten crack propagation rate data processing program and the da/dN $\sim$ ΔK curve is drawn on the double logarithm coordinate paper (see Fig. 8).
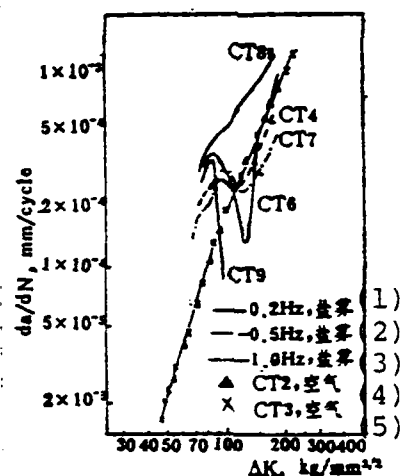
Fig. 8   Relationship of da/dN and ΔK of 30CrMnSiA steel. Key: (1)-(3) Salt spray; (4)-(5) Air;

Analysis and Discussion of Results

1. Analysis of Test Results in Air

The repeatability of the test results of the CT2 and CT3 samples is relatively good and in the second stage of the fatigue crack propagation, da/dN and ΔK assume a linear relationship. This coincides with the data provided in Reference [1]. In Fig. 8, we can clearly see the existence of a turning point at about 10^{-4}mm/cycle. Reference [2] considers that the precise determination of this turning point as well as the linear slope on the two sides of the turning point are of great significance to the precise calculation of the fatigue destruction life.

It is also necessary to explain that when the test was in air the frequency which we used was relatively high yet the obtained results are comparable with the results of salt spray tests under low frequency. The influence of frequency on the propagation rate of the fatigue cracks in a laboratory environment was very small. Ouyang Hui et al [3] studied the influence of frequency on the da/dN of 30CrMnSiNi2A steel. The employed frequencies were 20cpm (0.33Hz), 800cpm (11.6Hz) and 2400cpm (40Hz) and when R=0.1, the difference of the obtained da/dN were not large, all being within the same dispersion zone. In the same way, Atkinson [4] pointed out that when the frequency changes in the 0.1-100Hz range, the da/dN value has no noticeable changes in air.

2. Analysis of Test Results in Salt Spray

As seen in Fig. 8, the five samples in air had relatively complex situations:

(1) Generally speaking, because of the joint effects of the corrosive environment and alternate load, the propagation of the fatigue cracks will be accelerated. For example, in salt spray, when the CT8 sample is at $\Delta K-72kg/mm^{3/2}$, its da/dN is 5 times that in air. The other 5 samples are the same during the first several tens of hours. Aside from this, we can also see that when we lower the frequency, the influence of the salt spray increases. In the $\Delta K=72-85kg/mm^{3/2}$ range, the da/dN value obtained under 0.2Hz frequency is higher than the results obtained under 0.5Hz and 1Hz. The above situation is often caused by a hydrogen embrittlement mechanism.

(2) Four of the five samples have decreases of the da/dN and after a certain length of time, the da/dN again continues to rise. The number and time of the cycle of decrease and renewed rising as well as the crack lengths and ΔK values are listed in Table 3.

(1) 试样号	(2) 试验频率 Hz	(3) 起始裂纹长度 mm	(4) da/dN开始降低				(8) da/dN重新升高			
			(5) 循环次数周	(6) 时间小时	(7) 裂纹长度 mm	ΔK kg/mm$^{3/2}$	(9) 循环次数周	(10) 时间小时	(11) 裂纹长度 mm	ΔK kg/mm$^{3/2}$
CT4	0.5	39.4	55900	30.5	52.3	97.1	72150	39	56.7	112.9
CT6	0.2	38.3	33000	44	48.5	86.2	78160	104.5	60.1	127.9
CT7	1	38.2	77520	21.5	54.2	103.7	99950	28	60.3	129.2
CT9*	0.2	38.1	27220	36	48.2	85.2	—	—	—	—

(12) * CT9试样另有用途，未做完。

Table 3 (See next page)

Table 3 The da/dN changes of the samples in salt spray.

Key: (1) Sample number; (2) Test frequency, Hz; (3) Initial crack length, mm; (4) da/dN initial decrease; (5) Number of cycles; (6) Time, hours; (7) Crack length, mm; (8) da/dN renewed rising; (9) Number of cycles; (10) Time, hours; (11) Crack length, mm; (12)*The CT9 sample has another use, incomplete.

The reason why these four samples show da/dN decreases is still not very clear. This phenomenon has been mentioned in some materials [5-9]. The following analysis will perhaps be of aid by considering this problem from a different angle.

Борисова [8] et al observed the crack branching in titanium alloys which caused the propagation rate to decrease. They used the CT9 sample to carry out tests. When the da/dN decreased to 8×10^{-5} mm/cycle and a=53.8mm, the engine was stopped and the sample was taken down and blow dried. Then they polished the crack tip areas on the two surfaces of the sample and afterwards placed it under an ММ microscope and observed (800 power amplification). The result was that they still hadn't found crack branching. However, it is also possible that they were unable to observe crack branching on the sample surface.

Holder [7] considers that after the crack grows to a certain length, the medium's transmission difficulties cause a decrease of the fatigue crack propagation rate. The four samples which produced da/dN decreases had roughly the same initial crack lengths. Although the CT6 and CT9 had initial decreases at the same crack length, yet not all of the samples accorded with this law.

Table 3 shows that the da/dN of the four samples of CT4 etc. decreased after 20-40 hours of tests. This is very possibly related to the gradual formation of corrosion products near the crack tip and on the sample surface within this period of time.

91

We can see from Figs. 9 and 10 (see Plate 10) the existence and distribution of the corrosion products. The JEM-200A electron microscope is used to observe the fractures of the CT3, CT6 and CT8. On the fractures of the CT3 sample tested in air, a fatigue strip could be seen (Fig. 11, see Plate 11). The fatigue strip was not observed after the CT6 and CT8 sample fracture surfaces tested in salt spray removed the corrosion products. Moreover, there still remained corrosion spot marks (Figs. 12, 13 and 14, see Plate 11).

The lower part of the sample was placed in the salt solution and after being put there for 10 hours at 35°C, the sample surface outside of the solution had much more serious corrosion than the sample solution in the salt solution. This is due to the oxygen content of the salt spray being higher than the static position of the salt water. Therefore, the rate of the ferric oxide growth in the salt spray is faster than that in the salt water.

After this test was carried out for a certain amount of time, the corrosion products on the fracture surface near the crack tip became thicker causing the solution transmission as well as the reaction with the newly formed metallic surface to be obstructed. The anode solution of this type of crack tip and the hydrogen embrittlement effect gradually weaken and because of this the crack propagation rate began to decrease. Because of the further accumulation of corrosion products, the crack propagation rate is lower than the da/dN value in air under the same nominal stress intensity.

It should be pointed out that after the CT8 sample in Fig. 8 goes through 54 hours of testing, although the crack propagation rate has a tendency to slow down, yet is is not noticeable.
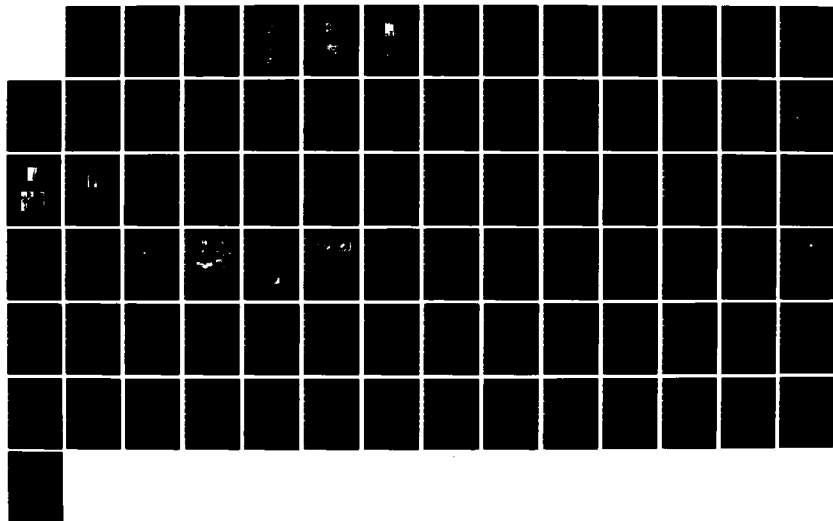
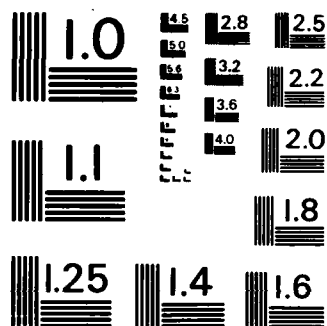| | | 1.0 | | 4.5 | 2.8 | 2.5 |
5.0		3.2	2.2
6.6		3.6
		1.1		4.0	2.0
					1.8
		1.25		1.4	1.6

MICROCOPY RESOLUTION TEST CHART

NATIONAL BUREAU OF STANDARDS-1963-A

(3) When the $\triangle K$ value further increases, because the mechanical factors occupy a dominant position, the crack propagation rate further increases until the sample breaks.

Preliminary Conclusion

The changes of the crack propagation rate of 30CrMnSiA steel under salt spray conditions is determined by the formation process of the corrosion products near the crack tip. When there are not many corrosion products in this area, its da/dN is higher than in air and moreover it increases with the decreases of the test frequency. After the accumulation of corrosion products enlarges to a certain level; the da/dN will decrease.

The fatigue crack propagation characteristics of materials in salt spray conditions are influenced by mechanical, chemical and electrochemical etc. factors. Systematic research is also required to obtain deeper knowledge of the law.

[1] Compilation of Data on the Fatigue Crack Propagation Rate of Aeronautical Metallic Materials, Beijing Institute of Aeronautical Materials, 1981, 10,p39.

[2] Chen Hu et al, Engineering Fracture Mechanics (Vol.2), 1977, 9,p425.

[3] Ouyang Hui et al, The Influence of Frequency on the Crack Propagation Rate of 30CrMnSiNi2A Steel, Internal Materials, Beijing Institute of Aeronautical Materials, 1981,11.

[4] Atkinson, J.D. and Lindley, T.C., The Effects of Frequency and Temperature on Environmentally Assisted Fatigue Crack Growth Below KIscc in Steels, I.Mech.E.Conf.,1977,p65.

[5] Austen,I.M. and Walker,E.F., Quantitative Understanding of the Effects of Mechanical and Environmental Variables on Corrosion Fatigue Crack Behaviour, I.Mech.E.Conf.,1977,p1.

[6] Metal Corrosion and Protection Investigation Group of the Chinese Academy of Sciences, "Some Situations of British

Research on Metal Corrosion and Protection", Science and Technology References Press,1978,12,p6.

[7] Holder,R., Environmental Effects on fatigue Crack Initiation and Propagations in a Cast Steel, I.Mech.E.Conf., 1977,

[8] Борисова,Е.А.,Шашенкова,И.Н.,Захарова,М.В.,Свойства сплава ВТ6 после β-отжига. Мет.и Тер.Обр.Мет., 1981. 4. p43.

[9] Tu.,L.K.L. and Seth, B.B., Threshold Corrosion Fatigue Crack Growth in Steels, J.Testing and Evaluation, 1978,1,p66.
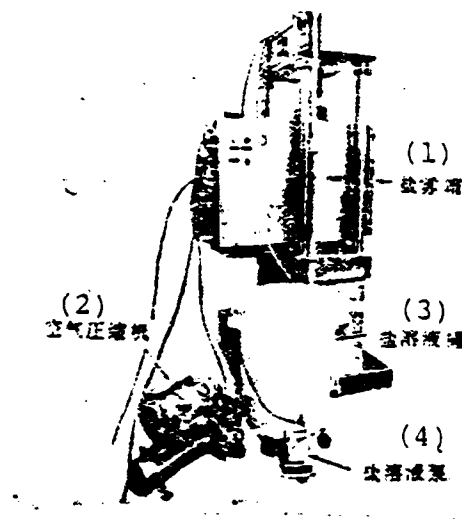
Fig. 1 Salt spray test system.

Key: (1) Salt spray box; (2) Air compressor; (3) Salt
solution container; (4) Salt solution pump.
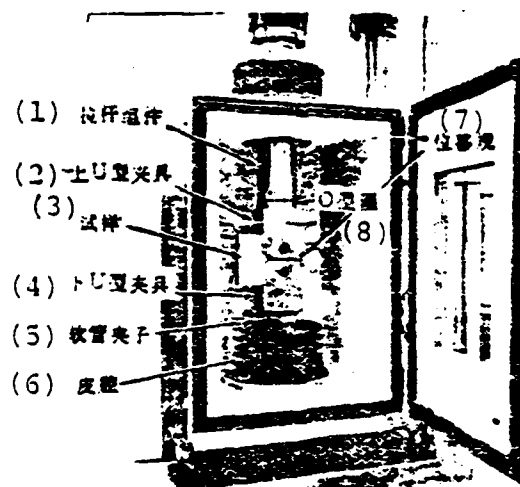
Fig. 2 Installment of sample in salt spray box.
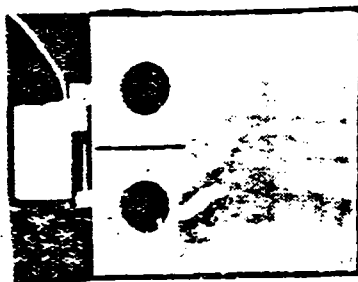
Fig. 3   Installment of displacement gauge.
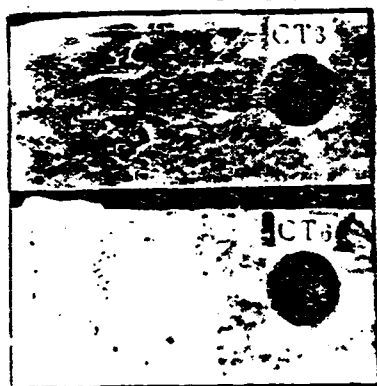
Fig. 9   External appearance of CT3 (in air) and CT6 (salt spray)
         steel samples.

Fig. 10   Fractures of CT3 (in air) and CT6 and CT8 (salt spray) samples.

Fig. 11   Metallography of CT3 sample fractures, x 13,200.

97

Fig. 12 Metallography of CT6 sample fractures, x 12,200.
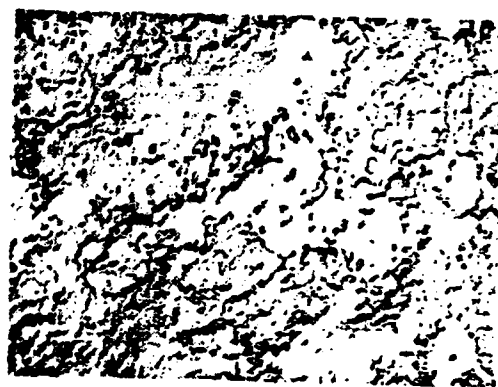
Fig. 13 Metallography of CT8 sample fractures, x 12,200.

Fig. 14   Metallography of CT8 sample fractures (different place),
x 12,200.

STUDY OF THE FATIGUE CRACK PROPAGATION CHARACTERISTICS OF
YB-3 AND YB-4 AERONAUTICAL ORGANIC GLASS

Chen Ruoxi, Shao Yujun and Fan Tang

Abstract

We studied the effects of the absorbed water and humid
heat ageing of the stress ratio and materials of an alternating
load as well as the water environment on the fatigue crack
propagation resistance characteristics of YB-3 and YB-4 aero-
nautical organic glass. We discovered that the moisture
content, especially the water environment, had excellent
effects on the crack resistance properties of two types of
glass. Thus, it has important significance. Based on sectional
microscopic observations, we proposed a micromechanism model for
the crack subcritical propagation of organic glass under alter-
nating loads.

I. Preface

Under the effects of alternating loads, because the crack
has subcritical propagation, even though the maximum stress
σ_{max} is much lower than damaging stress σ_f, the cracks in
the material can still propagate forward. At this time, the
material's crack propagation resistance ability is expressed by
fatigue crack propagation rate da/dN. When organic glass is
used as the structural material, fatigue crack propagation is
the major damaging form [1] which can be described by the Paris
formula [1,2]. There are many factors which influence the fat-
igue crack propagation rate of organic glass and there have
been foreign reports in recent years [1,8]. This paper focuses
study on the effects of the frequency and stress ratio of an
alternating load as well as the moisture content, water envir-
onment and humid heat ageing on the fatigue crack propagation

characteristics of Chinese-made YB-3 and YB-4 organic glass.
We also used a self-written program to aid the TQ-16 computer
to process the test data. Because the propagation mechanism
of the fatigue crack subcritical area of the organic glass is
completely different from the crack slow propagation area of
fracture toughness, this paper observed the section's appear-
ance and investigated the micromechanism of the crack propaga-
tion under the effects of alternating loads.

II. Test Section

The test material was YB-3 and YB-4 organic glass. We used
center cracked samples, the dimensions were 360x100x10mm and
the exterior was the same as in [9]. The test was carried out
on an Instron 1253 tester. After the center crack used special
mould processing, we then prefabricated fatigue cracks. Prior
to the test, we proprocessed the sample: (A) was placed in a
standard laboratory environment ($23\pm1°C$, relative humidity
$50\pm2\%$) for 4 days; (b) was humid heat aged in $60\pm1°C$ saturated
water vapor for 30 days.

The waveform of the alternating load used the sinusoidal
wave, the frequencies were 5Hz and 20Hz, stress ratio R was
1/3, 1/5 and 1/10. After a certain number of alternating load
cycles, we used a reading microscope to measure the front and
rear surfaces of the sample and the crack lengths a, a_5 and a_3
between them corresponding to cycle number N. Because the
transparency of organic glass is excellent we can accurately
measure a_3 with the method of regulating the focal distance.
The measuring interval of the crack length is about 0.3-0.5mm.
After the sample is broken open, we measure the crack length
of the subcritical area with a toolroom microscope.

The expression of da/dN uses the Paris formula:

$$\frac{da}{dN} = C(\Delta K)^n \qquad (1)$$

$$\Delta K = \frac{P_{max}(1-R)}{BW} \sqrt{\frac{\pi a}{2}} \left[1 - 0.025 \left(\frac{a}{W}\right)^2 + 0.06\left(\frac{a}{W}\right)^4 \right] \sqrt{Sec \frac{\pi a}{2W}} \qquad (2)$$

C and n are material constants; ΔK is the stress intensity factor range, $kg/cm^{3/2}$; B and W are the thickness and width of the sample, cm; P_{max} and P_{min} are the maximum load and minimum load of the alternating load, kg; R is the stess ratio of the alternating load $R = \frac{P_{min}}{P_{max}}$; a is the equivalent crack length corresponding to a certain number of alternating load cycles, cm. We calculated according to the following formula [9]:

$$a = \frac{2}{3}a_2 + 1/3(a_1 + a_3) \qquad (3)$$

Because the test data has very large dispersion and the amount of mathematical processing is very large, we must use a computer. See [10] for detailed explantion of computer program (ALGOL language) and mathematical method.

III.   Test Results

3.1 Data Processing and Computation Results

After putting in the complete test data of a group of samples, at one time the computer computed the needed material constants and related data. Table 1 lists the results of the fatigue crack propagation test data of two types of organic glass as well as the data processing.

(1)材 料	(2)预 处 理	应力比 R	C_1	a_1	C_2	a_2	N_0 (周)	N_c (周)	N_L (周)	$\dfrac{N_c-N_0}{N_0} \times 100\%$
YB-3(3)	标准环境	1/3	2.48051×10^{-16}	4.76704	9.27076×10^{-26}	17.2597	89530	86054	24361	−3.88
YB-3(4)	水 浸	1/3	2.00177×10^{-15}	4.09805	5.18507×10^{-24}	15.0078	135618	132705	79003	−2.15
YB-3(5)	标准环境	1/6	2.63333×10^{-16}	4.62419	2.21400×10^{-18}	11.0630	92330	88138	22396	−4.64
YB-3(6)	水 浸	1/6	2.71129×10^{-15}	3.86149	1.84472×10^{-18}	11.0607	107543	105124	69748	−2.25
YB-3(7)	标准环境	1/3	2.11714×10^{-16}	4.54020	8.05170×10^{-19}	10.0308	274753	247412	149992	−9.96
YB-3(8)	湿热老化	1/3	4.90980×10^{-15}	3.89824	3.45725×10^{-64}	27.0468	120808	115034	33867	−4.78
YB-4(9)	标准环境	1/3	3.32725×10^{-17}	7.06012	3.04692×10^{-18}	10.8397	102151	96193	67152	−6.81
YB-4(10)	水 浸	1/3	2.64379×10^{-16}	6.60578	4.39887×10^{-18}	12.1049	108968	101878	58405	−6.50
YB-4(11)	标准环境	1/6	1.71805×10^{-17}	6.90586	9.71696×10^{-41}	19.7061	69484	66454	39223	−4.33
YB-4(12)	水 浸	1/6	2.18917×10^{-16}	5.72328	1.16622×10^{-26}	16.0539	88263	84606	40967	−4.28
YB-4(13)	标准环境	1/10	9.04506×10^{-16}	5.85880	1.99184×10^{-24}	10.4964	60060	57758	30710	−3.83
YB-4(14)	水 浸	1/10	3.69606×10^{-16}	6.46472	3.05436×10^{-97}	16.9067	80852	80258	36723	−0.74
YB-4(15)	湿热老化	1/3	4.63194×10^{-11}	3.32520	1.31358×10^{-18}	13.6114	118348	115137	79316	−2.71

(19) *频率为20Hz，其余试样均为5Hz.

(20)注：C_1、a_1 和 C_2、a_2 分别为折点 j（图1）前后直线对应的材料常数；N_e 和 N_c 分别为平均实测寿命和估算寿命；N_L 为按置信度95%的概率分散带上限（图1）计算的估算寿命的下限值.

Table 1 (see next page)

Table 1 (continued) Fatigue crack propagation test data and
computation results of YB-3 and YB-4 glass.

Key: (1) Material; (2) Preprocessing; (3) Standard
environment; (4) Water immersion; (5) Standard
environment; (6) Water immersion; (7) Standard
environment; (8) Humid heat ageing; (9) Standard
environment; (10) Water immersion; (11) Standard
environment; (12) Water immersion; (13) Standard
environment; (14) Water immersion; (15) Humid
heat ageing; (16)-(18) Cycles; (19)*The frequency is
20Hz, the other samples are all 5Hz; (20) Note: C_1, n_1
and C_2, n_2 are separately the material constants
corresponding to the front and rear straight lines of
turning point; (Fig. 1); Ne and Nc are separately the
mean actually tested life and estimated life; N_r is
the lower limit value of the estimated life calculated
according to the upper limit of the dispersion band
with probability of 95% believability; (21) Stress ratio.

Figure 1 is the lg(da/dN)-g(Δ K) relational curve of YB-3 glass
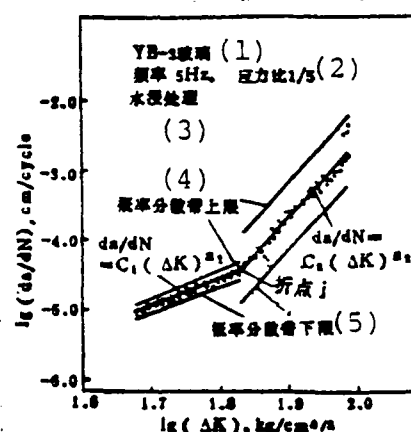drawn from the test data fter using processing.

Fig. 1 lg(da/dN)-lg(Δ K) relationship of organic glass.

Key: (1) YB-3 glass; (2) Frequency is 5Hz and stress
ratio is 1/5; (3) Water immersion processing;
(4) Upper limit of frequency dispersion band;
(5) Lower limit of frequency dispersion band.

The estimated life Nc is calculated by the following formula
using the Romberg numerical value integration method:

$$Nc = \int_{a_0}^{a_j} \frac{da}{C_1(\Delta K)^{a_1}} + \int_{a_j}^{a_b} \frac{da}{C_2(\Delta K)^{a_2}} \quad (4)$$

a_o, a_b and a_j are separately the crack lengths during the initial breaking periods as well as the crack lengths corresponding to turning point j in Fig. 1. The optimal number and optimal position of the turning points on the $\lg(da/dN)$-$\lg$ (ΔK) curve are calculated by the computer based on the principle of the minimum two power method. We can see from Table 1 that the difference between estimated life Nc and mean actually calculated damage life obtained from the computer is very small. Therefore, it can be considered that the automatically obtained turning point numer and its optimal position method are accurate; and the obtained material constants C_1, n_1 and C_2, n_2 are reliable.

3.2 N-a Relationship of Two Types of Organic Glass Under Different Test Conditions

Based on the material constants C_1, n_1 and C_2, n_2 obtained under each test condition, we calculated the alternating load cycle number corresponding to each crack propagation quantity a. After making charts, we obtained Figs. 2-4.
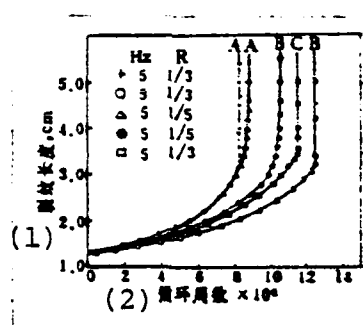

Fig. 2 N-a relationship of YB-3 glass under each test condition.
Key: (A) The sample is processed in a standard laboratory environment; (B) Processed in 20°C water immersion for 24 hours; (C) Processed for 30 days at 60°C saturated water vapor humid heat ageing (Figs. 3 and 4 are the same); (1) Crack length; (2) Cycle number.
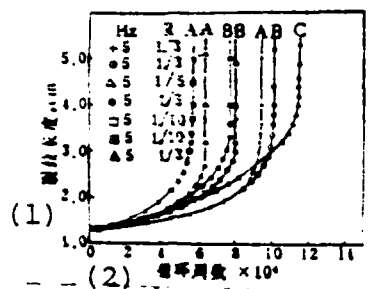
Fig. 3 N-a relationship of YB-4 glass under each test condition.
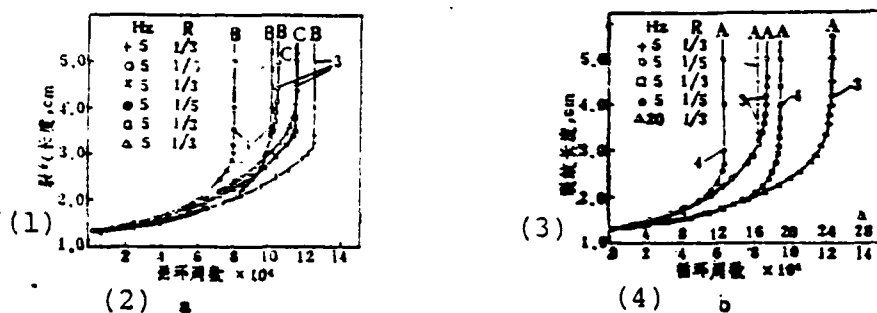Key: (1) Crack length; (2) Cycle number.

Fig. 4 Comparison of the fatigue crack propagation character-
istics of YB-3 and YB-4. 3 and 4 in the figure
separately represent YB-3 and YB-4.

Key: (1) Crack length; (2) Cycle number; (3) Crack
length; (4) Cycle number.

We can see from Figs. 2 and 3 that: when stress ratio R
decreased, the da/dN of the two types of glass increased and
damage life N̄e decreased; when compared with processing at a
standard laboratory environment area, after 24 hours of water
immersion or 30 days humid heat ageing, the da/dN of the two
types of organic glass noticeably lowered and the lengthening
of damage life N̄e is noticeable. We can see from Fig. 4 that:
the test frequency rose from 5Hz to 20Hz and the da/dN of the
YB-3 glass decreased; under the above three test conditions,
the da/dN of the YB-4 glass was slightly higher than that of
YB-3 glass.

3.3 Crack Propagation Characteristics in a Water Environment.

Figures 5 and 6 show the influences of water on the fatigue crack propagation characteristics of the two types of materials when completely immersed in water. The initial ΔK of each test in a water environment increases from the original $38 kg/cm^{3/2}$ to $61 kg/cm^{3/2}$. The existence of water in the crack seriously obstructs the crack's subcritical propagation and the influence of water on the crack growth of YB-4 glass is greater than on YB-3 glass.
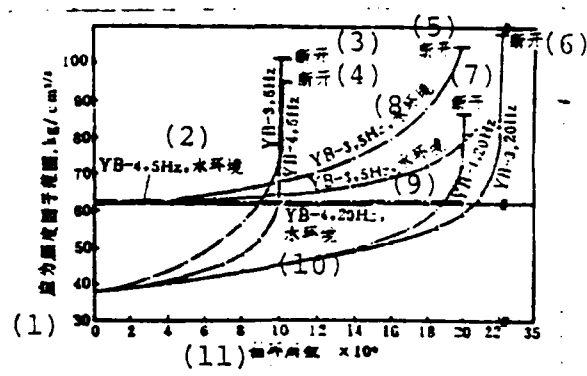
Fig. 5   Influence of a water environment on the fatigue crack propagation characteristics of YB-3 and YB-4.

Key: (1) Stress intensity factor range: (2) Water environment; (3)-(7) Open; (8)-(10) water environment; (11) Cycle number.
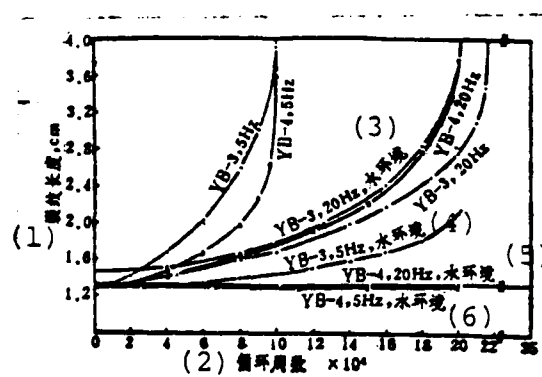
Fig. 6   Comparison of a-N curves of YB-3 and YB-4 glass in air and water environments (the initial ΔK of tests in the water environment is relatively large).

Key: (1) Crack length; (2) Cycle number; (3-(6) Water environment.

107

IV. Discussion

4.1 Influence of Plasticizers and Intermolecular Effects

YB-3 and YB-4 glass contain plasticizers and the latter
also possesses copolymerization components with carboxyl.
The added plasticizers flowing between the large and super
molecules decrease the active force between the large molecules.
This increases the movement of the large molecule structural
elements [11] which causes the material's crack propagation
resistance characteristics to increase. However, at the same
time, this can also decrease the effective binding density of
the large molecules and increase the possibility of slipping
between the molecules and chain section which causes the per-
formance to lower. Therefore, the action of plasticizers is
decided by the overall effects created by the added quantity.
To sum up, it is not advantageous to add too much plasticizer
in organic glass.

By comparing the N-a curves of the two types of glass in
Fig. 4, under the same conditions, the fatigue crack propagation
rate of the YB-4 glass is faster than that of YB-3 glass and
damaging life $\overline{N}e$ is also relatively low. It is clear that be-
cause the YB-4 glass molecules carry carbonyl with very strong
polarity, the intermolecular force is relatively great, the
molecular compliance is not as good as YB-3 glass, under exter-
nal load effects the movements of the molecular chain section
and side radical (the abilities of the α-process and
β-process are relatively poor) do not easily cause the mole-
cules to make the transition from one type of state of equili-
brium to another state of equilibrium and become suitable with
the states of external force effects. At this time, the coarse
wire in the silver streak structure easily weakens and breaks
[9] and therefore the crack propagation rate of the glass can
rise.

4.2 Influence of Alternating Load Frequency and Stress Ratio

The effect law of alternating load frequency on polymers is completely different than for metal materials and the sensitivity of the da/dN of different polymers each is different for frequency changes. Manson and Hertzberg consider that the dependent relationship of the da/dN of polymers to test frequencies is clearly interrelated with the frequency of the β - transformation under test temperature [12]. Afterwards, Hertzberg further pointed out that this is related to the movement frequency of the large molecule chain section of the β-transformation when creating room temperature [13]. The frequency sensitive factor (FSF) is used to indicate the sensitivity level of da/dN to frequency changes. We have discovered that the FSF value is maximum when the polymer and the β - transformation related molecule chain section jumping frequency and test frequency area are in a clear resonance state. This is because the resonance state has effects on the crack tip's local position heating which causes the material to become soft and dulling the crack tip causes the da/dN to decrease. When the organic glass is tested in the frequency sensitive range (0.1-100Hz) at room temperature, the test results completely agree with this conclusion. It is worth pointing out that after the test frequency rises, although it be one cycle of the alternating load, the crack propagation quantity decreases. However, the high-frequency causes the total time of the glass breaking to shorten. For example, when there is 5Hz, the YB-3 glass damage life $\overline{N}e$ is 89,530 cycles which requires 5 hours but the 20Hz damage life is 274,753 cycles which only requires 3.8 hours. Taken from this point, the danger of raising the frequency of the glass is increased.

The decreasing of the alternating load's stress ratio R is in reality to increase the amplitude of the alternating load and increase the impelling of motive power $\triangle K$ of the crack

propagation. Therefore, the fatigue crack propagation rate of the two types of organic glass is accelerated and the damage life is decreased. We can see this law from Figs. 2 and 3.

4.3 Influence of Water Environment and Humid Heat Ageing

We have still not seen reports related to this area. In order to compare the influences of water under various conditions on the material's characteristics, we carried out standard laboratory environment, water immersion and humid heat ageing tests on two types of glass samples and for some of the samples we did tests of immersing the entire crack in water.

We can see from the data in Table 1 and the N-a curves in Figs. 2 and 3 that water has good effects on the fatigue crack propagation resistant characteristics of two types of organic glass. Even though the glass only absorbed 0.10-0.16% of the moisture content after being immersed in water for 24 hours, the damage life was noticeably increased. The influence of the water environment on the characteristics of the two types of organic glass are much greater and this is clearly reflected in Figs. 5 and 6. When tested in a water environment the initial Δ K changed from the original 38kg/cm$^{3/2}$ to 61kg/cm$^{3/2}$ and when the test frequency is 5Hz and 20Hz they separately circulate 200,000 and 350,000 cycles, the cracks in the YB-4 glass still do not propagate. At this time, the stress of the samples with cracks is as shown in Table 2.

应 力 比 (1) R	(2) 中 心 裂 纹 长			
	a=1 毫 米 (3)		a=13 毫 米 (4)	
	P_{max} kg	σ_{max} kg/cm^2	P_{max} kg	σ_{max} kg/cm^2
1/3	2309	233	633	73
1/5	1924	194	527	61
1/10	1710	173	469	54

Table 2 (see next page

Table 2 (continued) Stress of samples with cracks in a water
            environment.
            Key: (1) Stress ratio; (2) Length of center crack;
            (3) Millimeters; (4) Millimeters.

The cracks do not propagate under this type of high dynamic
state stress.   This point has real and important significance.
As regards YB-3 glass, when the frequency is 5Hz, crack pro-
pagation is relatively slow and when 20Hz the effect of water
on the crack tip is not as great as that of YB-4 glass and the
crack propagation is relatively fast.   Naturally, because YB-4
glass contains hydrophilic carbonyl-COOH, the effect of water
on it is much stronger than on YB-3 glass.   The influence of
test frequency changes on the crack tip molecule movement under
the action of water awaits investigation.

    Based on the seeming effects of the microstructure of the
crack tip's silver grain on water [9,14]: on the one hand, the
flow of the water in the silver grain porous structure along
with the effects of the large molecule chain section and side
radicals directly weakens the intermolecular force and thus
raises the compliance of the molecules in the silver grain and
the movement abilities of the structural units.   On the other
hand, when the test frequency approaches the chain section
jumping frequency related to the β-transformation peak reson-
ance occurs, the high molecule movement relaxation time de-
creases and the deformation increases.   The deformation lags
behind one phase as compared to the stress which creates rela-
tively large internal consumption.   If the silver grain holes
and the spaces between the molecules fill with water and single
bundle molecules of water, we can change these into the strain
energy of thermal energy and can transfer them off so that the
firmness of the silver grain thick wire is maintained and the
cracks do not easily carry out subcritical propagation.   The
energy transfer should be the primary cause because only if we
have the strain energy source of the transformed energy

continually transferred off can we cause the crack not to propagate under very large ΔK drive.

4.4 Investigation of the Micromechanisms of the Section Appearance and Fatigue Crack Propagation

(1) Transformation of the Subcritical Area's Crack Propagation Mode

Under alternating loads, when the K_1 created by maximum P_1 at the crack tip is smaller than material fracture toughness K_1, the subcritical propagation area formed by the cracks propagating forward and the slow propagation area of the fracture toughness are two totally different concepts. The difference between their section appearance and crack propagation micromechanism is very great.

We can see from Fig. 7 (see Plate 13) that the subcritical propagation areas of the two types of organic glass have mirror surface to spray surface transition. Moreover, there is a noticeable saw-tooth boundary between the mirror surface and spray surface and the spray surface area of YB-3 glass is much larger than that of YB-4 glass. Skibo and Hertzberg in the same way observed the fatigue crack propagation section of polystyrene (PS) and found this phenomenon [15]. Because the silver streak propagation in organic glass always first propagates in cracks, this transformation is necessarily related to the crack tip's silver grain deformation. Hull considered that when the cracking rate of glass polymers is relatively fast, silver grain bundles form around the main crack tip and the crack propagates passed the silver grain bundle area.

By observing the boundary line between the mirror surface and spray surface, we discovered that: if we add ΔK of the subcritical area under alternating loads, the crack's surrounding area can also form silver grain bundles; the mirror surface reflects that the crack underwent single silver grain propagation and the spray surface reflects that the crack

underwent silver grain bundle propagation. We can clearly see from Fig. 8 that the crack made a transition from one silver grain layer to another. Based on the following facts, we can consider that the shape of the silver grain bundle is related to the size and molecular compliance of ΔK: the areas of spray surfaces of the two types of glass enlarge with the decrease of stress ratio R (i.e. ΔK rises); after water immersion, the sample's spray surface area is large; the spray surface area of YB-3 glass is much larger than that of YB-4 glass. The glass surface is in the plane stress state during tests and this is advantageous to the formation of silver grain bundles. Therefore, the spray surface is always first formed on the two sides of the section and afterwards, following the increase of ΔK, it gradually propagated towards the middle and forms a saw-tooth shaped boundary (Fig. 7). Under the same test conditions, the tooth shaped boundary ranges of YB-3 and YB-4 glass are separately 1.8-3.6cm and 2.9-4.8cm (Fig. 7) but after the crack lengths corresponding to the turning points of the lg(da/dN)-lg(ΔK) broken lines of the two types of glass go through precise computations by the computer, they are separately .173 and 2.640cm. Because of this, it is very difficult to find the precise relationship between the transformation of the mirror surface and spray surface and the turning point of the lg(da/dN)-lg(ΔK) broken line. This is completely opposite of the view in Reference [15].

By means of observations and analysis of the section appearance, we can consider that the transition of the organic glass crack subcritical propagation area's mirror surface to the spray surface reflects the transformation of the crack propagation mode from using single silver grain to using silver grain bundle propagation. This is mainly determined by the molecular structure and composition of the glass as well as the level of ΔK and is unrelated to the turning of the lg(da/dN)-lg(ΔK) curve.

(2) Micromechanism of Fatigue Crack Propagation

Figure 9 (see Plate 13) shows the appearance of the different stages of crack propagation of the two types of glass. We can see that even though the crack's subcritical propagation area is not the same as the slow propagation area of the fracture toughness, yet their appearances and mechanisms should be the same in the fast speed fracture area. When comparing the fatigue grain lines of the different glasses in Fig. 10, naturally the better the compliance of the large molecules the easier the formation of grain lines.
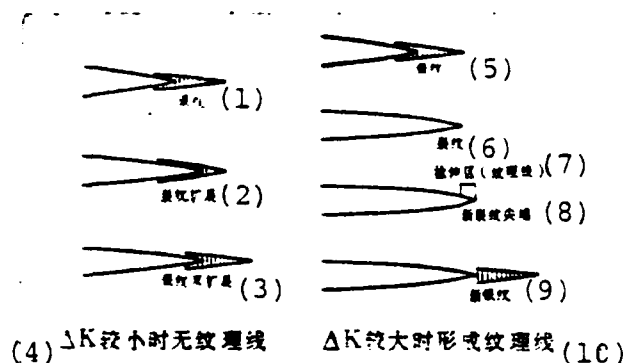

Fig. 11 Crack propagation of subcritical mirror surface.

Key: (1) Silver grain; (2) Crack propagation; (3) Silver grain bundle propagation; (4) No grain lines when ΔK is relatively small; (5) Silver grain; (6) Crack; (7) Tension area (grain lines); (8) New crack point; (9) New crack; (10) Grain lines form when ΔK is relatively large.
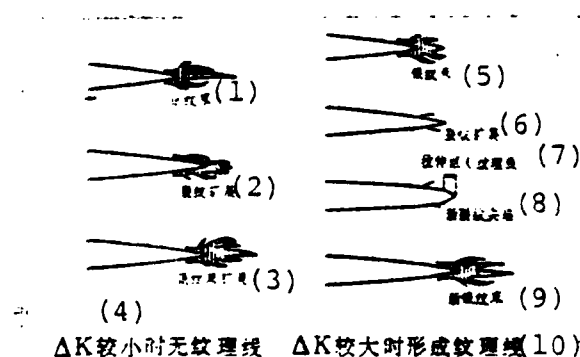

Fig. 12 Crack propagation of subcritical spray surface.
(see next page)

Fig. 12 (continued)

Key: (1) Silver grain bundle; (2) Crack propagation:
(3) Silver grain bundle propagation; (4) No grain lines
when ΔK is relatively small; (5) Silver grain bundle;
(6) Crack propagation; (7) Tension area (grain lines);
(8) New crack tip; (9) New silver grain bundle;
(10) Grain lines form when ΔK is relatively large.

Based on the following facts, this paper proposes a corrected
model of the micromechanism of the crack's subcritical propa-
gation of Reference [15] (Figs. 11 and 12): the mirror surface
reflects that the cracks used the single silver grain mode for
propagation and the spray surface reflects that the cracks used
silver grain bundle areas for propagation; one cycle of the
alternating load showed one fatigue grain line; there were no
fatigue grain lines when ΔK was relatively low which shows
also that the cracks continually propagated and when ΔK was
relatively high grain lines appeared which shows discontinuous
crack propagation; on both the mirror surface and spray surface
we could observe grain lines which explains that the appearance
of grain lines is only related to the ΔK value but is unre-
lated to the crack propagation mode.

Under alternating loads, the thick wire in the silver grain
gradually cracks due to the weakening of the orientation mole-
cules and the mutual slipping of the molecules etc. which cause
the cracks to propagate forward. During the initial period of
crack propagation, ΔK is relatively small and the insufficient
energy causes the crack tip to directly propagate to the silver
grain tip after one cycle of the alternating load. Therefore,
the entire cracking propagation is continuous and goes not form
grain lines. After ΔK reaches a certain level, the crack has
sufficient energy to quickly propagate to the silver grain tip
after one cycle of the alternating load. Afterwards, the ten-
sion area and relatively dull new crack tip form at the crack
tip. At this time, crack propagation is obstructed resulting
in sufficient time to form new silver grain in the new crack tip
area and elongation of a certain length. The fatigue grain lines

115

are created by the tension area and are the remaining marks of the molecule relaxation on the section. They can very notice-ably only form one grain line with one cycle of the alternating load. The silver grain bundle method of propagation is the crack propagation mode when ΔK is relatively high and it is easy to form silver grain materials. Aside from the formation of the spray surface due to the silver grain bundle, the crack propagation mechanisms should be the same.

Conclusion

1. Under dry conditions, the fatigue crack propagation re-sistance characteristics of YB-3 glass are slightly better than those of YB-4 glass. Water has excellent effects on the crack propagation resistance characteristics of the two types of glass and after water immersion and humid heat ageing, the glass absorbed a small amount of moisture content so that the crack propagation resistance characteristics of the material notice-ably increased. When the crack was completely immersed in water, the effects of the water were even stronger and under a very high ΔK level the cracks still did not propagate. The YB-4 glass was more strongly influenced by water than the YB-3 glass. That is, in a water environment, the crack propagation resistance characteristics of the former were better than those of the latter.

2. The stress ratio and frequency of the alternating loads has a relatively large influence on the fatigue crack propa-gation characteristics of organic glass. When the stress ratio decreases, the da/dN of the two types of glass increase and the damage life decreases. After the frequency increased from 5Hz to 20Hz, the da/dN of YB-3 glass decreased.

3. The phenomenon of mirror surface to spray surface trans-ition exists in the crack's subcritical propagation area. This

phenomenon reflects the change of the crack propagation from the single silver grain mode to the silver grain bundle mode. It is determined by the structure, composition as well as the $\triangle K$ level of the high molecule material yet is unrelated to the lg(da/dN)-lg($\triangle K$) curve.

4. After $\triangle K$ reaches a certain level, fatigue grain lines appear in the subcritical area which shows that the cracks have discontinuous propagation. When there is one cycle of the alternating load, one grain line appears.

References

[1] Martin, G.C., Avail.Univ.Microfilms, Order No.77-12,(1976) 834.

[2] Kim, S.L.,Polym.Eng.Sci., 19(1979), 145-150.

[3] Arad, S., J.Mech.Eng.Sci., 14(1972), 328.

[4] Mukherijee, B., Exp.Mech., 2(1971), 433.

[5] Radon, J.C., Polym.Eng.Sci., 15(1975), 500-506.

[6] Radon, J.C., Polym.Eng.Sci., 15(1975), 507-514.

[7] Hertzberg, R.W., ASTM. STP 536,(1973), 391-403.

[8] Hertzberg, R.W., Polym.Eng.Sci., 15(1975), 252-260.

[9] Chen Ruoxi, Shao Yujun and Fan Tang, Aeronautical Materials (Special Edition), 2(1982), 40-46.

[10] Chen Ruoxi, Data Processing and Life Estimations of Fatigue Crack Propagation Tests (ALGOL Program), Beijing Institute of Aeronautical Materials, (Internal Materials), 1981.

[11] Lebedeva, V.I., Plast.Massy, 6(1974), 53-54.

[12] Manson, J.A., Hertzberg, R.W., Polymer, 16(1975), 850-851.

[13] Hertzberg, R.W., Manson, J.A., Polymer, 19(1979), 358-359.

[14] Hull, D., The Mechanics and Physics of Fracture, Churchill College, Cambridge, 1985, 13/1-13/7.

[15] Skibo, M.D., Hertzberg, R.W., J.Mater.Sci., 11(1976), 479-490.
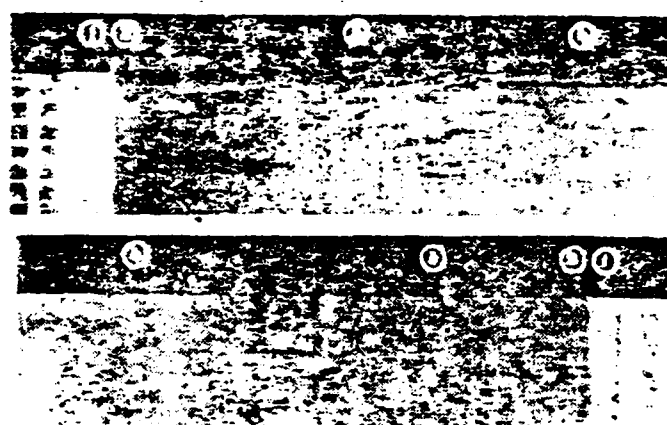
Fig. 7   Sample sections of the fatigue crack propagation of
two types of organic glass, YB-3 (above) and YB-4 (below).

Key: (1) Saw-tooth fracture; (2) Prefabricated fatigue
crack; (3) Subcritical propagation area; (4) Fast
propagation area.

Fig. 8 In the mirror surface area to spray surface area
transition, the crack propagation goes from bottom
to top, x 200.

(1)	(2)	(3)	(4)
快速断裂区	快速断裂-亚	出现纹理线	开始扩展
的瀑物线条	临界扩展边界		
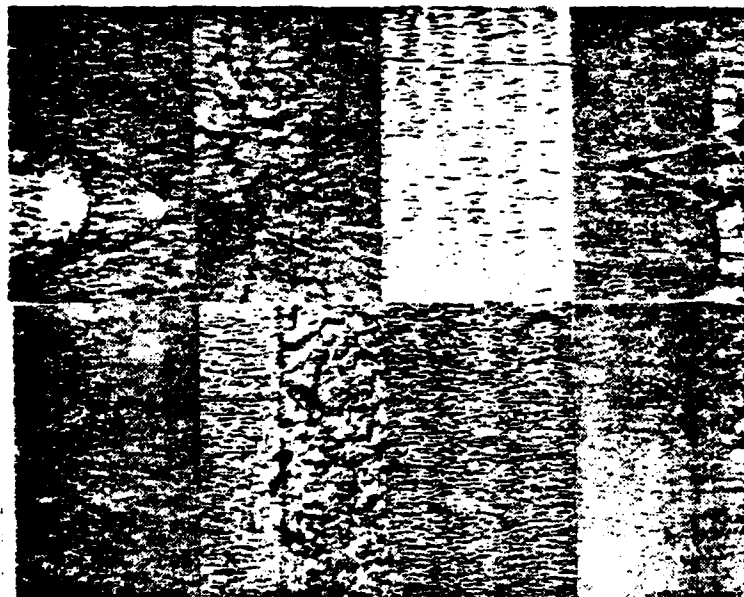
Fig. 9 Appearances of each stage of fatigue crack propagation

of YB-3 (above) and YB-4 (below) glass, x 200.

Key: (1) Parabolic strips of fast fracture area;
(2) Fast fracture - subcritical propagation boundary;
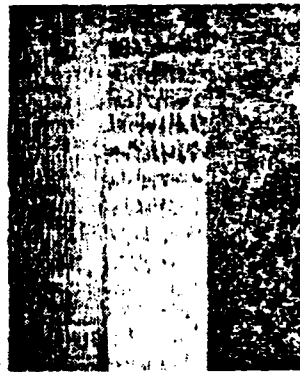(3) Appearance of grain lines; (4) Initial cracking.

Fig. 10 Comparison of fatigue grain lines of YB-2 (left),
         YB-3 (middle) and YB-4 (right) glass.

THE EFFECTS OF NON-METALLIC INCLUSIONS IN STEEL ON FATIGUE PROPERTIES

Zhang Detang, Li Shuyuan and Xia Huiqin

Abstract

This paper studies the effects of inclusions in two types of steel, 38CrMoAlA and 30CrMnSiA, on fatigue properties. The results of the study show that under conditions wherein the inclusion content is basically the same, the size, shape and distribution characteristics have marked effects on fatigue life. The particle sizes of the inclusion directly control the nucleation and propagation of the cracks. When the mean diameter of the inclusion is larger than 40 μm, the proportion of fatigue failures caused by inclusions can reach above 95%. Therefore, on the basis of controlling the inclusion content, the fatigue properties can be improved by decreasing the dimensions of the inclusion particles and changing the unfavorable geometric shapes and distribution.

The effects of non-metallic inclusions in steel on fatigue properties gained wide attention early. The fatigue damage caused by non-metallic inclusions in high strength structure steel has already been verified in many works [1,2]. At present, it is commonly considered that oxides, especially calcium aluminate, aluminum oxide and spinel type inclusions cause the most serious stress concentration. Therefore, the existence of these inclusions have marked harmful effects on the fatigue properties of steel materials (or parts) and often become the source of fatigue crack sprouting and even cause early fatigue damage [3]. Yet, there has been very little research done on the micromechanism of crack behavior between the inclusions and steel base body and there has been even less research on the

quantitative and qualitative effects of the sizes, shapes and distributions of inclusions on fatigue properties.

In 38CrMoAlA and 30CrMnSiA etc. structural steels, often because the metallurgical defects create product abandonment, human power and material resources are lost. Thus, it is urgently hoped that there be a quantitative or qualitative relationship between the inclusions and the fatigue properties which will act as the basis for material testing and judging product quality. For this reason, we studied the effects of the sizes, shapes and distributions of the inclusions on the fatigue properties.

I. Materials and Test Method

The materials used for the tests were 38CrMoAlA and 30CrMnSiA steels. The inclusions contained in these two types of steel were determined by comprehensive analyses. Aluminum nitride was dominant in 38CrMoAlA and calcium aluminate was ·dominant in 30CrMnSiA. These two types of inclusions are both embrittlement inclusions. These two types of steel are separately processed into board and bar samples. In order to establish the relationship of the sizes, shapes and distributions of the non-metallic inclusions and the fatigue properties, we separately carried out mechanical polishing of two test surfaces of board_fatigue samples. Afterwards, we observed the shapes, sizes and distributions of the inclusions in a 10x10mm area of the sample's test region. At the same time, we separately made photographic recordings as a basis for qualitative and statistical analyses as shown in Fig. 1 (see Plate 13). Figure 1a is the board sample and the black spots in the 10x10cm area indicate the positions of the recorded inclusions as shown in Fig. 1b.

We used the metallographic and electronic probes and electron

diffraction etc. methods to determine the type and microhardness of the inclusions. On the basis of common observations, we used the metallographic weighing method and image quantitative analyzer to determine the particle size and content (area %) of theinclusions. Further, based on the differences of their mean diameter size, we divided the samples into the three categories of A, B and C. The inclusion measurement results are listed in Table 1.

(1) 钢种与热处理	(7) 试样编号	(8) 夹杂物类型	(15) 显微硬度 HV, kg/mm²	(16) 夹杂物平均直径 d, μm	(17) 含量,% d60×400*
38CrMoA1A	38A	(9) 氮化铝	900~1000	10~15	0.18
(2) 940°C30分钟油淬	38B	(10) 氮化铝	900~1000	30~35	0.20
(3) +650°C1小时油冷	38C	(11) 氮化铝	900~1000	40~45	0.21
30CrMnSiA	30A	(12) 铝酸钙	1100	10~15	0.16~0.19
(4) 890°C30分钟油淬	30B	(13) 铝酸钙	1100	30~35	0.18~0.21
(5) +520°C1小时油冷	30C	(14) 铝酸钙	1100	40~45	0.17~0.20

(6) * 400倍60个视场的定量计算结果

Table 1   Results of qualitative and quantitative analyses of the inclusions.

Key: (1) Steel type and heat process; (2) Oil quenching at 940°C for 30 minutes; (3) Oil cooling at +650°C for 1 hour; (4) Oil quenching at 890°C for 30 minutes; (5) Oil cooling at +520°C for 1 hour; (6)*Quantitative calculation results of 60 viewing fields at 400 power; (7) Sample number; (8) Inclusion type; (9)-(11) Aluminum nitride; (12)-(14) Calcium aluminate; (15) Microhardness; (16) Mean diameter of inclusion; (17) Content.

On the basis of common observations of the samples, we selected representative typical samples and carried out fatigue tests. We also continuously took samples and used a metallographic microscope to observe the relationship of the cracking between the inclusion on the sample surface and the steel base body as well as the effects of the particle sizes of the inclusions on the fatigue crack propagation rate. Afterwards, we used a scanning microscope to observe the fatigue sources

caused by fractures and traced inclusions and also observed the crack appearances between the inclusions and steel base body. The board and bar fatigue tests were separately carried out on cantilever type repeated flexure (1,500 times/minute) and double fulcrum bridge type rotating flexure (3,000 times/minute) fatigue testers.

The fatigue limit when the samples of two types of steel were in cycle number $N=10^7$ were determined by the rising and falling method and its calculating formula is as follows:

$$S_r = \frac{1}{n} \sum_{i=1}^{m} U_i S_i \quad [4]$$

In the formula: S_r is the stress mean value dominated by the number of tests; S_i is the test stress of the i stage; U_i is the number of samples of the i stage; m is the number of stages of the stress level made by the rising and falling method; n is the total number of samples.

Aside from using the rising and falling method to determine the fatigue limit, we also drew the S-N curve. Based on the observation results of the number, size, shape and distribution of the inclusions, we can determine the differences of the number or particle size of the inclusions which cause fatigue property data dispersion. We can thus draw the S-N curve which truly reflects the effects of inclusion size on fatigue life.

II. Test Results and Discussion

2.1 Effects of Inclusion Particle Size

The relationship between the stress level and number of fatigue cycles is shown in Fig. 2. We can see from the S-N curve in Fig. 2 that although the difference between the inclusion contents of the 38A and 38B samples is not great, yet because the mean diameters of the inclusions are different,

the fatigue strength limit decreases from 61kg/mm^2 to 57kg/mm^2, a decrease of 6.6%.

Based on the calculation results by the rising and falling method, when comparing the 38A and 38B and the 30A and 30B, the fatigue strength limit decreases 6-7%.

Under certain inclusion shape and distribution conditions, we studied the effects of inclusion size on fatigue life and the data and statistical results of tests on 38A, 38B and 38C samples showed that the fatigue life was markedly effected by the inclusion particle size. We can see from Fig. 3 that inclusion particle size has important effects on the nucleation and propagation rate of fatigue cracks.
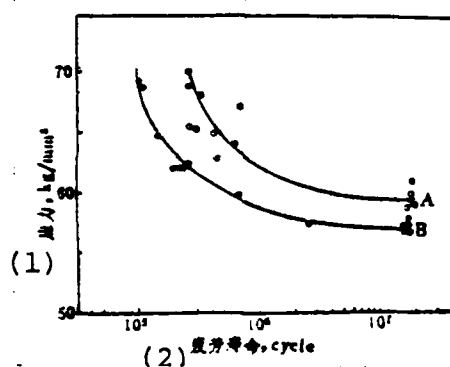

Fig. 2 Relationship between stress amplitude and fatigue life.
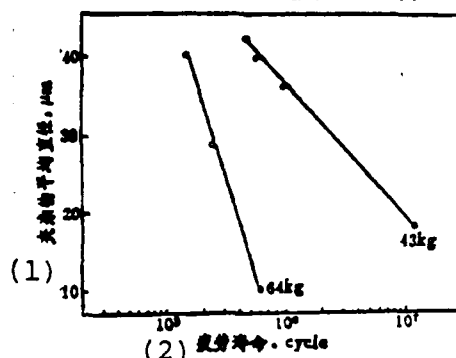Key: (1) Stress; (2) Fatigue life.

Fig. 3 (see next page)

125

Fig. 3 (continued) Relationship between inclusion size and fatigue life.

Key: (1) Mean diameter of inclusion; (2) Fatigue life.

Under the same stress level ($66kg/mm^2$) conditions, the different sized inclusions observed changed with the number of cycles and we also observed the nucleation and propagation process of the cracks as is shown in Fig. 4. We can see from Fig. 4 that when inclusions A, B and C are all located in the same stress area, the stress of the positions occupied by inclusions A (about 20μm) and B (about 40μm) is inferior to the position occupied by inclusion C (about 125μm). However, because the dimensions of inclusion C are much larger than those of A and B, the crack gives priority to nucleation in the inclusion C area. After nucleation, the cracks use very fast speed propagation and the crack nucleation of inclusions A and B occur later. At the same time, the propagation rate of the microcracks is very slow and within this, the micro-cracks caused by inclusion A appear not to propagate.
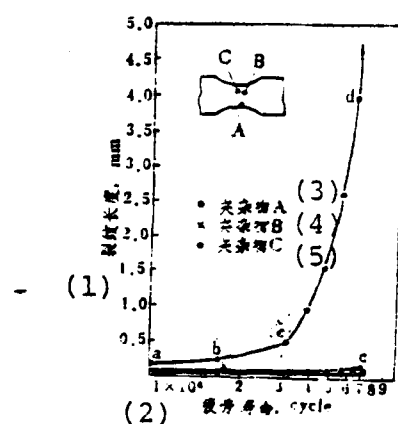

Fig. 4 Relationship between cracks caused by calcium aluminate inclusions and the number of cycles.

Key: (1) Crack length; (2) Fatigue life: (3) Inclusion A; (4) Inclusion B; (5) Inclusion C.

In Fig. 4, each point of inclusion C on the curve has a

corresponding metallographic picture as shown in Fig. 6 (see Plate 13). For example, on the a point position (see Fig. 5A) we have already observed microcracks. At this time, the ratio of the number of cycles when microcracks are produced and the number of cycles when there is fatigue loss is $N_o/N_f=0.1$. We can see from Fig. 5a that when inclusion C is under alternating stress effects, the cracks give priority to inclusions vertical to the tension stress direction and nucleation in the steel base body's common boundary surface (see the position pointed to by the arrow in the figure). When inclusion C is in the b point position on the curve (see Fig. 5b), we discover that there is propagation on the microcrack (at this time, $N_o/N_f=0.2$). When inclusion C reaches the C point on the curve ($N_o/N_f=0.44$) (see Fig. 5^C), we can clearly see from Fig. 5c that before the crack rapidly propagates, the common boundary between the inclusion and steel base body is gradually separated and joined with the microcrack. Therefore, the actual crack length should be calculated using the sum of the micro-crack length and inclusion's diameter size beginning when the earliest microcracks are produced. When inclusion C is in the d point position on the curve, the crack propagation rate drastically increases and N_o/N_f has already reached 0.8 (i.e. 80% of the total life). At this time, the common boundary between the inclusion and steel base body is completely separated and joined with the crack into a continuous crack path, that is, it produces instantaneous cracking. See Fig. 5d. Figure 5^e is the appearance of the inclusion floating on the base body after cracking. Although the inclusion is still embedded on the base body, yet the common boundary between the inclusion and steel base body has already been separated as shown by the arrow. When the fracture endures slight vibration, the inclusion immediately separates from the base body. Fig. 5f is the scanning microscope picture of the inclusion nest remaining after the inclusion separates from the base body. We can clearly see from the picture that this inclusion

is the source of the fatigue damage.

We used a scanning microscope to observe in detail the fatigue fractures of 38A, 38B and 38C samples. Results from a large number of statistics on fatigue source observations show that: for the 38C group samples, the ratio of fatigue failures caused by inclusions reached about 95%; for the 38B group samples, the ratio of fatigue failure caused by inclusions was between 70-80%; and for the 38A group samples, the ratio of fatigue failures caused by inclusions was below 50%. This shows that the mean diameter sizes of the inclusions have marked effects on the ratio of fatigue failures. Following the increase of the mean diameter of the inclusion, the ratio of fatigue failures drastically increases as shown in Fig. 6.
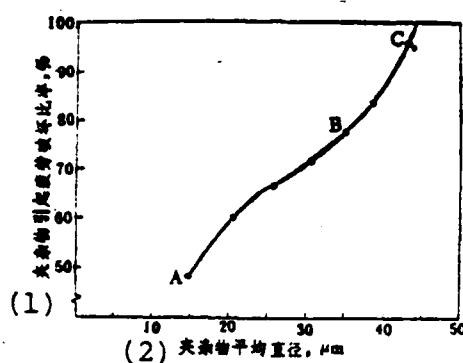

Fig. 6   Relationship between inclusion particle size and fatigue failure ratio.

Key: (1) Ratio of fatigue damage caused by inclusions; (2) Mean diameter of inclusions.

2.2   Effects of Inclusion Shapes and Distributions.

Inclusion shapes and distributions have effects on fatigue properties which cannot be ignored. The sizes of the stress concentration caused by the inclusions inside the steel base body are related to the shapes of the inclusions and the smaller the radius of the inclusion curvature, the more serious the stress concentration. Therefore, the stress field around

the sharp inclusions is much larger than the stress field of
the circular inclusions. Because of this, in inclusions of
the same size, when the sharp inclusions are under alternating
stress, the cracks give priority to nucleation in the sharp
angle area vertical to the tension stress direction. Moreover,
the crack propagation rate is also much faster than that of
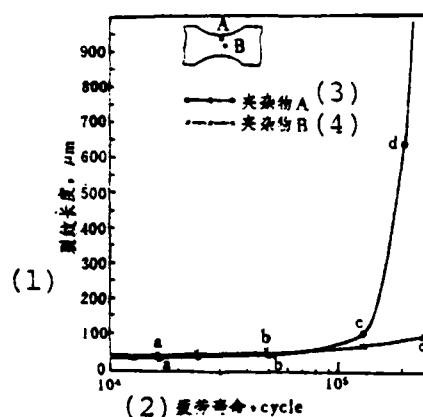circular inclusions [5] (Fig. 7).

Fig. 7   Relationship of cracks caused by different shaped
         aluminum nitride and the number of fatigue cycles.
         Key: (1) Crack length; (2) Fatigue life; (3) In-
         clusion A; (4) Inclusion B.

We can see from Fig. 7 that when inclusions A and B are
located in the same type of stress area, because inclusion A
is sharp, under the effects of alternating stress, the cracks
give priority to nucleation of the inclusion in the sharp area
vertical to the tension stress direction as shown in Fig. 8
(see Plate 14).

When the curve of inclusion A in Fig. 7 reaches the C
point position, the crack propagation rate rises drastically
producing instantaneous cracking in a very short period of time.
The crack propagation form corresponding to point C is shown in
Fig. 8c. At the same time as this, although the diameter of
inclusion B is larger than that of A, because its curvature

129

radius is relatively large, under alternating stress, the stress concentration caused by inclusion B is much smaller than that of inclusion C. Therefore, when inclusion B goes straight to the C point on the curve (see Fig. 7), the microcracks still have no noticeable propagation as shown by a, b and c of inclusion B in Fig. 8.

Test results show that when the sharp angle of the sharp inclusions is vertical to the stress axis direction, it has greater danger than circular inclusions. We used continuous observations of fracture behavior between the inclusions and the steel base body to describe models of fatigue crack nucleation caused by embrittlement inclusions and the propagation process in certain structural steels as shown in Fig. 9 (see Plate 14). In the figure, a is the original state, and the inclusions and steel base body closely joined together. Under alternating stress effects, the cracks give priority to nucleation of the sharp area of inclusions vertical to the tension stress direction. Afterwards, the common boundary between the inclusions and steel base body gradually separates (see Fig. 9b). Following the increase of the number of cycles, slipping is continuously produced around the inclusions and the microcracks also continuously join and propagate (see Fig. 9c). Before the cracks continue to propagate, the common boundary between the inclusions and steel base body gradually separates and the cracks join. At this time, the crack propagation rate sharply increases and forms a connected crack path as shown in Fig. 9d. After a drastic increase in the crack propagation rate, instantaneous cracking is very quickly produced. Figures 9e and f are separately the appearances before and after instantaneous cracking.

The reasons for the production of microcracks can be explained from the several following areas: (1) the aluminum nitride and calcium aluminate which we are studying are both

embrittlement inclusions. Their microhardness value (HV) is
2.5-3 times that of the steel base body [6]. During the de-
formation process, the steel base body produces plastic deform-
ation but the inclusion itself has no deformation. Due to the
differences in deformation behavior, strong stress concentration
is produced in the common boundary area between the inclusions
and steel base body so that the common boundary between the
inclusions and steel base body easily opens and produces micro-
cracks. Thus, it can be considered that the inclusion itself
is a germinating type microcrack [7]. Further, because the
maximum stress acts on the common boundary of the inclusions
and steel base body it is equivalent to the sum total of the
stress concentration caused by the externally added stress and
inclusions inside the base body. This total stress can be
expressed by the following form: $\sigma y \cong 2 \sigma_o$ [8]. In this
formula, σ_o is the externally added stress; σy is the total
stress acting on the common boundary of the inclusions and
steel base body.

Therefore, under the effects of alternating stress, there
will be doubled stress acting on the common boundary of the
inclusions and steel base body which will produce strong stress
concentration resulting in the production of microcracks.

(2) The differences of the elastic modulus between the
inclusions and steel base body can also produce stress con-
centration. Elastic modulus E_i of the aluminum nitride and
calcium aluminate is 1.5-2.0 times larger than elastic modulus
E_m of the steel base body. Because the stress concentration
coefficient changes with E_i/E_m, the larger E_i/E_m, the more
serious the stress concentration [8]. Therefore, the differ-
ences from the elastic modulus carry additional stress concen-
tration causing the common boundary between the inclusions and
steel base body to become a thin and weak link of the crack
sprouting.

(3) The differences of the heat expansion coefficient cause the inclusions to produce additional tension stress inside the steel base body. Because the heat expansion coefficient of the aluminum nitride and calcium aluminate inclusions is much smaller than that of the steel base body, after the steel undergoes heat treatment, latent tension stress embedded in the steel base body is produced around the inclusions [9].

By using a scanning microscope to observe fatigue fractures which have passed through three halted loads, we could draw the three-dimensional appearance of the opening process of the common boundary between the inclusions and the steel base body as shown in Fig. 10 (see Plate 14). After observations of matching fractures, we could see that the boundary of the inclusions and steel base body gradually separate as well as the separating marks left from each halted load. At the same time, we could also see the tire pattern in the separating nest caused by the inclusion edge. It shows the microcharacteristics of the later period of fatigue crack propagation. It is the stage of drastic increase in the fatigue crack propagation rate and the marks of one time of compression stress on the matching fracture from one rubbing of the inclusion edge. Therefore, it is closely related to the contour of the inclusion. The trend of the tire pattern is vertical to the direction of the fatigue crack propagation (see the direction pointed to by the arrow in Fig. 10b).

2.3 Effects of Inclusion Distribution Density

From the point of view of the stress concentration caused by inclusions, the stress field produced by the inclusions around the steel base body is closely related to the sizes and distribution of the inclusions. The effective volume of the stress field affecting the steel base body is four times that of the radius of the circular inclusions [8].

When the two inclusions are close together, because of
the superposition effects of the stress field, its harmful
effects are equivalent to the effects of the sum of the two
inclusion sizes (see Fig. 11, Plate 15). We can clearly see
from Fig. 11 that the crack nucleation and propagation process
are similar to an entire inclusion.

When the distance between the two inclusions is relatively
close, under the effects of alternating loads, the local area
surrounding the two adjoining inclusions simultaneously pro-
duces slipping. Because of the closeness of the stress fields
in the stress concentration produced by the common boundary
area between the inclusions and steel base body, the micro-
cracks produced by the two inclusions join together very
quickly and greatly accelerate the propagation rate of the
fatigue cracks (see Fig. 12, Plate 15).

The test results show that because the stress field pro-
duced by the inclusions enlarges with the increase of the
inclusion dimensions, the relatively large inclusions take
priority in producing cracks. At this time, the formed crack
length is indicated by the sum of the diameter of the inclu-
sion and the crack length.

Concluding Remarks

1. The fatigue properties of embrittlement inclusions
(calcium aluminate, aluminum oxide and aliminum nitride etc.)
have marked harmful effects on steel. The cracks which first
appeared on the sample's surface (or just embedded in the
subsurface of the sample) are larger than the inclusion posi-
tion of 20μm.

2.   The size of the inclusion particles is an important
factor influencing fatigue crack nucleation. When the mean
diameter of the inclusions is larger than $40\,\mu m$, the ratio of
the fatigue failures caused by the inclusions reaches to over
95%.

3.   The sharp inclusions have even worse effects than the
same sized circular inclusions. Therefore, the critical dim-
ensions of the fatigue failures caused by sharp inclusions
should also be smaller than the critical dimensions of circular
inclusions.

4.   The density of the inclusion distribution is large and
there are many possibilities for crack nucleation so that the
number of free paths for crack propagation become numerous.
Because the propagation of cracks is effected by the inclusion
stress field, the cracks join together relatively fast which
accelerates the propagation rate of the fatigue cracks.

References

[1] Araki Tohito, Iron and Steel, 56(1970), No. 12,1737.

[2] Uchiyama To, Iron and Steel, 57(1971), No. 13, 1891.

[3] Lankford, J.,-International Metal Reviews,22(1977),221.

[4] Gao Zhentong, editor, Fatigue Property Testing, National
    Defense Industries Press,1980,P106.

[5] Kakuten Hoei, Iron and Steel, 57(1971),No.2,352.

[6] Zhang Detang and Shi Bingdi, Illustrative Plates of Non-
    Metallic Inclusions in Steel, National Defense Industries
    Press, 1980,P26.

[7] Lu Suo, translator, Metal Fatigue Damage, National Defense
    Industries Press, 1976,P22.

[8] Kiessling, R., Hordbery, H., Production and Application
    of Clean Steels, 1972, P179-185.

[9] Brooksbank,D., Andrews,K.W., Production and Application of
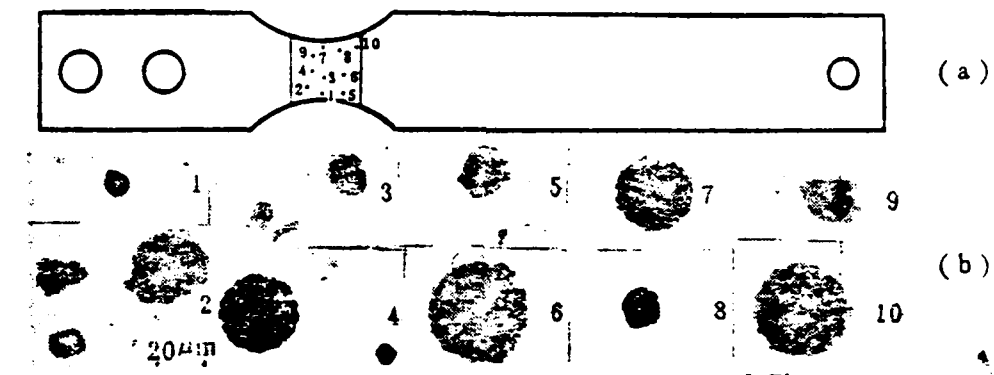   Clean Steels, 1972, P185-199.

Fig. 1 Sizes, shapes and distributions of calcium aluminate on the polished surfaces of 30CrMnSiA samples.
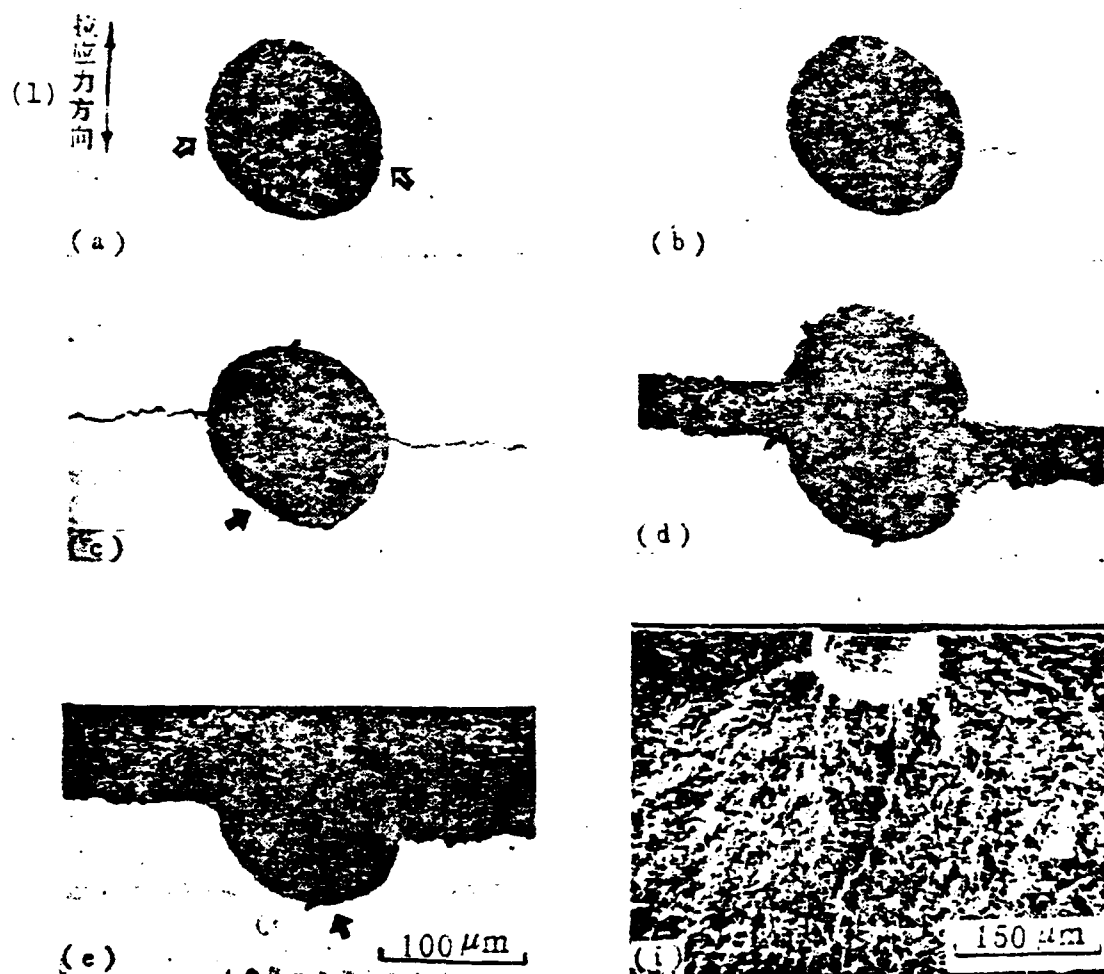
Fig. 5 Fracturing process between annular inclusions and steel base bodies.
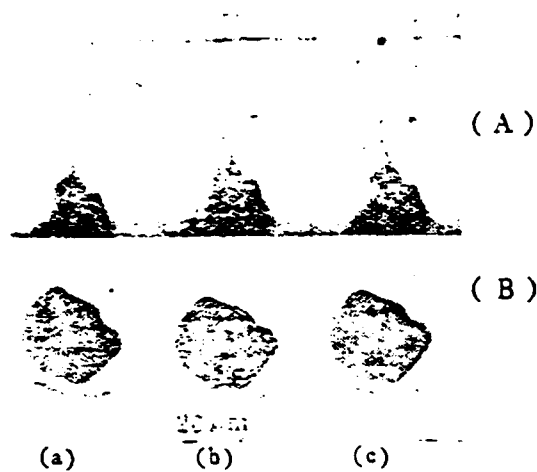
Key: (1) Tensile stress direction.

136

Fig. 8 Crack propagation process of inclusions-corresponding to Fig. 7.
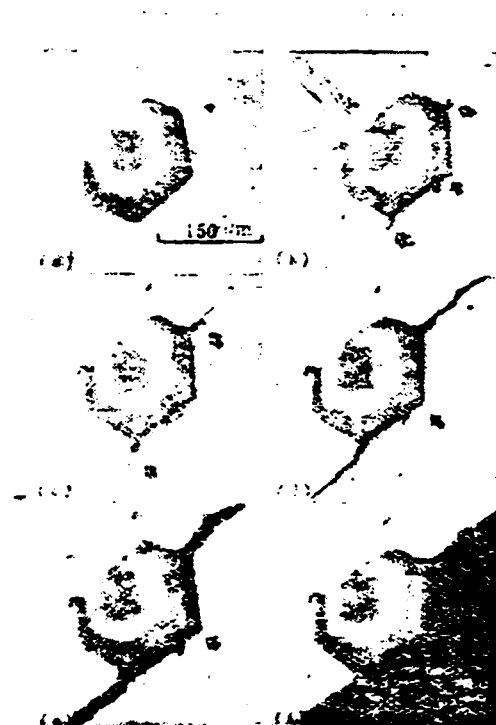

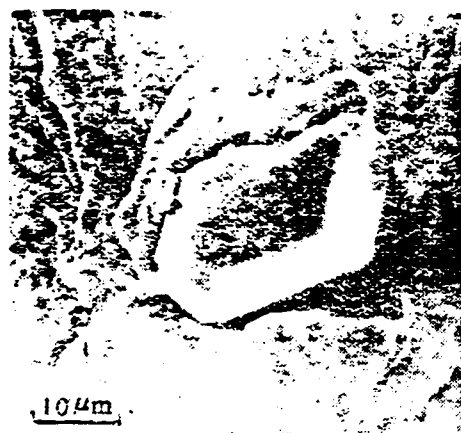Fig. 9 Fracturing process between embrittlement inclusions and steel base bodies.

137

Fig. 10 Interface separation process between inclusions and steel base bodies (quadratic photos with scanning electron microscope).
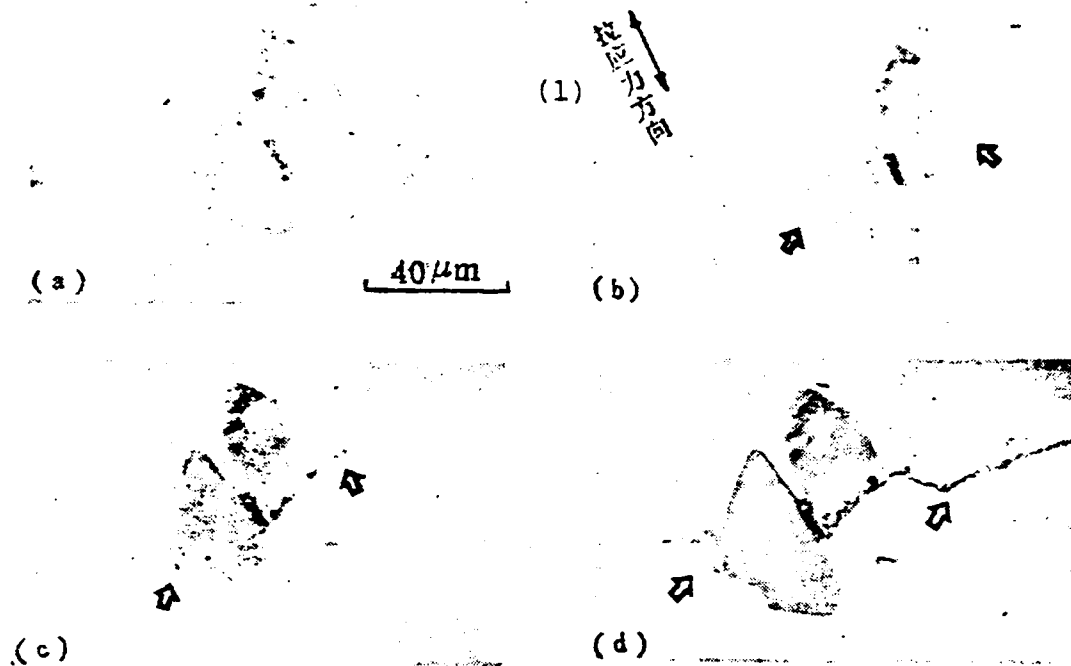
Fig. 11 Crack nucleation and propagation process of two inclusions brought close together.

Key: (1) Tensile stress direction.

Fig. 12 Propagation of the cracks of two adjacent inclusions.

CHARACTERISTICS OF INITIAL PERIOD FATIGUE CRACK PROPAGATION
OF METALS AND ITS AFFECTING FACTORS

Yan Minggao

Abstract

This paper reviews the mechanisms and characteristics of
fatigue crack propagation in various metals and alloys at
near-threshold range.

Test results from a series of microfractographic analyses
of samples and structures showed that the fracture patterns
which are predominantly produced at near-threshold range are
the facets or river patterns. The interrelationship of the
orientation of facets for different metals and alloys with
crystal lattice structures was described with modes of slip
and fault energy. A general trend of fatigue crack propaga-
tion characteristics was proposed under non-axial loading.

In this paper, the interrelationship between the fatigue
limits of plain and notched samples and fatigue thresholds as
well as the mechanism of the fatigue crack propagation in
short cracks was evaluated. The crack propagation behaviors
in short cracks can be generally expressed as:

$$\Delta K_{th} = f(a)\,\Delta\sigma_{th}\sqrt{\pi a}$$

In the formula, f(a) is the function of the crack length and
sample's geometric shape.

This paper also reviewed the influences of stress ratio,
microstructure and environment on fatigue crack propagation
behavior at near-threshold range. It is suggested the concepts
"oxide inducted" and "roughness inducted" produced by crack

closure can be used to explain the effects of the above men-
tioned factors on fatigue crack propagation behavior at near-
threshold range in structural materials.

I. Preface

Since the beginning of the century with the axle fracture
accidents of American trucks, research on fatigue fractures
has gained wide interest and a great deal of test research and
theoretical analysis was begun. Nevertheless, relatively
serious disastrous accidents still occurred from the "free axle"
fractures to the "Comet" airliner disintegrations and the de-
molishing of rocket shells during the 1940's up until the
collapse of the oil field drilling platform on the North Sea
during the 1980's etc. This explains that the sprouting and
propagation of fatigue cracks in the stress concentration of the
structural components is often difficult to avoid. Therefore,
studies on the initial period of fatigue crack propagation of
notched and microcrack components are concerned with how to
take preventative measures which will have important theories
and real significance.

It is generally considered that the propagation of fatigue
cracks can be divided into three stages. During the initial
stage of propagation, the very low propagation rate is used
($da/dN < 10^{-5}$ mm/cycle). This area is the non-continuous
propagation area and appears as a type of crystallographic
pattern of facets or river pattern fractures; when $da/dN >$
10^{-5} mm/cycle, then it reaches the continuous propagation area
and the fracture appearance is predominantly fatigue cracks;
when $da/dN > 10^{-3}$ mm/cycle, it is then the "static mode" pro-
pagation area, the fracture appearance is predominantly tough
nests, intercrystalline fractures or fiber tears. The entire
da/dN-K curve can approximately be described by the "S" shaped
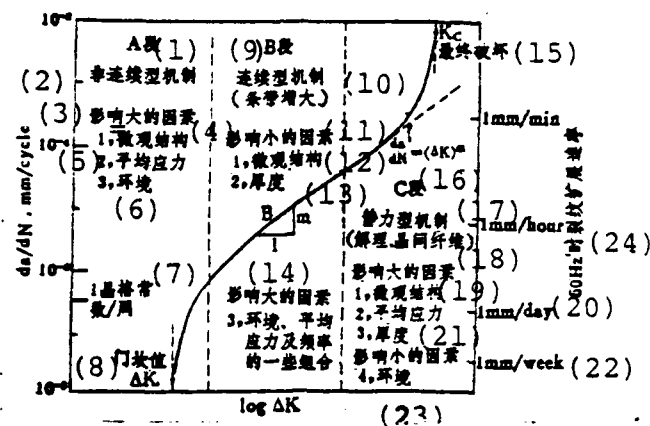curve as shown in Fig. 1 [1,2].

Fig. 1 Schematic of da/dN-K curve and its micromechanism [1].
Key: (1) Stage A; (2) Non-continuous mechanism;
(3) Factors with large effects; (4) Microstructure;
(5) Mean stress; (6) Environment; (7) Lattice constants/
cycle; (8) Threshold value; (9) Stage B; (10) Contin-
uous mechanism; (11) Factors with small effects;
(12) Microstructure ; (13) Thickness; (14) Factors with
large effects: environment, mean stress and frequency;
(15) Final damage; (16) Stage C; (17) Static mechanism
(cleavage and intercrystalline fibers); (18) Factors
with large effects; (19) Microstructure; (20) Mean
stress; (21) Thickness; (22) Factors with small effects ;
(23) Environment; (24) Crack propagation rate when 50Hz.

In the last 20 years, a great number of studies have been
done on the second stage of the propagation behavior of fatigue
cracks and there has been deep understanding; but because of
the rapid development of the third stage of crack propagation,
the proportion occupied by the estimation of real component life
has not been large. For this reason, the crack behavior of the
first stage which has relatively large structures and environ-
mental medium sensitivity has been receiving more and more
attention. Especially following the development of fracture
mechanics and the use of new testing techniques, there have been
many scientific treatises published which have proposed many
mechanical models and micromechanisms. Yet, there are often

142

many contradictions in the data and results and even the obtaining of opposite conclusions. For this reason, it is necessary to make a brief evaluation of the studies on the micromorphology and mechanical behavior of initial period fatigue crack propagation as well as its affecting factors.

II. Microcharacteristics of Initial Period Crack Propagation.

Since the early 1960's when Forsyth [3] divided the fatigue crack propagation of aluminum alloys into the two propagation stages of I and II, there has been a great deal of investigative research done on the propagation behavior along the axial 45° crystallization mode in the first stage of the initial period of propagation and physical models were proposed. See Reference [2] for details.

As regards the micromorphology of the initial period of fatigue crack propagation, in their observations of the micro-fracture morphology of Al, Cu, Ti and Ni alloys and stainless steel, Hertzberg and Mills [4] discovered that under very low propagation rates a type of crystallographic fracture of facets or river patterns appeared. After this, Beevers [5] summarized the former works of others and listed the crystallographic orientation of the facet's produced by over ten types of alloys during the initial period of propagation. These facets were generally close to the close-packed crystalline surface of the base body such as the [111] and [001] surfaces of surface-centered cubic metals, the [110] and [001] surfaces of body-centered cubic metals and the [0001] surface of close-packed hexagonal metals. These types have facet fractures appearing under very low propagation rates and have been considered to create weakening of the combining strength of the atomic chain between the adjacent slipping surfaces because of the repeated slipping in the local area in the front end of the crack. Therefore, the local slipping surface produces cleavage fractures under low tension stress [6]. However, the

143

facet orientation of certain cubic metals which appear on
non-slipping surface [001] has still not been explained.

However, when we considered the crystalline structure,
fault energy (SFE) and slipping band types of metals and alloys,
we discovered that the orientations of these facets had certain
regularity [7]. See Table 1.

(1) 晶　格	(2) 合　金	(8) 层错能	(15) 滑移类型		(22) 个 平 面 位 向
F C C	Al 合金(3)	(9) 高	(16) 波纹		{001}
	Ni 合金(4)	(10) 低	(17) 平　面		{111}
	不锈钢(5)	(11) 低	(18) 平　面		{111}
B C C	Fe—3%Si	(12) 高	(19) 波　纹		{001}
	β 黄铜(6)	(13) 低	(20) 平　面		{011} ±10°
H C P	Ti 合金(7)	(14) 高	(21) 波　纹		{0001} ±5°

Table 1 Crystallographic orientation of facet fractures.
　　　　　Key: (1) Lattice; (2) Alloy; (3) Alloy; (4) Alloy;
　　　　　(5) Stainless steel; (6) Brass; (7) Alloy;
　　　　　(8) Fault energy; (9) High; (10) Low; (11) Low;
　　　　　(12) High; (13) Low; (14) High; (15) Slipping type;
　　　　　(16) Ripple; (17) Plane; (18) Plane; (19) Ripple;
　　　　　(20) Plane; (21) Ripple; (22) Facet orientation.

We can see from Table 1 that for cubic metals with high
fault energy and ripple slipping, alternating slipping is
easily produced which is beneficial to the appearance of
cleavage fractures along the cubic surface. For example,
certain body-centered cubic metals such as Fe-3%Si etc. can
be described by the fracture mechanism proposed by Cottrell
[8], that is

$$\frac{a}{2}\,(\,\overline{1}11\,) + \frac{a}{2}\,(\,111\,) \rightarrow a\,(\,001\,)$$

The other cubic metals (Ni base alloy, stainless steel and
β brass etc.) make the above mentioned dislocation

interaction difficult to produce because of the low fault and plane slipping. Thus, the cleavage only appears along the slipping [7]. Recently, Lynch [9], in his analysis of the mechanisms of initial period fatigue crack propagation, considered that the propagation along the [001] surface and $\langle 110 \rangle$ direction was caused by the alternate slipping on the [111] surface of crossing in the crack tip area. See Fig. 2.

(2) 滑移面1
(1) 裂纹
(3) 滑移面2
(a)

(111) 滑移面(4)
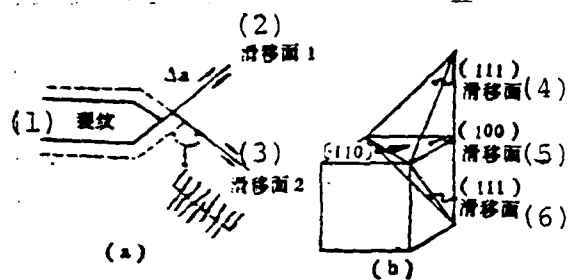(100) 滑移面(5)
(111) 滑移面(6)
(b)

Fig. 2   Schematic of propagation along the [100] surface and $\langle 110 \rangle$ direction caused by the alternate slipping of the [111] surface crossing in the crack tip area [9].

Key: (1) Crack; (2)-(6) Slipping surface.

In actual engineering materials, because of the structures (the morphology and distributions of the second phase and inclusions) and the effects of the environmental medium and stress state etc. factors, the microfracture morphology of the initial period crack propagation is often diversified. In the observations of the fracture morphology of structural steel and titanium alloys, Gerberich and Moody [10] pointed out that the initial period microfractures of these two types of materials can be divided into the two major categories of transcrystalline and along the crystal and and there are nine types of morphology: (a) oblique cleavage; (b) alternating cleavage; (c) cracking between α/β phases; (d) α phase cleavage in α/β areas; (e) branch intercrystalline cracking in hard base body; (f) branch intercrystalline cracking in soft base body; (g) plastic

intercrystalline cracks; (h) cavity sum of grain boundary
created by particles; (i) joining of intercrystalline crystal;
see Fig. 3. The first four types are transcrystalline and the
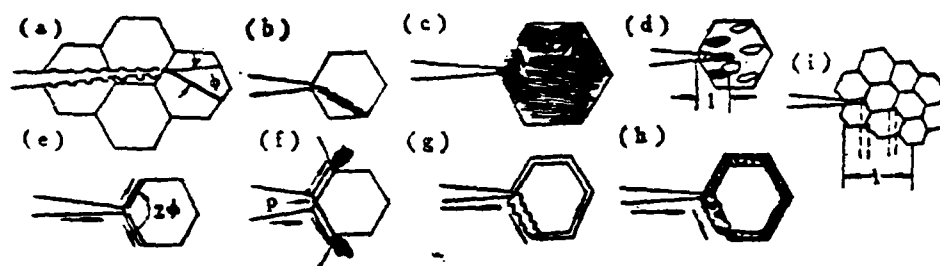latter five are along the crystal types.

Fig. 3 Microfracture morphology of initial period fatigue
        crack propagation [10].

Freudental [11] considered that because of the non-uniformity
and discontinuity of the local structures in the actual compon-
ents as well as the various distortions on the surface and inside,
the micromechanism of the fatigue crack propagation is mainly
composed of the non-slipping shear cracks in the high strength
alloys and the slipping surface cracks produced by the soft
metal repeated slipping as well as the two types of mechanisms
in medium strength alloys.

We can see that in actual engineering components and samples,
the fracture morphology is varied. However, they also have a
certain basic change law. Based on a large number of crack
orientation and fracture analyses of aluminum alloy, structural
steel and high temperature alloy samples and parts, Quyang Jie
[12] deduced eight types of fracture shapes and considered that
these fractures could be described by the "alternating shear"
mechanism and the "al.ernating tear-shear" mechanism. From an
analysis of a simple stress state, I [2] consider that the
initial period of crack propagation belongs to the bidirectional
tension of the plane stress mode. At this time, the shearing

146

stresses on the slipping surface cancel eachother and the positive stresses superimpose eachother which is beneficial to the appearance of cleavage fractures on the facets.

III. Mechanical Behavior and Threshold Values of Initial Period Crack Propagation

In recent years, in order to save on energy resources, decrease material consumption and raise product functioning, it has been difficult to avoid the existence of notches and stress concentration areas in engineering components. Especially for some components such as engine rotor parts, gears, crankshafts, pressure containers etc., they sustain small amounts of low cycle large loads (e.g. starting and stopping) and large amounts of high cycle low loads. Moreover, it is relatively difficult to examine the cycle of these parts during long operations. For this reason, these parts require the guaranteeing of safe crack propagation (or no propagation). Thus, a new important branch was developed from "destruction tolerance design" in product design which is the "safe crack design" [13]. Therefore, study of the mechanical behavior and the threshold values of the initial period fatigue crack propagation has been given further serious attention.

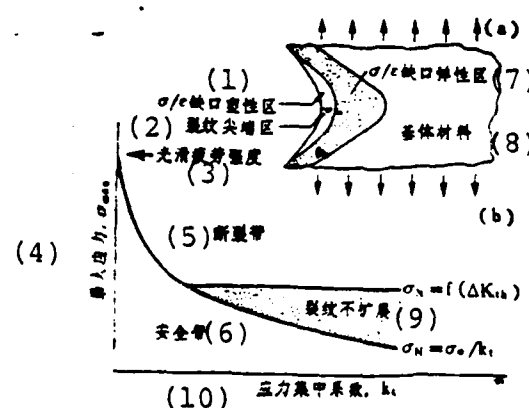### 3.1 Fatigue Limit and Crack Propagation Threshold Value

Fig. 4 (see next page).

147

Fig. 4 (continued) (a) Sketch of stress/strain field in notched
samples; (b) schematic of interrelationship of the
smooth and notched fatigue limits and the threshold
value stress [13].

Key: (1) Notch plastic area; (2) Crack tip area; (3)
Smooth fatigue strength; (4) Maximum stress; (5) Fracture
zone; (6) Safety zone; (7) Notch elastic area; (8) Base
body material; (9) Cracks with no propagation; (10)
Stress concentration coefficient.

Figure 4 (a) is a schematic of the stress-strain field and
fatigue crack growth in notched samples and the propagation area.
We can see from the figure that because there are relatively
large plastic and elastic pressure stress fields in front of the
crack tip, the crack appears halted or having a very low rate
of propagation. Figure 4 (b) is a schematic of the interrela-
tionship of the smooth and notched fatigue limits and the
fatigue threshold value stress [13].

Lukas [14] pointed out that at present there are three types
of fatigue limits: the crack propagation threshold value
(ΔK_{th}), the fatigue stress limit (σ_c) and the fatigue plastic
stress limit (ε_{apc}). The latter two types of fatigue limits
have the following relationship:

$$\sigma_c = k\varepsilon^n_{apc} \qquad (1)$$

In the formula, k and n are material constants and there is also
an interrelationship between the fatigue threshold value and
the fatigue threshold value and the fatigue stress limit.
Assuming K_{atb} is the basic threshold value, under symmetrical
stress cycles, $K_{atb} = \Delta K_{th}/2$. For a penetrating crack, we
obtain

$$K_{atb} = 1.12\sigma_c \sqrt{\pi a_c} \qquad (2)$$

In the formula, a_c is the critical crack dimension and when the
sample has notches,

$$K_{atb} = \sigma_{c_n} \sqrt{\pi a_c} \; F(a_c, k_t, \rho) \qquad (3)$$

In the formula, σ_{c_n} is the notch's fatigue limit, k_t is the notch's stress concentration coefficient and ρ is the notch's radius. The approximate relation of the above formulas can be written as

$$\sigma_{c_n} = \frac{\sigma_c}{k_t} \left[1 + \frac{1.14}{\rho} \left(\frac{k_{atb}}{\sigma_c} \right)^2 \right]^{1/2} \qquad (4)$$

Following the increase of the strenth, σ_c gradually increases, K_{atb} then decreases, the second term in the brackets also decreases and σ_{c_n} approaches the σ_c/k_t value. When ΔK_{th} is known, this simplified formula can be used in engineering.

In a recent paper comprehensively analyzing fatigue limits and threshold value, Smith [15] pointed out the interrelationship between the smooth and notched fatigue limit and the threshold value. Based on the general fracture mechanical (LEFM) formula, threshold value (ΔK_{th}) is the function relation of applied stress amplitude value ($\Delta \sigma$) and crack length (a). When the crack begins to grow,

$$\Delta K_{th} = f \Delta \sigma \sqrt{\pi a} \qquad (5)$$

In the formula, f is the correction coefficient of the geometric dimensions and when a penetrating crack grows from the surface,

$$K_1 = 1.12 \Delta \sigma \sqrt{\pi a} \qquad (6)$$

In order to cause the crack to not go as far as propagating, it is necessary that

$$\Delta K_{th} \geqslant 1.12 \Delta \sigma \sqrt{\pi a} \qquad (7)$$

We can see from the above formula that when the length of

the crack is very small it is necessary to add relatively large
stress amplitude so that the crack can grow. In Fig. 5, long
crack threshold value ΔK_{th} can be expressed by 1/2 the slope
of the straight line. That is

$$a_0 = 0.25 \left[\frac{\Delta \bar{K}_{th}}{\Delta \sigma_0} \right]^2 \qquad (8)$$

The a_0 of soft steel ($\Delta K_{th} = 9.9 MNm^{-3/2}$, $\Delta \sigma_0 = 240 MNm^{1/2}$)
is about 0.2mm and the a_0 of hardened steel ($\Delta K_{th} = 3.4 MN^{-3/2}$,
$\Delta \sigma_0 = 670 MNm^{-1/2}$) is about 0.005mm. This is why the mass
requirements for the surface of the high strength materials
are high and the surface delineating marks cause the fatigue
life to greatly decrease. This is because the existence of
the delineating marks possibly shorten and even eliminate the
sprouting of the cracks and the initial period propagation
stage.

At the same time, we can also see that when crack growth is
less than a_0, the formulas established on continuous mechanics
(LEFM) are already unsuitable for use again. At this time, the
crack propagation law is already different from those measured
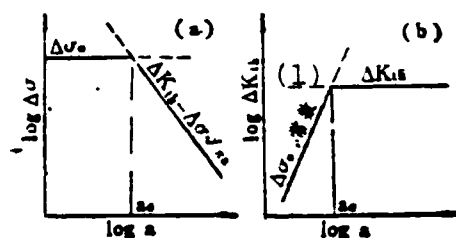under common length cracks. See Fig. 5 (b)

Fig. 5 (a) is the transformation from the smooth fatigue limit
to the long crack ΔK_{th} and its (b) influence on the
measured threshold value [5].

Key: (1) Constant.

This phenomenon was also proven by the test results published
by Romaniv et al [16] recently. When the crack growth exceeds

150

its critical value $(a^{o}s)$, ΔK_{th} is unrelated to the crack length. They also give the expression of short crack threshold value (ΔK_{th}^{sh}) and long crack threshold value (ΔK_{th}).

$$\Delta K_{th}^{sh} = \Delta K_{th} \left(\frac{a_s}{a_s^o}\right)^r \tag{9}$$

In the formula, r is the material's constant.

3.2 Propagation Behavior of Short Cracks

Kitagawa and his collaborators [17] also studied the threshold value stress of structural steel bar samples with different strength levels of surface microcracks and obtained the following relational formula:

$$\Delta\sigma_{th} = \frac{\Delta K_{th}}{f(a)\sqrt{\pi a}} \tag{10}$$

In the formula, f(a) is the function related to the crack dimensions and the sample's geometric shape.

El Haddard et al [17,18] used the side notched thin plate CSAG40-11 steel sample to further prove this phenomenon. In order to make the LEFM fracture mechanical method effective, they introduced a constant l_o for correction. That is

$$\Delta K = \Delta\sigma\sqrt{\pi(a+l_o)}\ F \tag{11}$$

In the formula, F is the constant related to the samples geometric dimensions and for small penetrating cracks, F is approximately equal to 1. When a is close to zero, $l_o \gg a$, $\Delta\sigma = \Delta\sigma_e$ and $\Delta K = \Delta K_{th}$. We obtained a relational formula similar to formula (8)

$$l_o = \frac{1}{\pi}\left(\frac{\Delta K_{th}}{\Delta\sigma_e}\right)^2 \tag{12}$$

When we consider using the 1.12 coefficient for approaching the surface crack, formulas (8) and (12) basically coincide. By substituting formula (11) into the above formula, we can obtain the general formula of threshold value stress ($\Delta\sigma_{th}$) when in any crack length,

$$\Delta\sigma_{th} = \frac{\Delta K_{th}}{\sqrt{\pi(a+l_0)}} \qquad (13)$$

Figure 6 shows the relational curve of the G40-11 steel's fatigue threshold stress and crack length [17]. We can see that when l_0=0.24mm, the estimated value agrees well with the test results. At present, the physical significance of l_0 is still unclear and this is possibly related to the stress-strain field of the crack tip.
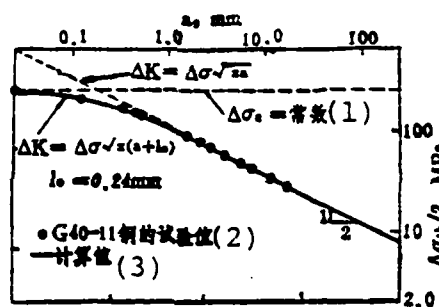

Fig. 6 Relational curve of the G40-11 steel's fatigue threshold stress and the crack length [17].

Key: (1) Constant; (2) Test value of G40-11 steel; (3) Calculated value.

Opper and El Haddad obtained a similar formula for short crack propagation after analysis of the initial period fatigue crack propagation of notched samples,

$$\Delta\sigma_{th} = \frac{\Delta K_{th}}{K'\sqrt{\pi(l+l_0)}} \qquad (14)$$

In the formula, K' is the elastic stress concentration coefficient and l is the crack length. The above formula can be

152

written as

$$\Delta \sigma_{th} = \frac{F \cdot \Delta \sigma_e}{K'} \sqrt{\frac{l_0}{l+l_0}} \qquad (15)$$

For a middle or side notch with a depth of C

$$K' = \sqrt{\frac{l+c}{l}} \qquad (16)$$

When l is close to zero, K' then approaches 1.12xK.

From formulas (15) and (16) we can obtain

$$\Delta \sigma_{th} = F \cdot \Delta \sigma_e \sqrt{\frac{l}{l+c}} \sqrt{\frac{l_0}{l+l_0}} \qquad (17)$$

If the maximum value of $\Delta \sigma_{th}$ is $\Delta \sigma p$, it will be located in $l^* = \sqrt{cl_0}$ and then formula (17) is simplified into

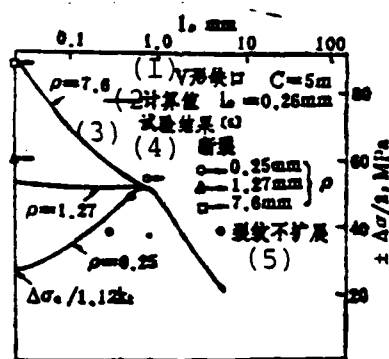$$\Delta \sigma_p = \frac{F \Delta \sigma_e}{1 + \sqrt{c/l_0}} \qquad (18)$$

Fig. 7   Comparison of curve calculated from saples with differ-
ent notch radii and the test values [19].

Key: (1) V shaped notch; (2) Calculated value; (3) Test
results; (4) Fracture; (5) Crack with propagation.

Figure 7 shows the comparison of the values of the samples with different notch radii calculated from formulas (15) and (18) and the test values (V shaped notch depth C=5mm and l_o=0.29mm).

For the "sharp notch" and the crack's initial stress, $\Delta\sigma$i'

$$\Delta\sigma_i = \Delta\sigma_e/K_t \qquad (19)$$

This stress increases with the elongation of l until it reaches its maximum value.

For the "dull notch," this stress decreases with the increase of l (or is equal to its initial stress), that is

$$K_t = l + 2\sqrt{c/\rho} \qquad (20)$$

The boundary lines of the two types of notches is $\rho c_r = 4 l_o$ and from formula (20) we can obtain

$$K_{tc_r} = l + 2\sqrt{c/\rho c_r} \qquad (21)$$

Then

$$C_{c_r} = (K_t - l)^2 l_o \qquad (22)$$

Figure 8 shows the short crack's propagation behavior beginning from notches with different geometric shapes [18].
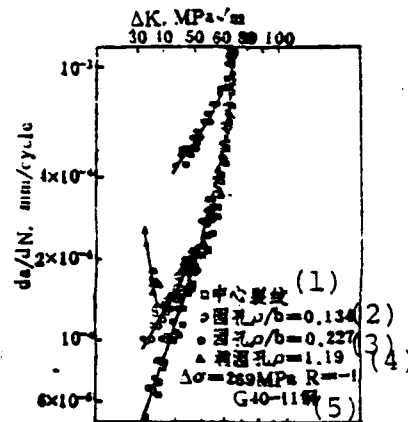
154

Fig. 8   Short crack's propagation behavior beginning in the
          notch area with different geometric shapes [18].

          Key: (1) Center crack; (2) Circular hole; (3) Circular
          hole; (4) (Illegible?) circular hole; (5) Steel.

Hudak Jr. [48] did an analysis of short crack propagation
behavior and gave the following preliminary conclusions:

(1) When the general fracture mechanics analysis method
(LEFM) is used, the crack behaviors of the short cracks and
long cracks are different. The main reason for this is that
the supposition of general continuous mechanics is not again
suitable.

(2) The short cracks can grow when the crack dimensions and
added stress level are estimated lower than the long cracks.

(3) The growth rate of the short cracks is higher than the
growth rate calculated by the long crack $da/dN-\Delta K$ data.

(4) The true propagation behavior of short cracks should
consider adding a constant length l_o on the actual crack dimen-
sions. At present, the physical significance of l_o is still
not understood yet by using it we can suitably determine the
threshold value of short cracks and its propagation behavior.

155

Miller and his collaborators [20,21] raised doubts concerning the above mentioned analysis and considered that the physical significance of the introduced constant l_o was still unclear. For example, the different propagation behaviors of some short cracks when lower than $\Delta\sigma_e$ are still unable to be measured by formula (11). Aside from this, l_o is also unable to be a constant because it is related to the exerted stress level. For this reason, they proposed a model which uses the local plastic shearing model to describe the sprouting and early period propagation of the cracks. See Fig. 9. In the figure, ΔS is the notch's plastic shearing displacement and it is the function of the stress level, period, yield strength and shape dimensions.
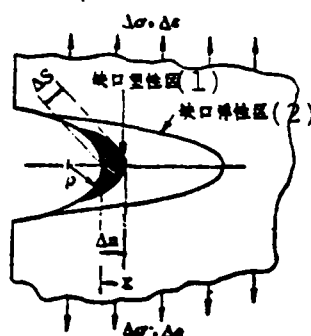

Fig. 9   Elastic and plastic stress-strain fields of notch
         root [21].
         Key: (1) Notch's plastic area; (2) Notch's elastic area.

When a crack enters the plastic area, shearing displacement $\{\phi_t\}$ of the crack tip can be considered to originate from plastic shearing displacement $\{\phi_p\}$ caused by the notch plastic area and this shearing displacement decreases with the deep plastic area of the crack; further, plastic deformation (ϕ_e) produced by the strangeness of the crack tip (which can be obtained by LEFM analysis). Therefore

$$\phi_t = \phi_p + \phi_e \qquad\qquad (23)$$

They consider that the ϕ_t critical value of crack sprouting and propagation can be

$$\phi_{tcr} = \frac{\Delta K_{th}}{\sqrt{2} \, E \, \Delta\sigma_{cy}} \qquad\qquad (24)$$

In the formula, $\Delta\sigma_{cy}$ is the cycle yield strength. When the crack grows from a notch area, the decrease rate of ϕ_p is possibly faster than ϕ_e and thus the situation of $\phi_t < \phi_{th}$ appears. See the $|\phi|_{e2}$ curve in Fig. 10. This produces non-propagating cracks.
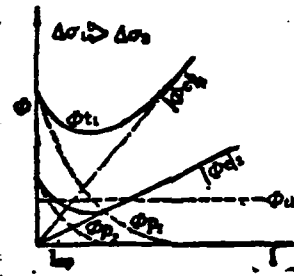

Fig. 10 Schematic of fatigue crack propagation of notch under different stress levels [21].

To sum up, at present, the propagation of short cracks during the early period of fatigue cracking and its mechanism are still in the development stage and await further test work and deep theoretical analysis.

IV. Factors Affecting Early Period Crack Propagation

4.1 The Effects of the Stress Ratio

Among the factors affecting initial period crack propagation behavior and threshold value, it is generally considered

that stress ratio R is one of the important factors [22]. The increase of R will cause the initial period propagation rate and threshold value to decrease.

The following formula is generally used to indicate the effects of the R specific value or mean stress on the ΔK_{th} value of the relatively low propagation rate range [23].

$$\Delta K_{th} = \Delta K_{tho} (1-R)^r \qquad\qquad (25)$$

In the formula, r is the material's constant; ΔK_{tho} is the threshold value when R=O which shows that the above formula is only applicable when R is a positive value. Kaisand and Mowbray [24] gave general formulas which coincide well with the test data,

$$\Delta K_{th} = \Delta K_{tho} \; f(R) \qquad\qquad (26)$$

(1)
当 R > 0 时, $f(R) = \left(\dfrac{1-R}{1+R}\right)^{1/2}$

R < 0 时, $f(R) = \left(\dfrac{1-R}{1+R/3}\right)^{1/2}$

(2)

Key: (1) When; (2) When.

That is, when R is a negative value, they suppose that during the loading period the R value only has a 1/3 compression section which has an effect on the crack propagation.

There have been different explanations of the effects of stress ratio R on the crack's initial period da/dN and the threshold value. As for Klesnil and Lukas [25] considering that the load process for structural steel is an important factor,

158

they also pointed out that the effects of R on the threshold are also due to the compression stress of the crack tip's plastic plastic area. Schmidt and Paris [26] used the crack closure effects to explain the effects of R on the threshold value.

For low stress ratio, $K_{min} \leqslant Kc_1$

$$K_{max} = Kc_1 + \Delta K_o = \text{constant} \tag{27}$$

$$\Delta K_{th} = K_{max} - K_{min} = K_{max}(1-R) \tag{28}$$

For high stress ratio, $K_{min} \geqslant Kc_1$

$$\Delta K_{th} = \Delta K_o = \text{constant}$$

$$K_{max} = \frac{\Delta K_{th}}{1-R} = \frac{\Delta K_o}{1-R} \tag{30}$$

The above relationships were proven in 2024-T3 aluminum alloy, A533 steel and T-1 titanium alloy. Test results show that loading frequency has certain effects on aluminum crack closure stress strength factors Kc_1 and ΔK_{th}. Under low stress ratio, the effects of frequency on K_{max} are not great [27].

In his study of the crack propagation process of BS-4360 low alloy steel in the near-threshold range, Radon [28] discovered that the size of the effects of R is also related to the thickness of the sample. For example, the effects of a relatively thin sample (B=12mm) are quite noticeable but in a sample with a thickness of 50mm, R does not have large effects. This phenomenon is possibly related to the stress state and closure effects of the sample.

Further, prestrain also has different effects on the thres hold value of carbon steel under different R ratios (see Fig.11).
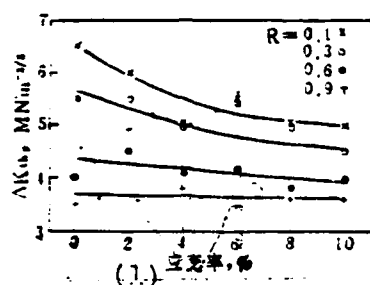
Fig. 11 Effects of ΔK_{th} value of prestrain on carbon steel (0.1C-1.5Mn) under different R ratios [29].

Key: (1) Strain rate.

Blacktop and others [29] consider that under low stress ratio the effect of the cooling process is possibly related to the plastic area dimensions of the crack tip. At the same time, they also pointed out based on the following formula [30]

$$\Delta K_{th} = E \epsilon_f \sqrt{2 \pi \rho_{min}} \qquad (31)$$

that the prestrain will cause the ϵ_f in the formula to decrease and thus cause its threshold value to decrease.

4.2 The Effects of Microstructures

To date, there have been a great amount of test data and many test formulas published concerning the effects of the crystal grain size on initial period crack propagation and the threshold value. For example, Kitagawa et al [31] discovered the following relation between ΔK_{th} and σ_j in tests on low strength alloy steel

$$\Delta K_{th} = AE - B \sigma_y \qquad (32)$$

In the formula, A and B are test constants. In his study on the effects of crystal grain dimension (d) on the threshold value of manganese steel, Beevers [5] proposed the following test formula

$$\Delta K_{th} = 3.8 + 1.4 \times 10^3 d^{1/2} \qquad (33)$$

160

and $\sigma_j = 139 + 0.347d^{-1/2}$ (33')

Taira et al [32] in their study of the effects of crystal grain size on the threshold level of low carbon steel pointed out that ΔK_{th} increases with the enlargement of crystal grain dimension ($d^{1/2}$) and gave a formula for calculating effective threshold value (K_{effth}) and crystal grain dimension $d^{1/2}$,

$$\Delta K_{effth} = 0.19 + 1.96 \times 10^{-2} \sqrt{d}$$ (34)

In the formula, $\Delta K_{effth} = K_{max} - K_{op}$. They discovered that the crack tip's slipping zone ε_s enlarges with crystal grain dimension (d), that is, $\varepsilon_s = 0.51d$. The da/dN- Δ K curve with different crystal grain dimensions is indicated by ΔK_{eff} and approaches a straight line. See Fig. 12.
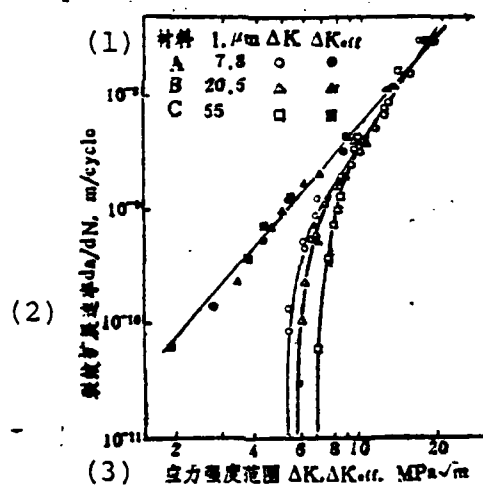

Fig. 12   da/dN- Δ K curve of low carbon steel with different crystal grain dimensions [32].

   Key: (1) Material; (2) Crack propagation rate;
   (3) Stress strength range.

After Gerberich and Moody [10] did an analysis of test data for structural steel and titanium alloys with different strength levels, they pointed out that the slope of the

$\Delta K_{th}/E-d^{1/2}$ variation curve of different materials assumed the two types of models of positive and negative numbers as shown in Fig. 13.
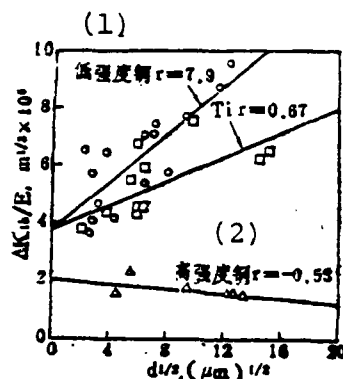

Fig. 13 $\Delta K_{th}/E-d^{1/2}$ variable curve of different materials [10].

Key: (1) Low strength steel; (2) High strength steel.

From the above results, we only consider that the crystal grain dimensions are insufficient and it is also necessary to analyze its internal microstructure and morphology.

Gu Haicheng and Knott [33] gave the following relational formula

$$\Delta K_{th} = (\pi \rho */2)^{1/2} \sigma_{u \cdot f}(R) \qquad (35)$$

They consider that the threshold value is only related to tension strength (σ_u) of the material and is also connected to its structural "distance parameter" ($\rho*$) (i.e. the Neuber material constant). The increase of the tension strength often carries a decrease of the structural distance parameter. Thus, the peak value of a ΔK_{th} can appear under different tempering temperatures for certain steels.

For multiphase alloys, Masounave et al [34] studied the fatigue crack propagation behavior of different ferrite (a) and pearlite (p) in carbon steels and pointed out the following relationship which exists between ΔK_{th} and the microstructures

162

$$\Delta K_{tho} = f_a^n \phi_a + (1 - f_a^n) \phi_p \qquad (36)$$

In the formula, f_a is the volume percentage of the ferrite; ϕ_a and ϕ_p indicate the functions of the effects of a and p on ΔK_{th}.

$$\phi_a = \Delta K_o + K_i d^{\frac{1}{2}} \qquad (37)$$
$$\phi_p = \Delta K_p = 常数 \qquad (38)$$
(1)

Key: (1) Constant

The author and others [35] discovered that the function relation between ΔK_{th} and the microstructures could be approximately expressed by the following empirical formula when determining the threshold value of high strength steel after different isothermal treatments.

$$\Delta K_{th} = 1.95 f_M + 7.53 f_B + 14.1 f_A \qquad (39)$$

In the formula, f_M, f_B and f_A are separately the volume percentages of tempered martensite, bainite and remaining austenite. We can see from the above formula that the contributions of different microstructures are different for ΔK_{th}, that is, M:B:A is approximately equal to 1:4:7. This estimation is roughly equal to the contribution of the 10% remaining austenite in 4340 steel on plastic deformation function mentioned by Schwalbe [36]. Aside from this, he also discovered when determining the lattice distortion, dislocation density, remaining stress and microhardness of cloudburst sample surface layers that the surface layer structures also markedly affect fatigue crack propagation and its threshold value [35,37].

163

In researching the effects of microstructures and crystal preferred orientation on the threshold value of Ti-6Al-4V, Brown and Smith [38] discovered that the corresponding relation of alloys with remaining β phase α isometric structures, ΔK_{th} and $\sqrt{G \cdot S}$ is not as clear as that of low strength steels. However, the T-L samples vertical to the (0001) surface and L-T samples parallel to the (0001) surface possess different initial period crack propagation behavior. When the latter was in $\Delta K \approx 3.5 \text{MNm}^{-3/2}$, they still did not discover the threshold value of the crack propagation.

We can see from the test results listed above that the effects of microstructures on the initial period crack propagation and the threshold value are complex and there have been explanations of these phenomena. It is generally considered that this is closely related to the reverse plastic area's dimensions (r_y)

$$r_y = \frac{1}{6\pi} \left(\frac{\Delta K}{\sigma_y} \right)^2 \qquad\qquad (40)$$

and that the relative dimensions of r_y and the microstructures are a major factor affecting initial period crack propagation and the threshold value.

When researching the effects of the microstructures of titanium alloy Ti-6Al-4V on fatigue crack propagation, Irving and Beevers [39] considered that when the size of the plastic area reaches the dimensions of the microstructure, the crack growth will reach from structurally insensitive to structurally sensitive. Kao and Byrne [40] also pointed out that the cementite distances in the pearlite steel is the minimum microstructure unit. They have predominant effects on the fatigue crack propagation of steel while the effects of the original austenite's crystal grain size and other grain boundaries on the crack propagation at the near-threshold range are in a

secondary position. Further, the chip distance determined the free mean distance of crack's front edge propagation displacement. The decrease of the chip distance limited the displacement of the front edge of the crack and thus delayed its propagation rate. This effect was even more noticeable in the near-threshold range.

4.3 The Effects of the Environmental Medium

Among the affecting factors, the effects of environmental mediums have been receiving much attention and it is a very complex problem. In the past, because there was a lack of test data on initial period crack propagation, later period mechanisms (e.g. the dissolving and hydrogen embrittlement etc. of metals) were often used for explanation in crack propagation. Recently, based on a large amount of test results on alloy steel and high strength steel, Ritchie [1] summarized the effects of environmental mediums on initial period crack propagation and behavior in the threshold value range into the following several points:

(1) Its effects mainly occur under low stress ratio conditions;

(2) When compared to results in laboratory air, the dry inert atmosphere caused the da/dN to accelerate and to decelerate in water;

(3) As regards high strength steel, the propagation rate in dry hydrogen gas is lower than in laboratory air.
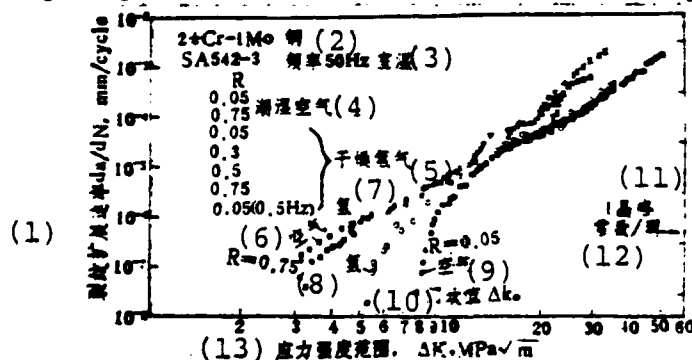

Fig. 14 (see next page)

Fig. 14 (continued) The propagation behavior of SA542-3 bain-
ite steel fatigue cracks in humid air and dry hydrogen
gas [1].

Key: (1) Crack propagation rate; (2) Steel; (3) Fre-
quency 50Hz at room temperature; (4) Humid air;
(5) Dry hydrogen air; (6) Air; (7) Hydrogen;
(8) Hydrogen; (9) Air; (10) Threshold value; (11)
Lattice; (12) Constant/cycle; (13) Stress strength
range.

Figure 14 shows the crack propagation behavior of 2 1/4
Cr-1MO bainite steel in humid air and dry hydrogen gas envir-
onments as well as under different stress ratios and frequen-
cies. We can see that the effects of hydrogen gas on crack
propagation appear in two ranges, that is, the medium rate
(da/dN-10^{-5}mm/cycle) and the near-threshold value (da/dN $<$
10^{-6}mm/cycle) [41].

There are slightly different effects of the environment on
the crack propagation of 300M high strength steel. See Fig. 15.
When the rate is higher than 10^{-6}mm/cycle, the hydrogen causes
acceleration (f=5Hz); when the rate is lower than 10^{-6}mm/
cycle, the dry hydrogen causes the initial period crack propa-
gation rate to decrease 16% [43]. This type of retardation
also appears in other high strength rotor steel [44]. We also
observed this type of retardation in salt spray tests of high
strength steel. See the schematic in Fig. 16 for the effects
of dry hydrogen gas on the crack propagation behavior of struct-
ural steel.

Fig. 15 Fatigue crack propagation behavior of 300M high
strength steel (650°C tempering) in air and dry
hydrogen gas.

Key: (1) Crack propagation rate; (2) Alloy steel;
(3) 970°C austenite melting, oil quenching and
300°C isothermal; (4) Humid air; (5) Dry hydrogen
gas; (6) Dry hydrogen gas; (7) Air; (8) Hydrogen
gas; (9) Stress strength range.

Fig. 16 Schematic of the effects of dry hydrogen gas on the
fatigue crack propagation of low strength alloy
steel [1].
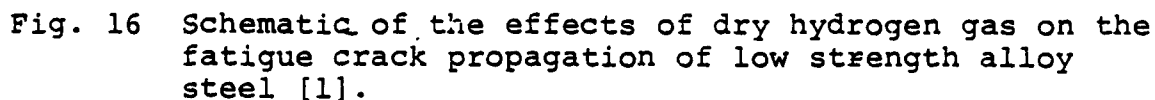
Key: (1) v decrease; (2) R increase; (3) Hydrogen gas;
(4) R increase; (5) Air (not related to R); (6) Air
(not related to v); (7) Air.

The mechanisms of the effects of environmental mediums on
initial period crack propagation can be roughly divided into
two major categories, the hydrogen embrittlement model and the
crack closure model. Although the former successfully describes

the behavior of fatigue cracks under medium or relatively high propagation rates, yet based on the above test results we can clearly see that there is another type of mechanism at work and for this reason we will focus the following discussion on the crack closure model.

During the last two years, Ritchie and his collaborators [1,45], based on test results of the effects of a large number of environmertal mediums on alloy steel and high strength steel, proposed two models for the production of crack closure effects, that is, the "oxide induced" and "roughness induced" closure models. Schematics of the two types of models are shown in Fig. 17.
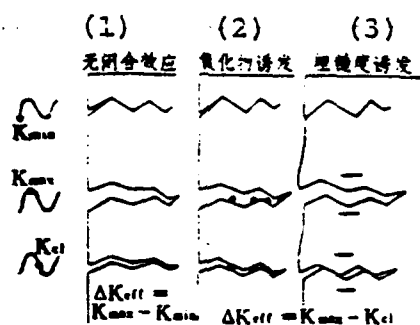

Fig. 17 Schematic of fatigue crack closure mechanisms when near the threshold value [1].

Key: (1) Non-closure effect; (2) Oxide induced; (3) Roughness induced.

The first type is-the crack advance closure caused by oxide accumulation and the second type is created by the second shearing displacement added on to the roughness of the fracture. Naturally, the closure produced by the plastic deformation will cause the oxide film to be crushed and pressed solid and produce a new surface thus causing the oxide film to become thicker. They discovered that the oxide film (Fe_2O_s) of the 4 1/4Cr-2Mo steel near the threshold value can reach $0.2 \mu m$, about 20 times that of the medium and high rate propagation areas. The thickness of the corrosion product in the dry

hydrogen is only 50-150Å. Under high stress ratio, type II displacement will cause "corrosion————oxidation" and cause the thickness of the oxide layer to greatly decrease. Figure 18 shows the variation curve of the thickness of the oxide layer of the two above mentioned types of steel measured by the Auger spectography and the crack length and da/dN.
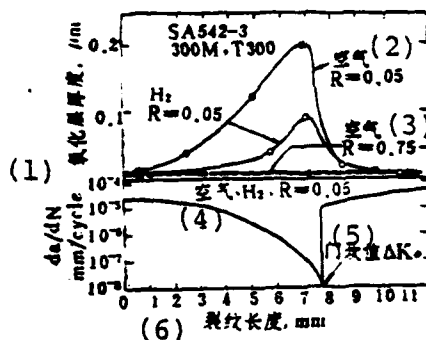

Fig. 18   Relationship of the thickness of the oxide layer in 2 1/4Cr-1M and 300M steel measured by the Auger spectograph and the crack length and da/dN [42].

Key: (1) Thickness of oxide layer; (2) Air; (3) Air; (4) Air; (5) Threshold value; (6) Crack length.

Suresh et al [45] also reduced crack closure stress strength factors and the calculated formula of Kc_1 is

$$Kc_1\bigg|_{X=0} = \frac{d \cdot E}{4\sqrt{\pi l}\,(1-v^2)} \quad (41)$$

In the formula, d is the maximum thickness of the oxide layer; 2l is the distance from the maximum thickness point to the crack tip; $E/(1-v^2)$ is the effective elastic modulus in a plane strain state. The calculated value obtained by formula (41) generally agrees with the test value.
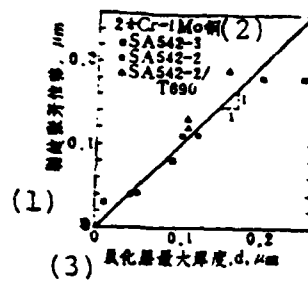
169

Fig. 19   1:1 corresponding relationship of the maximum thick-
          ness of the oxide layer of 2 1/4Cr-1Mo steel in air,
          hydrogen, helium and water and the crack opening
          displacement (CTOD) [1].

          Key: (1) Crack opening displacement; (2) Steel;
          (3) Maximum thickness of oxide layer.

Figure 19 shows the 1:1 corresponding relationship of the
maximum thickness of the oxide layer of 2 1/4Cr-1Mo steel
drawn from test data in the atmosphere, hydrogen, helium and
water and the crack opening displacement (CTOD). Therefore, the
coarse microstructures or inclusion contents will possibly pro-
duce rough or facet fracture surfaces and promote the occurance
of "roughness induced" closure. This conclusion agrees with
the observation results reported earlier by others of coarse a
titanium structure fracture surface having relatively large
"non-matching" in crack propagation near the threshold value
[46].

The above only discussed the main factors of related early
period crack propagation behavior but in reality there are
other factors such as the loading process, frequency, ampli-
tude, load type, test methods etc. as well as the comprehensive
effects of various factors which should also be conscientiously
considered. Because of the limitation of space, we cannot
enumerate in detail. The reader can refer to recently published
comprehensive evaluation references [1,2,47,48].

Concluding Remarks

This paper presented a brief review of research results during recent years on metal fatigue crack propagation behavior and the fatigue threshold value as well as the microscopic characteristics of the early period crack propagation process. We did an analysis and discussed the mechanical behavior and its major affecting factors. Because crack propagation is structurally sensitive in the near-threshold range and is noticeably affected by the environment (medium, temperature), loading conditions and test methods etc., it is necessary to conscientiously discriminate and analyze existing published test results and data. For example, the humidity in the atmosphere has strong effects on certain structural materials (such as structural steel etc.). When determining the initial period crack propagation rate and the threshold value as well as using it in engineering, it is necessary to seriously consider the important affecting factors and their overall effects. In test plan design, it is necessary to fully synthesize the working conditions of the product such as environment, temperature, stress ratio etc. and find its characteristics and laws under certain conditions. At the same time, we should also use macrocosmic and microcosmic joining, materials, techniques and structural joining and find its general laws as well as develop the use of fracture mechanics and investigate ways to raise material and component fatigue properties so as to effectively guide product design, scientific research and production practices and even better serve national economic construction.

References

[1] Ritchie, R.O., A paper presented at Intern.Symp.on Fatigue Thresholds, Stockholm(1981).

[2] Yan Minggao, "Metal Fatigue Crack Propagation Laws and Its Micromechanisms," HK 80075,CAE,(1980).

[3] Forsyth, P.J.E.,Proc.Roy.Soc.,A242, (1975), 198.

[4] Hertzberg,R.W. and Mills,W.J. ASTM STP 600. (1976), 220.

[5] Beevers,C.J., Metals Science, Aug/Sept., (1977), 362.

[6] Gell, M. and Leverant, G.R., Acta Met., 16, (1968), 553.

[7] Yan, Minggao and Wang, Zongguang, Proc.1st China-USA Bilaternal Metall. conf., Beijing, (1981), 354.

[8] Cottrell, A.H., Trans.AIME, 44, (1958), 192.

[9] Lynch, S.P., ASTM STP 675, (1979), 174.

[10] Gerberich, W.W. and Moody, N.R., ASTM STP 675, (1979), 292.

[11] Freudental, A.M., Eng.Frac.Mech., 6, (1974), 775.

[12] Ouyang Jie, Aeronautical Materials, (1978),No.4.

[13] Wanhill, R.J.H.,Proc.Intern.Symp.on Fatigue Threshold, Stockholm, (1981),Vol.1,No.3.

[14] Lukas, P., same as above, Vol.1.No.10.

[15] Smith, R.A., same as above, Vol.2,No.29.

[16] Romaniv, O.N.,et al, same as above, Vol.3,No.45.

[17] Kitagawa,H. and Takahasi, S., Proc.1CM-2,ASM,Cleveland, (1967),627.

[18] El Haddad,N.H. et al, J.Eng.Met.Tech.,ASME,101,(1979), 42; Intern.J.Frac.,16,(1980),415.

[19] Topper, T.H. and El Haddad, N.H.,Proc.Intern.Symp.on Fatigue Thresholds, Stockholm, (1981), Vol.1,No.7.

[20] Hommouda, M.M. and Miller, K.F.,ASTM STP 668, (1979),703.

[21] Hommouda, M.M. Smith, R.A. and Miller, K.J., Fat.Engng. Mater.Struct.,2, (1979),139.

References (continued)

[22] Bathies et al, same as above, 4, (1981), 1.

[23] Klesnil, M. and Lukas, P., Mater.Sci.Engng.,9. (1972),231.

[24] Kaisand, L.R. and Mowbray, D.F., J.Testing and Evaluation, 7,(1979), 270.

[25] Klesnil, M. and Lukas, P.,Eng.Frac.Mech.,4, (1972),77.

[26] Schmidt, R.A. and Paris, P.C., ASTM STP 536, (1973), 79.

[27] Nelson, D.V., Experimental Mech.17/2, (1977), 41.

[28] Radon, J.C., Proc.Intern.Symp.on Fatigue Thresholds, Stockholm, (1981), Vol.1,No.4.

[29] Blocktop, J. et al, same as above, Vol.2,No.35.

[30] Yu, Chonghua and Yan, Minggao, Fat.Engng.Mater.Struct.,3, (1980),189.

[31] Kitagawa, H., Nishitani, H. and Matsumets, J.,Proc.ICF-3, V-4(1977).

[32] Taira, S. et al, ASTM STP 675, (1979),135.

[33] Gu, Haicheng and Knott, J.F., Proc.Intern.Symp. on Fatigue Threshold, Stockholm, (1981),Vol.2, No.30.

[34] Masounave, J. and Bailon, Proc.ICM-2,Boston, (1976),513.

[35] Yan, Minggao, Gu Mingda and Liu, Caimu, Proc.Inter.Symp. on Fatigue Thresholds, Stockholm, (1981).Vol.2, No. 23.

[36] Schwalbe, K.H., Engng.Frac.Mech., 9, (1977), 795.

[37] Wang, Renzhi, Li, Xiangbin, Tan, Yonggui and Yan Minggao, Proc.1st Intern.Conf.on Shot-peening, France, (1981).

[38] Brown, C.W. and Smith, G.C. Proc.Intern.Symp.on Fatigue Thresholds, Stockholm, (1981), Vol.1,No.16.

[39] Irving, P.E. and Beevers, C.J., Mater.Sci.Engng.,14. (1974), 229.

[40] Kao, P.W. and Byrne, J.G., Proc.Intern.Symp.on Fatigue Thresholds, Stockholm, (1981), Vol.2,No.22.

[41] Suresh, S., Zamiski, G.F. and Ritchie, R.O., Met.Trans., A12, (1981).

References (continued)

[42] Toplosky, J. and Ritchie, K.O., Scripta Metellurgica, 15, (1981).

[43] Stewart, A.T., Eng.Frac.Mech., 13, (1980), 463.

[44] Liaw, P.K., Hudak, S.J. and Donald, J.K., Proc.14th Nat. Symp.Frac.Mech., U.C.L.A., ASTM, (1981).

[45] Suresh, S., Parks, D.M. and Ritchie, R.O., A Paper Presented at Intern.Symp. on Fatigue Thresholds, Stockholm, (1981).

[46] Walker, N. and Beevers, C.J., Fatigue Engng.Mater.Struct., 1,(1970),135.

[47] Blom, A.F., Aeronautical Materials (Special Edition), 2 (1982).No.1,65.

[48] Hudak Jr., S.J., Trans.ASME. J.Eng.Met.Tech., 103, (1981), 27.

END

(FILMED)

5-84